

(2)

REPORT DOCUMENTATION PAGE

Form Approved
OMB No. 0704-0188

AD-A231 924

Time to average 1 hour per response, including the time for reviewing instructions, searching existing data sources, gathering and maintaining the data needed, and completing and reviewing the collection of information. Send comments regarding this burden estimate or any other aspect of the burden to Washington Headquarters Service, Directorate for Information Operations and Assessments, 1215 Jefferson Davis Highway, Suite 1204, Arlington, VA 22202-4162, Washington, DC 20332.

| | | | |
|--|---|--|---|
| 1. REPORT USE ONLY (Leave blank) | 2. REPORT DATE 4 Dec 1990 | 3. REPORT TYPE AND DATES COVERED Final Report/30 Sep 85-29 Sep 90 | |
| 4. TITLE AND SUBTITLE Millimeter Wave Generation by Relativistic Electron Beams and Microwave-Plasma Interaction | | 5. FUNDING NUMBERS 61102F/2301/A8 | |
| 6. AUTHOR(S) Spencer Kuo | | | |
| 7. PERFORMING ORGANIZATION NAME(S) AND ADDRESS(ES) Polytechnic Institute of Technology Weber Research Institute/Route 110 Farmingdale, NY 11735 | | 8. PERFORMING ORGANIZATION REPORT NUMBER S 1 0037 | |
| 9. SPONSORING/MONITORING AGENCY NAME(S) AND ADDRESS(ES) AFOSR/NP Bolling AFB DC 20332-6448 | | 10. SPONSORING/MONITORING AGENCY REPORT NUMBER AFOSR-85-0316 | |
| 11. SUPPLEMENTARY NOTES | | | |
| 12a. DISTRIBUTION/AVAILABILITY STATEMENT Approved for public release; distribution is unlimited. | | 12b. DISTRIBUTION CODE | |
| 13. ABSTRACT (Maximum 200 words) The design and operation of a compact, high power, millimeter wave source (cusptron) has been completed and proven successful. Extensive theoretical analysis of cusptron beam and rf dynamics has been carried out and published. Theory agrees beautifully with experiment. Microwave Bragg scattering due to been achieved by using expanding plasmas to upshift rf signal frequencies. | | | |
|  DTIC ELECTE FEB 19 1991 91 2 12 042 | | | |
| 14. SUBJECT TERMS | | 15. NUMBER OF PAGES 54 | |
| | | 16. PRICE CODE | |
| 17. SECURITY CLASSIFICATION UNCLASSIFIED | 18. SECURITY CLASSIFICATION OF THIS PAGE UNCLASSIFIED | 19. SECURITY CLASSIFICATION OF ABSTRACT UNCLASSIFIED | 20. LIMITATION OF ABSTRACT UL SAR |

POLY-WRI-1582-90, November 1990 ✓

SCIENTIFIC FINAL REPORT FOR
AIR FORCE OFFICE OF SCIENTIFIC RESEARCH
GRANT AFOSR-85-0316
on
"MILLIMETER WAVE GENERATION BY
RELATIVISTIC ELECTRON BEAMS
AND MICROWAVE-PLASMA INTERACTION"

S. P. Kuo
Principal Investigator

Y. S. Zhang
K. K. Tiong
A. Y. Ho
J. Kim
A. Q. Ren

Approved for public release
Distribution unlimited

AIR FORCE OF SCIENTIFIC RESEARCH (AFSC)
DATE OF TRANSMITTAL TO DTIC
Technical report has been reviewed and is
Approved for public release IAW AFM 1.2.2
Distribution is unlimited.

Science and Technology Directorate

Prepared for

Air Force Office of Scientific Research
Grant No. AFOSR-85-0316
(Sept. 30, 1985-Sept. 29, 1990)

I. Introduction

This report only discusses work that has been carried out during the funding period from September 30, 1989 to September 29, 1990 supported under Grant No. AFOSR-85-0316. This grant has been awarded to the Polytechnic University since September 30, 1985. The work accomplished during the early funding period has already been reported in the previous four years' progress reports.

The investigation covered by this grant deals mainly with the generation of millimeter waves by means of a relativistic electron beam and with the interaction between electromagnetic waves and the plasma. However, an extension of the research effort to study the mechanism for high gradient electron beam acceleration and the arc discharge in high current carrying plasma has also been made. During the funding period a new experimental program on the study of microwave absorption, scattering and reflection by a filamentary plasma produced by hollow cathode discharge and frequency shift of microwave pulse by self-generated plasma in a plexiglass chamber also have been initiated. Many good results have been obtained and will be presented in the next section.

During the past funding year, several findings of our work have already been published or are in press. Basically, the topics of investigation are divided into four general categories: (a) optimization of the design of a compact, high power mm wave source (cusptron device) and its operation, (b) generation and application of artificial atmospheric plasma including propagation of high power microwave pulse in the air breakdown environment and Bragg scattering study, (c) wave-plasma interaction, study of the absorption, scattering and reflection of microwaves by hollow cathode discharge plasma and (d) frequency up-conversion of microwave inside a suddenly generated plasma.

For the first topic, particle simulations are employed in the analysis. The study focused on the design optimization for the cusptron device. The results are then used for the experimental setup and development of a cusptron (high harmonic) microwave tube. This tube is already radiating with reasonable output power and with expected output frequency. The second topic is devoted to the experimental study of Bragg scattering of EM waves by microwave produced plasma layers and the propagation of high power microwave pulses in the air breakdown

environment. The purpose of these experiments is to simulate the situation of producing plasma layers in the upper atmosphere for over-the-horizon (OTH) radars application. The third topic includes the setup of a hollow cathode discharge plasma and the interaction between microwave and such a plasma. The last one deals with an initial value problem. We have demonstrated that the wave frequency can be changed in a time varying medium. The focus of study is on the scattering property of filamentary plasma.

Through the support of this grant, two graduate students have completed their Ph.D. degrees. Dr. K. K. Tiong completed the requirements of the degree in August 1989. His Ph.D. dissertation was included in the last year's progress report. Dr. Y. S. Zhang completed the requirements in August 1990. His Ph.D. dissertation is included in the present report.

II. Publications

1. K. K. Tiong, S. P. Kuo and P. E. Miller, "Operational characteristics of a cusptron microwave oscillator", Int'l J. Electronics, 68(1), 127-136, 1980.
2. K. K. Tiong and S. P. Kuo, "Operation of a high harmonic cusptron oscillator", Int'l J. Electronics, accepted for publication, 68(5), 1990.
3. K. K. Tiong, "Theory and experiment of a cusptron microwave oscillator", Ph.D. Thesis, Polytechnic University, 1989.
4. S. P. Kuo and M. C. Lee, "Filamentation instability of magnetosonic waves in the solar wind environment", J. Geophys. Res., 94(A10), 13387-13395, 1989.
5. S. P. Kuo and Y. S. Zhang, "Bragg scattering of em waves by microwave produced plasma layers", Physics of Fluids B, 2(3), 667-673, 1990.
6. S. P. Kuo, Y. S. Zhang and Paul Kossey, "Propagation of high power microwave pulses in air breakdown environment", J. Applied Physics, 67(6), 2762-2766, 1990.
7. S. P. Kuo, "Frequency up-conversion of microwave pulses in rapidly growing plasma", Phys. Rev. Lett., 65(8), 1000-1003, 1990.
8. S. P. Kuo, Y. S. Zhang, and A. Q. Ren, "Observation of frequency up-conversion in the propagation of a high power microwave pulse in a self-generated plasma", Phys. Lett. A, 150(2), 92-96, 1990.
9. Y. S. Zhang, "Bragg scattering of electromagnetic wave by microwave produced plasma layers", Ph.D. Thesis, Polytechnic University, 1990.



or

a

v

Availability Codes

Avail and/or
Special

D1

A-1

10. S. P. Kuo, Y. S. Zhang, Paul Kossey and R. J. Barker, "On the feasibility of microwave produced Bragg reflector:Examined by the chamber experiment", NATO AGARD Conf. Proc., to be published.
11. K. K. Tiong and S. P. Kuo, "A TE₈₁-mode cusptron oscillator", Bull. Amer. Phys. Soc., 34(9), 2004, 1989.
12. S. P. Kuo and A. Y. Ho, "Wave scattering off a filamentary plasma produced by hollow cathode discharge", ibid, 2141, 1989.
13. Y. S. Zhang, S. P. Kuo and P. Kossey, "Lifetime of plasma generated by microwave pulse", ibid., 2141-2142, 1989.
14. Y. S. Zhang and S. P. Kuo, "Excitation of ionization instability in microwave discharge plasma", IEEE Int'l Conf. Plasma Science, 90CH2857-1, p. 83, 1990.
15. S. P. Kuo and Y. S. Zhang, "On the feasibility of microwave produced Bragg reflector for the OTH radar application", ibid., p. 152, 1990.
16. S. P. Kuo, Y. S. Zhang and A. Q. Ren, "Frequency up-conversion of microwave pulse in a rapidly growing plasma", ibid., p. 171, 1990.
17. S. P. Kuo and A. Y. Ho, "Broadband attenuation of microwave by hollow cathode discharge plasma", ibid., pp 171-172, 1990.
18. Y. S. Zhang and S. P. Kuo, "Simulation of intense microwave pulse propagation in air breakdown environment", ibid., p. 172, 1990.
19. A. Y. Ho and S. P. Kuo, "Interaction dynamics of hollow cathode discharge plasma", ibid., p. 183, 1990.

III. Appendix

Reprints and preprints attached to this report include:

1. "Operational characteristics of a cusptron microwave oscillator."
2. "Operation of a high harmonic cusptron oscillator."
3. "Filamentation instability of magnetosonic waves in the solar wind environment."
4. "Bragg scattering of em waves by microwave produced plasma layers."
5. "Propagation of high power microwave pulses in air breakdown environment."
6. "Frequency up-conversion of microwave pulses in rapidly growing plasma."
7. "Observation of frequency up-conversion in the propagation of a high power microwave pulse in a self-generated plasma."
8. "Scattering and Broadband Absorption of Microwaves by an Arc Plasma Column."

Operational characteristics of a cusptron microwave oscillator

K. K. TIONG,[†] S. P. KUO[†] and P. E. MILLER[†]

The operational characteristics of a cusptron oscillator for three different harmonic interactions (8, 10 and 12) are studied via numerical particle simulation. The results lead to the determination of the optimum design parameter of the waveguide structure for both TR_{N_01} and TE_{02} modes. For the TE_{N_01} modes, it is found that the π mode is roughly twice as efficient as the 2π mode counterparts. The efficiency study of the tube operating at the TE_{02} mode (where only the 2π mode exists) leads to a single optimum waveguide parameter, $b/a = 1.3$ (b and a are the outer and inner radii of the waveguide) for all three harmonics.

1. Introduction

Recently, there has been considerable effort in generating powerful microwave radiations by relativistic electron beams. Various devices including gyrotrons (Kuo *et al.* 1986, Granatstein *et al.* 1975), relativistic magnetrons (Palevsky and Bekefi 1979), and free-electron lasers (McMullin and Bekefi 1981) have been studied experimentally and theoretically. In general, these devices are not aimed to be physically compact for the purposes and requirements of their operation. In contrast, cusp-trons (Namkung 1984, Kuo *et al.* 1988, Tiong *et al.* 1987, Lawson and Striffler 1986, Chu and Dialetis 1984) are being developed with the aim of keeping the physical size of the devices compact.

The cusptron tube is a promising device for efficient operation at higher cyclotron harmonic modes (Namkung 1984, Tiong *et al.* 1987, Lawson and Striffler 1986). A cusp magnetic field is employed to produce an axis-encircling electron beam (E-layer) as the radiation source. Such a beam configuration features the strongest finite Larmour radius effect (Chu and Dialetis 1984) for the harmonic interactions. This device also uses a slotted cylindrical waveguide, similar to the anode blocks of a magnetron, to determine the field pattern of the resonant mode. The harmonic resonance interaction is further improved by the periodic structure of the waveguide wall which introduces periodic fringe fields in the field pattern of the mode, and enriches the resonant harmonic contents of the mode fields as experienced by the electrons (Lau and Barnett 1982). Moreover, such a waveguide structure can allow efficient operation even at low beam energy and minimize the competition between the modes.

Similarly to the magnetron device, the cusptron can also have π mode and 2π mode operations. In the 2π mode operation, the phase shift from one slot to the next is 360° , and thus, the number of slots on the waveguide wall suggests the optimum cyclotron harmonic number for the resonant interaction. In comparison, the phase shift between two adjacent slots is 180° in the π mode. Hence, π mode operation needs twice the number of slots for the same cyclotron harmonic interaction. Consequently, the field pattern of the resonant mode in each operation is expected to be different from one another. This, in turn, will give rise to a difference

Received 27 September 1988; accepted by P. A. Lindsay, 28 November 1988.
Polytechnic University, Long Island Center, Farmingdale, NY 11735, U.S.A.

in the output efficiency. In order to reach a conclusive decision on the mode of operation, a comparative study of the performance of the cusptron tube operating in the π mode and 2π mode is needed.

In the present work, the non-linear evolution of the radiation fields of the cusptron tube is studied by using a particle simulation (Kuo *et al.* 1988). The functional dependence of the efficiency on the beam energy γ , and on the ratio b/a of the outer radius b to the inner radius a of an N -slotted waveguide will be determined. We will consider the cases of $N = 8, 10$ and 12 for 2π mode operation, and $N = 16, 20$ and 24 for π mode operation. The purpose of this study is to identify the optimum design parameters and the mode of operation for the device.

2. Characteristic equations

The resonant interaction between an axis-encircling electron beam and the modes of a slotted cylindrical waveguide is studied. The cross-sectional view of the waveguide is shown in Fig. 1. The structure of the waveguide is characterized by the slot number N , the half-angle of the slot θ_0 , and the radii a and b . Using only the fundamental mode fields for the slot regions, the boundary conditions of the TE mode fields at $\rho = a$ lead to the equation

$$\frac{1}{2} \sum_{n=-\infty}^{+\infty} \left[\frac{\sin \Gamma \theta_0}{\Gamma \theta_0} \right]^2 \frac{J_\Gamma(ka)}{J'_\Gamma(ka)} = F(ka) \quad (1)$$

for the determination of the transverse wavenumber k of the mode fields, where the cut-off condition $k_z = 0$ is assumed; $\Gamma = m + nN$, where m is the mode index, which determines the phase difference between slots; $m = 0$ for the 2π mode and $m = N/2$ for the π mode;

$$F(k\rho) = \frac{[J_0(k\rho)Y'_0(kb) - J'_0(kb)Y_0(k\rho)]}{[J'_0(ka)Y'_0(kb) - J'_0(kb)Y'_0(ka)]}$$

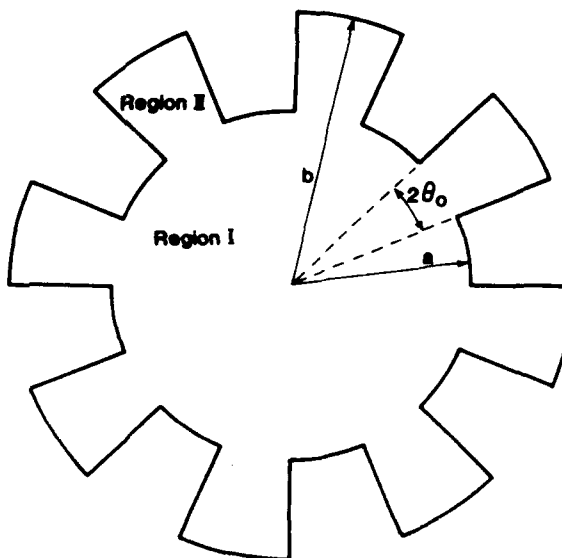


Figure 1. Cross-sectional view of the eight-vane cylindrical waveguide.

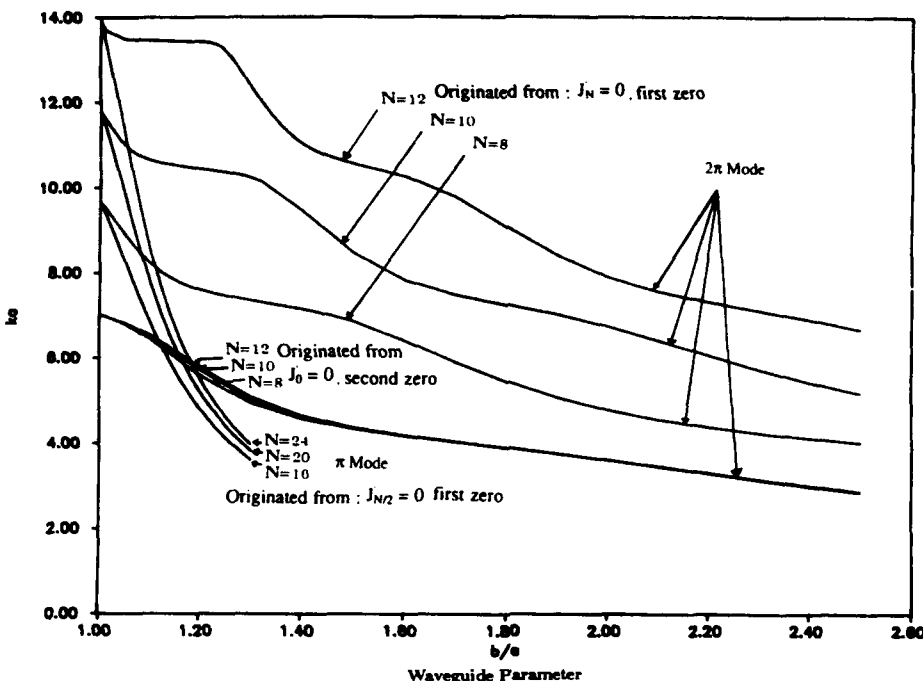


Figure 2. Relationship of the normalized transverse wavenumber (ka) with the waveguide parameter (b/a).

J_ℓ and Y_ℓ are the Bessel and Neumann functions, respectively; a 50% slot opening is considered so that $\theta_0 = \pi/2N$.

In general, (1) has multiple roots k_j , $j = 1, 2, 3, \dots$, for a given waveguide structure. Each root is a function of the ratio b/a , and defines a frequency range of operation. In the following analysis we consider for each N_0 th ($N_0 = N$ for the 2π mode and $N_0 = N/2$ for the π mode) harmonic interaction, three branches of roots starting from $b/a = 1$, namely the TE_{N_01} (both π and 2π modes) and TE_{02} (2π mode only) modes respectively. These branches of roots are presented in Fig. 2.

To achieve the resonant interaction, we have to adjust the background magnetic field to the strength such that $\Omega \approx \omega_0/N_0$ for the N_0 th harmonic cyclotron resonance, where $\Omega = \Omega_0/\gamma$ is the relativistic electron cyclotron frequency, $\Omega_0 = eB_0/mc$, and ω_0 is the eigenfrequency of the empty waveguide mode. The motion of electrons in the wavefields and a uniform axial magnetic field B_0 is governed by a set of coupled non-linear equations

$$\frac{d}{dt} \mathbf{R} = \mathbf{P}/\gamma m \quad (2)$$

$$\frac{d}{dt} \mathbf{P} = e \left[\mathbf{E} + \frac{1}{c} \mathbf{v} \times (\mathbf{B} + 2\mathbf{B}_0) \right] \quad (3)$$

where $\gamma = (1 + P^2/m^2c^2)^{1/2}$, $\mathbf{P} = \gamma m \mathbf{v}$, and \mathbf{E} and \mathbf{B} are the waveguide TE mode fields.

This set of equations can be simplified only if the resonant component of the total force is included on the right-hand side of (3). This approximation is justifiable since the perturbations on the electron orbits are mainly introduced by the resonant

components of the total force which have the slowest time variation. Consequently, only the resonant trajectory (R, ϕ) will be of interest. This trajectory can be expressed to be

$$R = R_L(t) = P(t)/m\Omega_0$$

$$\phi = \phi_0 + \psi(t) + \int_0^t \Omega(t') dt'$$

where $R_L(t)$ and $\psi(t)$, to be determined self-consistently, are the time-dependent Larmour radius and the slowly varying phase of the electrons: this results from the resonant interaction between the electrons and wave fields. From (2) and (3), the set of self-consistent characteristic equations (Chu and Dialetis 1984, McMullin and Bekefi 1981) for the resonant trajectory of the electrons is derived to be

$$\frac{d}{dt} \alpha = AE_0 J'_{N_0}(\alpha) \cos \phi \quad (4)$$

$$\frac{d}{dt} \phi = -\Delta\omega + AE_0 \left\{ \frac{\Delta\omega}{\omega} J_{N_0}(\alpha) = \frac{1}{\alpha} \frac{d}{d\alpha} [\alpha J'_{N_0}(\alpha)] \right\} \sin \phi \quad (5)$$

where $\alpha = kR_L(t)$ and

$$\phi = N_0(\psi + \phi_0) - \int_0^t \Delta\omega(t') dt'$$

E_0 is the amplitude of the wavefield;

$$\Delta\omega = \omega - N_0\Omega = \Delta\omega_0 + \omega_0(\gamma - \gamma_0/\gamma)$$

$\Delta\omega_0 = \omega - \omega_0$, and

$$\omega_0 = N_0\Omega_0/\gamma_0; \quad A = a_{N_0}\omega/B_0, \quad a_{N_0} = 1/N_0 J'_{N_0}(ka)$$

and γ and α are related through the relation

$$\gamma^2 = 1 + (\Omega_0 \alpha/\omega)^2$$

The z component of (3) reduces to $(d/dt)V_z = 0$ for $k_z = 0$ and is not coupled to the rest of the components. A similar result is also obtained under the grazing condition that $v_z = k_z c^2/\omega = v_g$. The effect of finite k_z and v_{z0} on optimum interaction is found to be small as long as $k_z c \ll \omega$.

Since the field amplitude E_0 varies during the interaction with electrons, it has to be determined self-consistently. This consideration can be included by coupling (4) and (5) to the energy conservation equation, which is given by

$$\frac{\epsilon}{8\pi a^2 N_0} \frac{d}{dt} E_0^2 = n_0 mc^2 \frac{d}{dt} \langle \gamma \rangle \quad (6)$$

where $\langle \rangle$ represents an average over the initial random phase distribution of electrons; n_0 is the electron beam density averaged over the inner cross-section of the waveguide structure and defines an averaged plasma frequency

$$\omega_p = (4\pi n_0 e^2/m)^{1/2}$$

ϵ is the effective dielectric constant of the waveguide structure for the TE mode and is given by

$$\epsilon = \sum_{n=-\infty}^{+\infty} \left[\frac{\sin \Gamma \theta_0}{\Gamma} \right]^2 \left[1 + \frac{1}{ka} \frac{J_r(ka)}{J'_r(ka)} + \left(1 - \frac{\Gamma^2}{k^2 a^2} \right) \frac{J_r^2(ka)}{J'^2_r(ka)} \right] + \frac{\pi^2}{2N^2} \left[\frac{b^2}{a^2} G^2(kb) - G^2(ka) - (1 - \delta_{ab}) \frac{1 + G(ka)}{ka} \right] \quad (7)$$

with

$$G(k\rho) = F''(k\rho) = \frac{J'_1(k\rho)Y_1(kb) - J_1(kb)Y'_1(k\rho)}{J'_1(ka)Y_1(kb) - J_1(kb)Y_1(ka)}, \quad \delta_{ab} = \begin{cases} 1 & a = b \\ 0 & a \neq b \end{cases}$$

Equations (4) and (5) describe the motion of a single electron in the wave fields, and (6) describes the evolution of the self-consistent field driven by the collective response of the electrons. In order to couple them together, a phase average over the single electron motion is necessary. This will be done numerically, in the following section, by solving the trajectories of a large number of electrons with random initial phase distribution.

3. Numerical simulation

Initially, the particles are set to be positioned symmetrically about the axis of the waveguide structure, and the energy of each particle is given by a predetermined value resulting from the cathode voltage. This distribution represents an unperturbed sample of the actual randomly distributed electrons in the ideal E -layer which have an initial density per unit length of $N_L = 1.6 \times 10^{10} \text{ cm}^{-1}$.

With each increment of simulation time during program execution, the perturbation in each particle's position is computed by integrating the coupled equations (4) and (5); from this calculation, the particle energy can also be determined. By comparing the resulting average particle energy with the initial average particle energy, the energy transferred to the wavefield can be determined through (6). The next time increment repeats the calculations using the perturbed position and energy values for the particles, along with the resulting wavefield magnitude.

In this simulation, it was found that 128 particles were sufficient to obtain accurate data; greater numbers of particles only resulted in longer execution time. The program was run on a CRAY X-MP/48 operating at the Pittsburgh Supercomputer Center. The coupled equations (4) and (5) were solved using the ODEPACK LSODE Fortran subroutine available on the CRAY.

4. Numerical results

In this section, we study the operational characteristics of cusptron devices by using a computer particle simulation approach described in the previous section. In all the calculations, we are using an ideal E -layer having a constant line density of the typical value $N_L = \pi a^2 n_0 = 1.6 \times 10^{10} \text{ cm}^{-1}$ as the radiation source. However, the initial beam energy (γ_0) will be considered as a variable. In addition, the ratio of the outer to inner radius of the waveguide, b/a , is also varied in the numerical analyses for three harmonic cases ($N_0 = 8, 10$ and 12). As shown in Fig. 2, the mode frequency $\omega_0 \approx kc$ varies with b/a , so does the cyclotron frequency $\Omega_0 \approx$

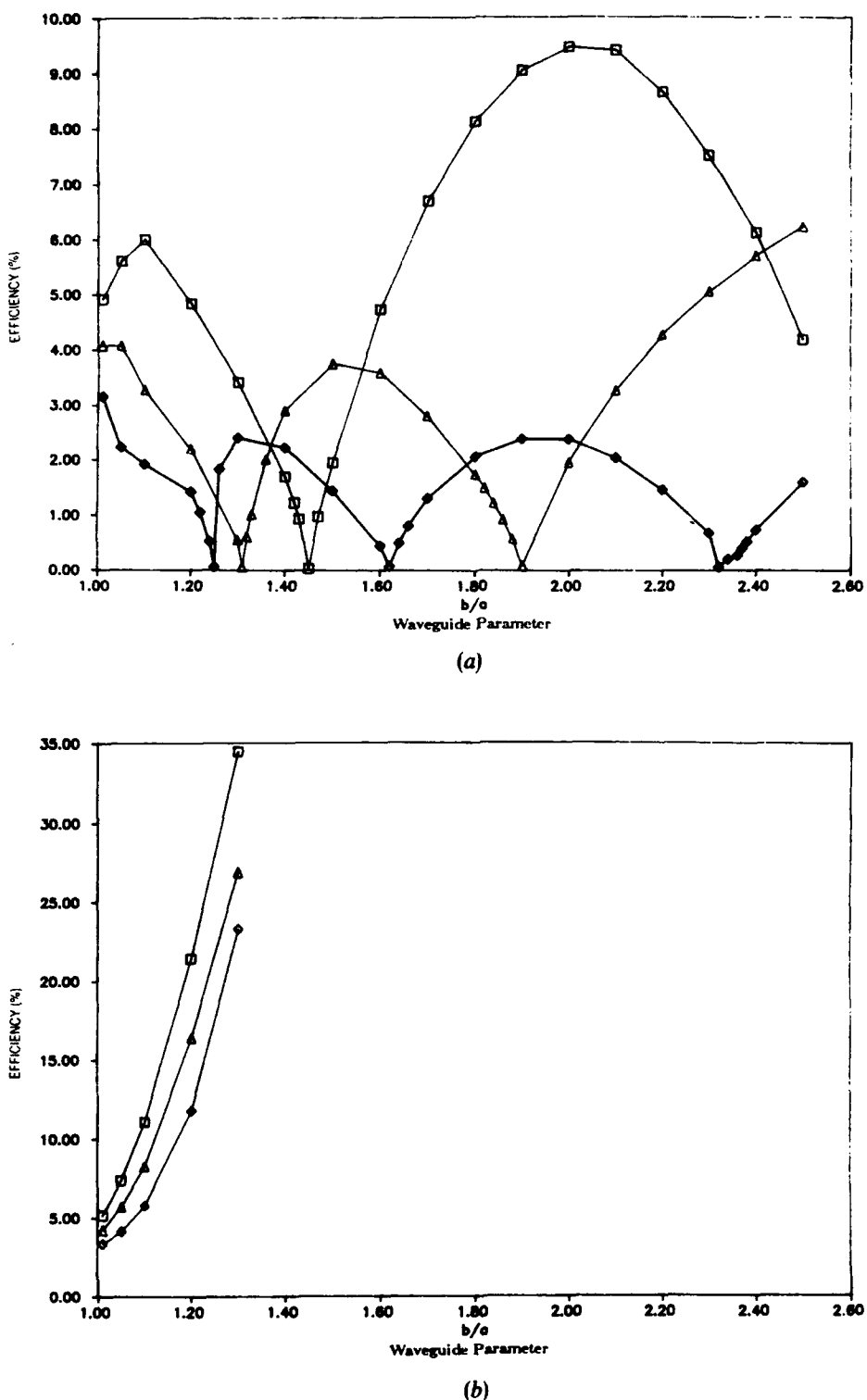


Figure 3. (a) Efficiency versus b/a for the 2π mode ($N_0 = 8$ (\diamond)) operating at the $TE_{N_0,1}$ mode with normalized Larmour radius $R_L/a = 0.7$, originated from $J'_N = 0$, first zero. (b). Efficiency versus b/a for the π mode ($N_0 = 8, 10$ and 12 ; $N = 16$ (\square)), 20 (\triangle) and 24 (\diamond)) operating at the $TE_{N_0,1}$ mode with normalized Larmour radius $R_L/a = 0.7$, originated from $J'_{N/2} = 0$, first zero.

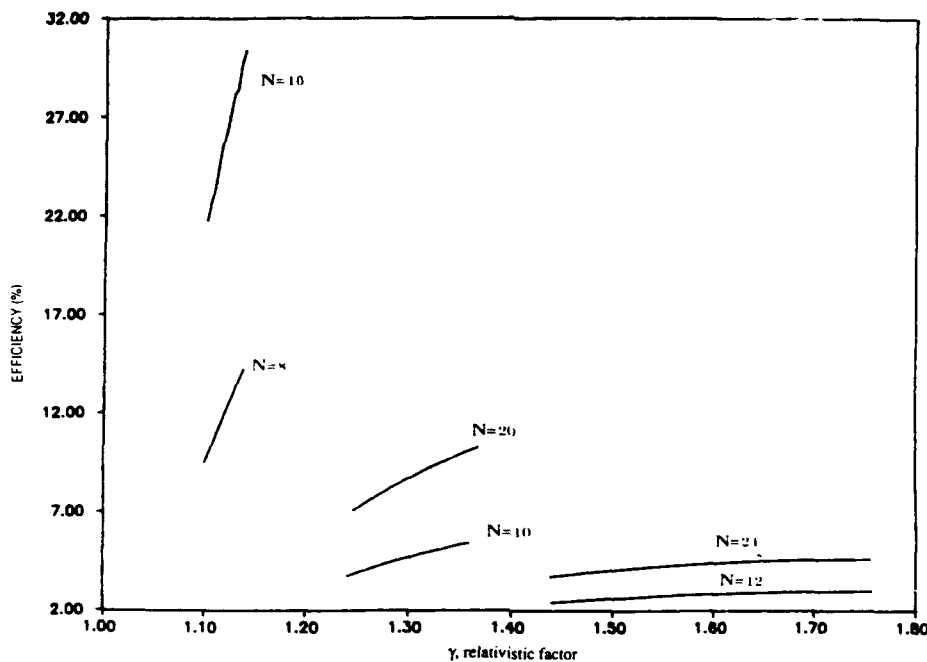


Figure 4. Efficiency versus relativistic factor (γ) for both 2π and π modes operating at TE_{N_01} mode, $0.7 \leq R_L/a \leq 0.8$.

$\gamma_0 \omega_0 / N_0 \simeq \gamma_0 k c / N_0$. In the experimental arrangement, the radius of the E -layer produced by the cusp magnetic field is, in general, fixed by the radius of the ring cathode of a Pierce gun. Therefore, the beam energy (γ_0) has to vary with b/a in order to match the electron Larmour radius R_L to the radius R of the cathode, otherwise, the produced axis-encircling beam may either become non-concentric with large spatial spread (for γ_0 to be too low) or have large v_{z0} (for γ_0 to be too large). In either case, the performance of the tube will be degraded. In order to optimize the interaction, one would like to set the radius R of the cathode as close as possible to the value a of the inner radius of the waveguide. This is because the high-harmonic mode fields are more concentrated in the region near the inner wall of the waveguide. However, for practical application, one would have to keep a gap to allow for the possible spread of the E -layer. The typical value of R_L/a is chosen to be between 0.7 and 0.8. For this reason, the beam energy used in the calculation will be varied with b/a to ensure that $0.7 \leq R_L/a \leq 0.8$.

Presented in Figs 3(a) and (b) are the functional dependences of the saturation efficiency η on the ratio b/a for the π th mode and 2π mode, respectively. In each mode of operation, three harmonic cases ($N_0 = 8, 10$ and 12) are considered, where the beam radius is fixed to be $0.7a$ and k is chosen from the upper branches of the dispersion curves of Fig. 2, whose k values at $b/a = 1$ correspond to those of TE_{N_01} modes. The results in Fig. 3(a) can be used to determine the most favourable b/a value(s) for each N_0 from which the optimum output efficiency can be achieved for 2π mode operation. Those values of b/a are identified to be $b/a = 2.0$ for the $N_0 = 8$ case, $b/a = 1.5$ for $N_0 = 10$, and $b/a = 1.3$ and 1.9 for $N_0 = 12$.

Using these b/a values for the 2π mode tubes, their operating frequencies are defined. In order to make a meaningful comparison between the performance of the π mode and 2π mode, their operating frequencies should be set to be the same for each harmonic case. The inner radius a of the waveguides and, hence, the beam

energy are also kept the same for both modes of operation. Thus, the corresponding b/a values for π mode operation can be determined from the dispersion curves of the π mode with the k_s of the 2π mode. Figure 4 displays the functional dependence of the saturation efficiencies η on the beam energy γ_0 for the specified b/a values, where γ_0 only varies in the range for which $0.7 \leq R_L/a \leq 0.8$. It shows that the π mode always has a better output efficiency than that of the 2π mode.

The frequencies defined by the lower branches of the curves of Fig. 2 correspond to the modes branching out of the TE_{02} mode due to the presence of slots on the wall. Thus, tubes operate only at 2π mode for these dispersion branches. Again, we first determine the dependence of η on b/a for each N_0 case. The results are presented in Fig. 5 for $R_L/a = 0.7$. The most favourable b/a values for the design of tubes can then be obtained from the locations of the peaks of those curves. These values are found to be quite insensitive to N_0 and are all about equal to 1.3. This is shown by the fact that all the dispersion curves are very close to each other. Thus, the harmonic content introduced by the slots depends mainly on b/a , but not the number of the slots. Using this common value for all three N_0 cases, the dependence of the optimum efficiency on γ_0 , which is restricted to vary in the range for which $0.7 \leq R_L/a \leq 0.8$, is determined for each N_0 . The results are presented in Fig. 6.

5. Summary

We have used a numerical particle simulation to study the non-linear evolution of the radiation fields excited through the negative mass instability of an ideal E -layer, which is rotating inside a slotted waveguide. The dependences of the saturation efficiency of the cusptron device on the structure of the waveguide (i.e. b/a and N_0), the mode of operation (π mode or 2π mode), and the electron beam energy (γ_0)

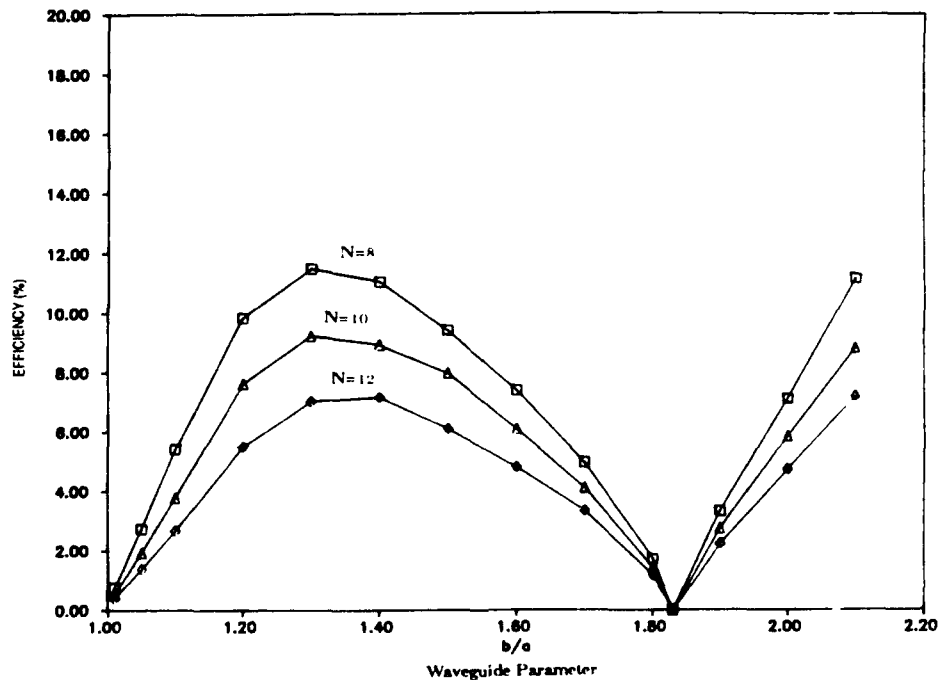


Figure 5. Efficiency versus b/a for the 2π mode ($N_0 = 8, 10$ and 12) operating at the TE_{02} mode with normalized Larmour radius $R_L/a = 0.7$. Originated from $J'_0 = 0$, second zero.

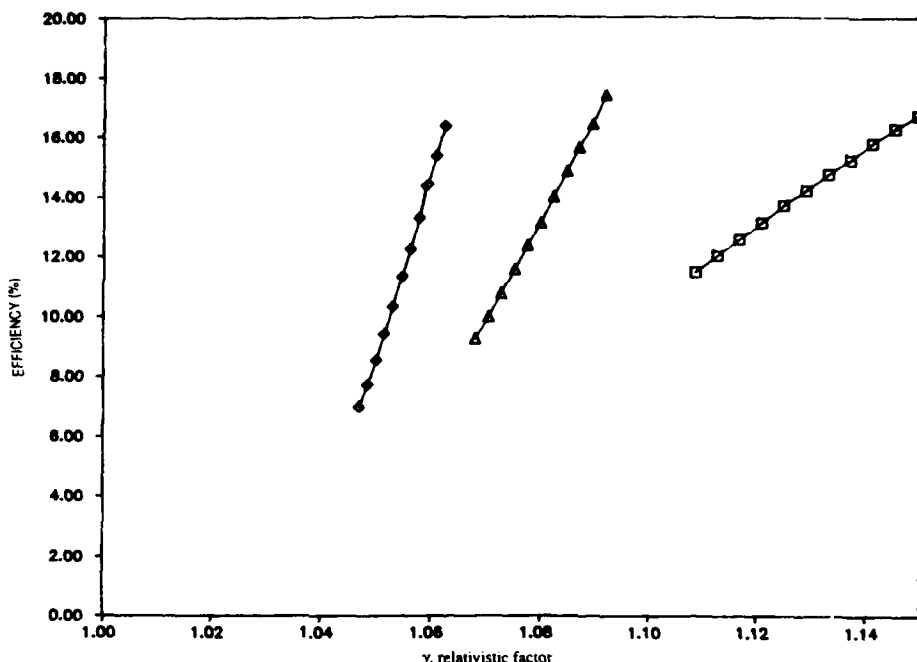


Figure 6. Efficiency versus relativistic factor (γ) for the 2π mode operating at the TE_{02} mode. $0.7 \leq R_L/a \leq 0.8$, $N = 8$ (\square), 10 (Δ) and 12 (\diamond). Originated from $J'_0 = 0$, second zero.

are thus determined. Three branches of waveguide modes whose dispersion relations are shown in Fig. 2 have been considered. A comparison between the performance of π mode and 2π mode operation has also been made.

The present study leads to the following conclusions.

- Operating the waveguide mode in the harmonic branch (i.e. it reduces to the TE_{N_01} mode for $b/a = 1$), the π mode tube ($N = 2N_0$) is found to be about twice as efficient as the 2π mode tube ($N = N_0$).
- The optimum structures of the 2π mode tubes are determined to be $b/a = 2$ for $N_0 = 8$, $b/a = 1.5$ for $N_0 = 10$ and $b/a = 1.3$ for $N_0 = 12$. The optimum efficiency for each corresponding tube is found to be 15.5% with $\gamma_0 = 1.14$, 5.5% with $\gamma_0 = 1.36$, and 3% with $\gamma_0 = 1.75$.
- In the fundamental branch (i.e. the waveguide mode becomes TE_{02} for $b/a = 1$), tubes can only operate at 2π mode. A common value of $b/a = 1.3$ is found to be the optimized tube structure for all three N_0 cases. The optimum efficiency is found to be about 18% for all three different N_0 tubes, except the required beam energy for each tube is different, $\gamma_0 = 1.15$ for $N_0 = 8$, $\gamma_0 = 1.09$ for $N_0 = 10$ and $\gamma_0 = 1.065$ for $N_0 = 12$.

ACKNOWLEDGMENT

This work was supported by the Air Force Office of Scientific Research, Grant No. AFOSR-85-0316.

REFERENCES

CHU, K. R., and DIALETIS, D., 1984, *International Journal of Infrared and Millimeter Waves*, **5**, 37.

GRANATSTEIN, V. L., SPRANGLE, P., PARKER, R. K., and HERNDEN, M., 1975, *Journal of Applied Physics* **46**, 202.

KUO, S. P., KUO, S. C., CHEO, B. R., and LEE, M. C., 1986, *International Journal of Infrared and Millimeter Waves*, **7**, 635.

KUO, S. P., TIONG, K. K., MILLER, P. E., and NAMKUNG, W., 1988, *Physics of Fluids*, **31**, 1821.

LAU, Y. Y., and BARNETT, L. R., 1982, *International Journal of Infrared and Millimeter Waves*, **3**, 619.

LAWSON, W., and STRIFFLER, C. D., 1986, *Physics of Fluids*, **29**, 1682.

MCMULLIN, W. A., and G. BEKEFI, 1981, *Applied Physics Letters*, **39**, 845.

NAMKUNG, W., 1986, *Physics of Fluids*, **27**, 329.

PALEVSKY, A., and BEKEFI, G., 1979, *Physics of Fluids*, **22**, 986.

TIONG, K. K., KUO, S. P., and KUO, S. C., 1987, *International Journal of Electronics*, **65**, 397.

Operation of a high harmonic cusptron oscillator

K. K. TIONG† and S. P. KUO†

A cusptron oscillator has been set up. It uses a 16-slot waveguide for the generation of the 16th cyclotron harmonic TE_{02} mode (2π -mode operation) and the 8th cyclotron harmonic TE_{81} mode (π -mode operation). The output frequencies are 12.5 GHz and 8.33 GHz, respectively. Moreover, a 15th cyclotron harmonic TE_{02} mode has also been generated at 10 GHz via peniotron instability.

1. Introduction

It is evident from most experimental indications that gyrotrons generally produce good operating efficiencies in the fundamental and second harmonic modes (Carmel *et al.* 1983, Kreischer and Temkin 1987, Granatstein and Alexeff 1987). However, when it is operating in higher harmonic modes or the whispering gallery modes, the efficiency drops dramatically. The information on the saturation efficiency of gyrotron operation at higher-order modes is therefore of considerable interest to a number of researchers (Chu 1978, McDermott *et al.* 1983, Kuo *et al.* 1986). Among them, Kuo *et al.* (1986) performed a non-linear analyses of gyrotron operation at harmonics as high as $N=8$. The results showed a progressive decrease in efficiency with increasing harmonic number. However the efficiency increases with increasing beam energy. The demand for high-power high-frequency sources motivates the search for many other novel ways of improving the operation of high harmonic gyrotrons. Further, it is also desirable that new devices should be reasonably compact, for applications such as space based radar systems, and also should offer a degree of tunability either in the CW range or the step range. Destler *et al.* (1981) showed that the efficiency of a gyrotron operating at higher harmonics can be improved by using a high energy rotating beam. The improvement lies in the fact that the Larmor radius of the electron beam is directly proportional to its energy. Therefore, by increasing the energy, the electron beam will be brought closer to the wall where the harmonic field is concentrated (Lawson *et al.* 1985). However, this feature will make the device rather bulky when the accelerator is required to produce electrons of energy higher than 500 keV. Other complications also arise from using high-voltage high-current beams. For example, the cavity size must be scaled correspondingly to handle the increase in dissipated power and high current operation in overmoded cavities leads to the problem of the suppression of parasitic modes which would otherwise complicate the mode purity controllability.

To improve the efficiency of a high harmonic gyrotron without using a high energy beam, a cusp-injected hollow beam system is introduced. The system has the attraction of maximizing the finite Larmor radius effect, which will enhance the beam-high-order modes interaction without using a high energy beam. Such a beam trajectory can be produced by passing an axially streaming, thin annular

Received 20 January 1990; revised 5 April 1990; accepted 14 June 1990.

† Weber Research Institute, Polytechnic University, Farmingdale, NY 11735, U.S.A.

electron ring through a cusp-magnetic field configuration created by magnetic field reversal. Using this system and with an appropriate guiding magnetic field in the interaction region, the E-layer produced can be positioned as close to the waveguide wall as physically permissible. However, other disadvantages including the loss of electrons in traversing such a field configuration and radial beam broadening may also negate some of the benefits of this system. It can also be shown that the selectivity of the higher-mode operation can be improved by the inclusion of periodic boundary slots in the resonant circuit. As the ratio of b/a exceeds a certain value, which depends on the number of slots, the slotted boundary creates a large periodic fringe field near the orbits of the concentrically circulating electrons, thereby enriching the harmonic contents of the RF fields as experienced by the electrons (Lau and Barnett 1982, Chu and Dialetis 1984, Lawson and Striffler 1986, Tiong *et al.* 1988). These added features have the advantage of making the device physically compact as the magnetic field strength required for high-harmonic radiation will be decreased proportionally to the harmonic number and the required beam energy for a given Larmor radius will also be reduced by the square of the harmonic number.

The experimental feasibility of such a device incorporating the previously described features was first demonstrated by NamKung (1984). In his work, a six-vane resonant circuit with $b/a=1.5$ was used. Radiation at 4.38 GHz with 500 W power was detected with a magnetic field strength of 260 G. In his later work, he is able to generate radiation at 10.4 kW power at 6 GHz (NamKung *et al.* 1987). The magnetic field strength required was 350 G. In the later report, it was noted that the 4.38 GHz radiation corresponds to the 4th harmonic and the efficiency is optimized to be 9% at the 9 kW power level, while that of 6 GHz corresponds to the 6th harmonic radiation. Later reports by Chojnacki *et al.* (1987), using the same system indicated radiation at 6.78 GHz at the 8th harmonic and 8.85 GHz at the 10th harmonic, where the radiated powers were reported as 9.1 kW and 2.2 kW, respectively.

In the present work, we extend the cusptron operation to even higher harmonics. It is noted that in all previous work on the cusptron, the mode of operation is on the TE_{01} branch of the dispersion curve. It is also our aim to operate the device in the TE_{N1} or TE_{OM} branches of the dispersion curves (i.e. the solution of the waveguide mode originating from the first zero of the N th harmonic or M th zero of the fundamental mode). The main advantage of such operation is the resultant high-frequency output with lower magnetic requirement. Other objectives include exploring the operation of the device in the π -mode configuration, which has been shown by particle simulation (Kuo *et al.* 1988, Tiong *et al.* 1990) to be more efficient in comparison to the more common 2π -mode operation.

In §2, descriptions of the background theories and particle simulation for the design of the tube are presented. The experimental set-up and results are presented in §3. Final conclusions and some perspectives of the work are discussed in §4.

2. Characteristic equations and particle simulations

The transverse wave number k of the TE mode fields in an N -slot cylindrical waveguide is given by (Kuo *et al.* 1988)

$$\frac{1}{2} \sum_{n=-\infty}^{+\infty} \left[\frac{\sin \Gamma \theta_0}{\Gamma \theta_0} \right]^2 \frac{J_\Gamma(ka)}{J'_\Gamma(ka)} = F(ka) \quad (1)$$

where the cut-off condition $k_z=0$ is assumed; $\Gamma=m+nN$; m is the mode index which determines the phase difference between slots; $m=0$ for 2π mode and $m=N/2$ for π mode; θ_0 is the half angle subtended by each slot;

$$F(k\rho) = \frac{[J_0(k\rho)Y'_0(kb) - J'_0(kb)Y_0(k\rho)]}{[J'_0(ka)Y'_0(kb) - J'_0(kb)Y'_0(ka)]}$$

a and b are the inner and outer radii of the waveguide; J_i and Y_i are the Bessel and Neumann functions, respectively; a 50% slot opening is considered so that $\theta_0=\pi/2N$.

In general, (1) has multiple roots k_j , $j=1, 2, 3, \dots$ for a given waveguide structure. Each root is a function of the ratio b/a , and defines a frequency range of operation. The dashed curves I and II presented in Fig. 1 represent the roots corresponding to the TE_{02} dispersion branch (2π mode only) and the TE_{81} dispersion branch (π mode only), respectively. For the π mode case, only the range $1 < b/a < 1.4$ is of interest since ka decreases drastically with b/a .

To achieve resonant interaction, we have to adjust the background magnetic field to a strength such that $\Omega=\omega_0/N_0$ for the N_0 th harmonic cyclotron resonance, where $\Omega=\Omega_0/\gamma$ is the relativistic electron cyclotron frequency and ω_0 is the eigenfrequency of the empty waveguide mode. As the resonance condition is met, the perturbations on the electron orbits are mainly introduced by the resonant component of the total force which has the slowest time variation. Consequently, only the resonant trajectory will be of interest. A set of self-consistent characteristic equations for the resonant trajectory of the electrons is thus derived to be (Kuo *et al.* 1988)

$$\frac{d}{dt} \alpha = AE_0 J'_{N_0}(\alpha) \cos \varphi \quad (2)$$

$$\frac{d}{dt} \varphi = -\Delta\omega + AE_0 \{(\Delta\omega/\omega) J_{N_0}(\alpha) + \frac{1}{\alpha} \frac{d}{d\alpha} [\alpha J'_{N_0}(\alpha)]\} \sin \varphi \quad (3)$$

where

$$\alpha = kv_1/\Omega \quad \text{and} \quad \varphi = N_0(\psi + \phi_0) - \int_0^t \Delta\omega(t) dt$$

E_0 is the amplitude of the wavefield;

$$\Delta\omega = \omega - N_0\Omega = \Delta\omega_0 + \omega_0(\gamma - \gamma_0)/\gamma, \quad \Delta\omega_0 = \omega - \omega_0, \quad \text{and} \quad \omega_0 = N\Omega_0/\gamma_0$$

and γ and α are related through the relation $\gamma^2 = 1 + (\Omega_0\alpha/\omega)^2$.

Since the field amplitude E_0 is going to vary during the interaction with electrons, it has to be determined self-consistently. This consideration can be included by coupling (2) and (3) to the energy conservation equation, which is given by

$$(\epsilon/8\pi a^2 N_0) \frac{d}{dt} E_0^2 = n_0 m c^2 \frac{d}{dt} \langle \gamma \rangle \quad (4)$$

where ' $\langle \rangle$ ' indicates an average over the initial random phase distribution of electrons; n_0 is the electron beam density averaged over the inner cross-section of the waveguide structure; ϵ is the effective dielectric constant of the waveguide structure for the mode under consideration and is given by (Kuo *et al.* 1988)

$$\begin{aligned} \epsilon = & \sum_{n=-\infty}^{+\infty} \left(\frac{\sin \Gamma \theta_0}{\Gamma} \right)^2 \left\{ 1 + \frac{1}{ka J_R'(ka)} + \left(1 - \frac{\Gamma^2}{k^2 a^2} \right) \frac{J_R^2(ka)}{J_R'(ka)} \right\} \\ & + \frac{\pi^2}{2N^2} \left\{ \left(\frac{b^2}{a^2} \right) G^2(kb) - G^2(ka) - (1 - \delta_{ab}) \left[1 + \frac{G(ka)}{ka} \right] \right\} \end{aligned} \quad (5)$$

with $G(k\rho) = F''(k\rho)$ and δ_{ab} is the Kronecker delta.

In order to couple (2)–(4) together, a phase average over the single electron motion is necessary. This is achieved numerically by solving the trajectories of a large number of electrons with a random initial phase distribution. Initially, the particles are set to be positioned symmetrically about the axis of the waveguide structure, and the energy of each particle is given by a predetermined value resulting from the cathode voltage. This distribution represents an unperturbed sample of the actual randomly distributed electrons in the ideal E-layer. With each increment of simulation time during program execution, the perturbation in each particle's position is computed by integrating (2) and (3); from this calculation, the particle energy can also be determined. By comparing the resulting average particle energy to the previous average particle energy, the energy transferred to the wavefield can be determined through (4). The next time-increment repeats the calculations using the perturbed position and energy values for the particles, along with the updated wavefield amplitude. In this simulation, it was found that 128 particles were sufficient to obtain accurate data. Adding more particles in the simulation will not improve the results over the accuracy of the numerical scheme—Los Alamos ordinary differential equation solver (LSODE). The temporal evolution of the wavefield amplitude can thus be determined and the saturation efficiency η of the output radiation can be calculated. The solid curves I and II in Fig. 1 show the functional dependence of η on b/a for 2π -mode 16th harmonic operation ($N_0=16$) in the TE_{02} mode, and for π -mode 8th harmonic operation ($N_0=8$) in the TE_{81} mode, respectively. In the calculation, the beam energy changes with b/a so that the ratio r_L/a can be fixed at a constant value 0.7, where r_L is the electron Larmor radius. This shows that the first peak of the efficiency (solid) curve I is located near $b/a=1.3$. The efficiency curve II for the TE_{81} , π mode is a monotonically increasing function of b/a with severe trade-off on the output frequency at $b/a=1.3$; the efficiency of the π mode is already much higher than that of the 2π mode. On the other hand, the operation frequency of π mode is still comparable to that of 2π mode. Therefore, $b/a=1.3$ is considered to be a good parameter for the design of a slotted waveguide able to be used for 2π - and π -mode operation with the same experimental set-up. The second peak of efficiency

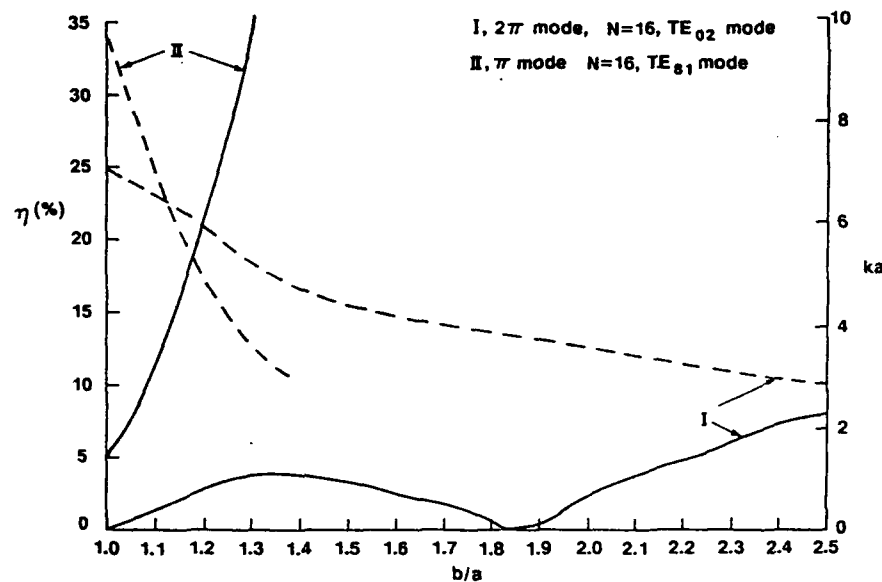


Figure 1. Efficiency and ka versus b/a for the 2π and π modes.

curve I is not considered because it requires a larger b/a value and also operates at a much lower output frequency for both the π and 2π modes.

3. Experiments and results

In the experimental set-up, twelve individually wound copper wire coils connected to three power supplies are used to produce the desired magnetic field profile. A cusp field centred at the anode location is produced by the three coils positioned in the upstream region together with the first three of the remaining nine placed in the downstream region. The other six coils in the downstream region are used to produce a uniform field inside the waveguide for cyclotron harmonic resonance interaction. Each coil can sustain a maximum of 20 A current (~ 0.1 T magnetic field) without overheating for an extended period of operation. The cusp transition width is substantially narrowed by a soft iron plate positioned between the upstream and downstream regions and jointed as part of the anode. The cusp transition width is measured to be about 0.5 cm. The system vacuum is maintained by an ion pump at about 10^{-8} Torr. A schematic of the set-up is shown in Fig. 2.

As discussed in § 2, $b/a = 1.3$ is a good choice for a 16-slot waveguide. The value $b/a = 1.3$ is therefore picked for the construction of the 10 cm long slotted waveguide whose photo is shown as Fig. 3. The corresponding ka values found from the dashed curves I and II of Fig. 1 are 5.14 for the TE_{02} 2π mode and 3.43 for the TE_{81} π mode, respectively. The inner radius $a = 1.98$ cm is chosen so that $0.65 < r_c/a < 0.75$, where r_c is the radius of the annular cathode. A hollow electron beam is produced from an annular thermionic cathode of radius 1.4 cm and radial thickness 0.16 cm with a Pierce-type focusing electrode. The electron axial energy is provided by a hard tube modulator with a maximum capability of 30 kV and

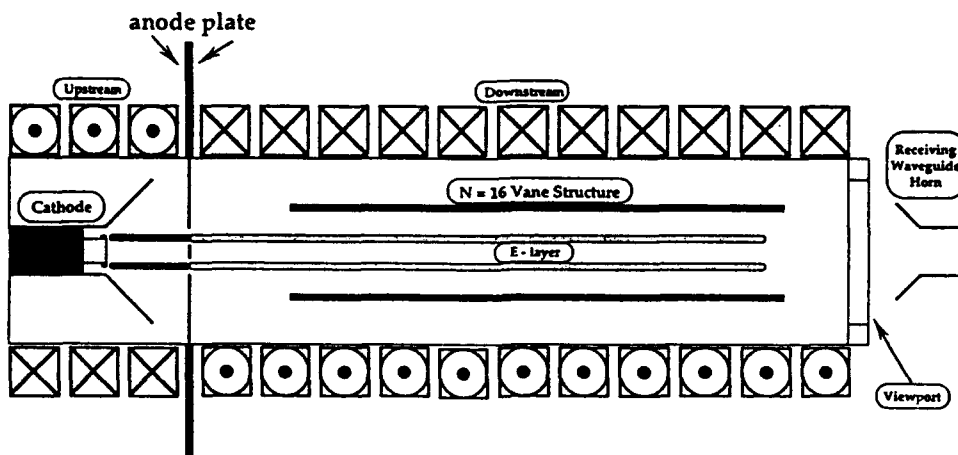


Figure 2. Schematic of the cusptron experiment.



Figure 3. Photograph of 16-slot waveguide ($b/a = 1.3$).

10 A current. The pulse width and pulse repetition rate are adjustable from 10–2 μ s and 200 Hz–1 kHz, respectively. The cathode is mounted on bellows coupled tubing to facilitate alignment and the adjustment of the cathode-anode gap without breaking the vacuum system. The anode with an annular slit of width 0.2 cm supported by three bridges is attached to the iron plate. The slit will allow the hollow beam to pass through the magnetic cusp transition region, where the $v_z \times B$ force converts the beam axial velocity v_z into the azimuthal velocity v_θ on

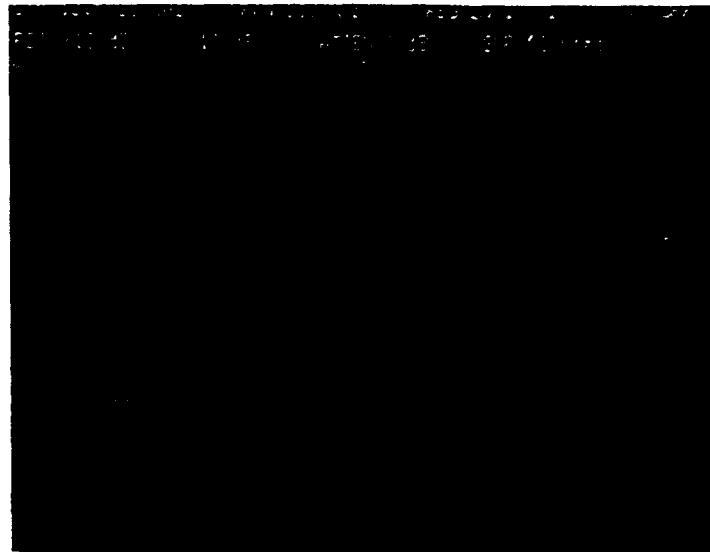


Figure 4. Spectrum analyser trace of 2π -mode radiation at 12.5 GHz, $V=16$ kV, and $I=0.5$ A.

the downstream side of the cusp transition. The 16-vane waveguide for the beam-wave interaction is placed immediately behind the anode in the downstream region.

Since the radius r_L of an ideal E-layer is equal to the radius of the hollow beam, it is thus fixed by the radius of the annular cathode r_c , i.e. $r_L=r_c$. From the relations

$$kc = N_0 \Omega_0 / \gamma_0, \quad v_\perp = (\Omega_0 / \gamma_0) r_L \quad \text{and} \quad \gamma_0 = (1 - v_\perp^2/c^2)^{-1/2}$$

we obtain

$$\gamma_0 = [1 - (kr_c/N_0)^2]^{-1/2}, \quad \Omega_0 = \frac{\gamma_0 \omega}{N_0} \quad \text{and} \quad \omega = kc$$

Using the specific values $1.3 < r_c < 1.5$ cm, $a = 1.98$ cm and $ka = 5.14$ for $N_0 = 16$ (and $ka = 3.43$ for $N_0 = 8$), the operating voltage V_0 , magnetic field B_0 , and cut-off frequencies f_0 are determined to be $12 < V_0 < 16$ kV ($21.5 < V_0 < 21$ kV), 0.0284 T (0.0387 T) and 12.4 GHz (8.27 GHz), respectively. In the actual experiments with the constructed waveguides, signals corresponding to both 2π - and π -mode operation in the expected frequency regions are detected. Presented in Figs 4 and 5 are spectral outputs recorded by the HP spectrum analyser (8569B). The signal at 12.5 GHz shown in Fig. 4 is the output of 2π -mode radiation, while the signal at 8.33 GHz shown in Fig. 5 is the output of π -mode radiation. In both cases, the radiation frequencies are slightly above the cut-off frequency of the respective modes. We have also operated the tube at about the same beam voltage and current, i.e. 16 kV and 0.5 A, respectively. It is noted that the above-mentioned operating voltages are calculated for an ideal cusp field. In the actual experiment, the cusp field is far from ideal and slightly asymmetric. Thus, the 16 kV electron beam can still pass through the cusp field with a higher downstream magnetic field

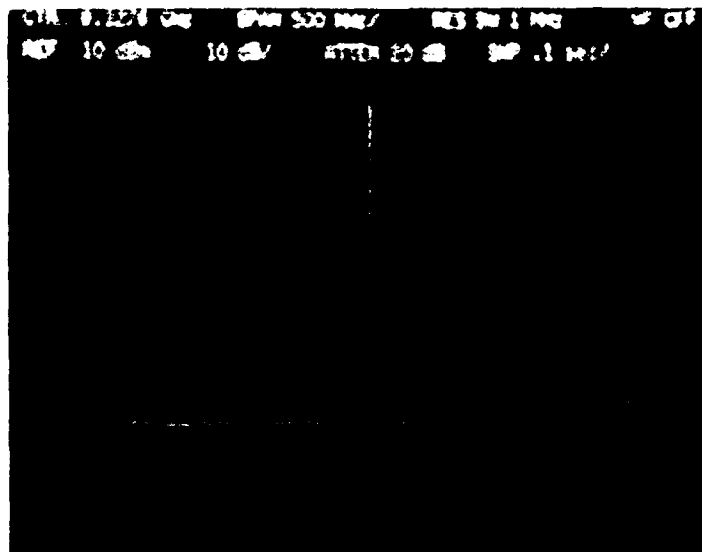


Figure 5. Spectrum analyser trace of π -mode radiation at 8.33 GHz, $V=16$ kV, and $I=0.5$ A.

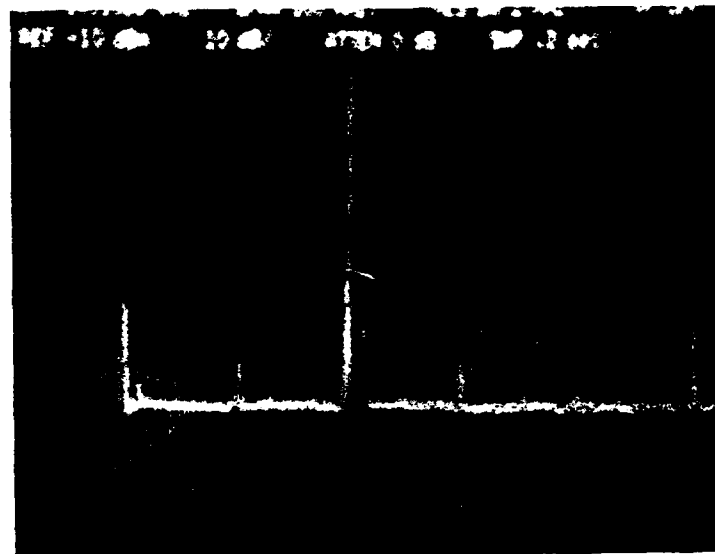


Figure 6. Spectrum analyser trace of radiation at 10.0 GHz, $V=16$ kV, and $I=0.5$ A.

for the π -mode case than the corresponding cut-off magnetic field for the ideal case. It is also noted that these two modes occur at different magnetic fields and can be separated easily. The fact that only single line at each frequency is generated suggests that the waveguide structure can indeed minimize the competition between the modes. The spurious signal at 10.0 GHz shown in Fig. 6 is also excited for this waveguide. It can also be separated from 2π -mode signal by a

slight change in the downstream guiding magnetic field. At present, this signal is tentatively frequency matched to the 15th harmonic due to the peniotron mode.

4. Discussion and conclusion

In the present operation, it is noted that the detected signal at 12.5 GHz, although distinct, is relatively weak. The strongest radiation is at 8.33 GHz, and at 10 GHz the power level is less. It should be noted that the detected signal power level does represent the real output power. This is due mainly to the inadequacy of the coupling system that guides the radiation from the circular resonant structure to the rectangular receiving antenna horn. In the present set-up, the multivane waveguide has a circular cross-sections of radii $a = 1.98 \text{ cm}$ and $b = 2.574 \text{ cm}$. The structure sits inside a chamber of radius 5.08 cm. Between the termination of the resonant structure and the end view port is a high voltage break of 5" length which is installed to monitor the beam current in order to determine the actual input beam power. This mismatch in dimension will cause a large reflection of radiated power back either through the waveguide or the gap between the waveguide and the chamber. The second mismatch is in the viewport, which is 0.571 cm thick. The manufacturer-listed transmission range for $0.32 \mu\text{m} < \lambda < 2.7 \mu\text{m}$ is 93%. We would expect the transmission to be smaller in the centimeter range in which we currently operate. The third mismatch is due to the use of an x-band rectangular horn to receive the output signal. In addition to the large cross-section difference in the radiating aperture and the receiving horn, this mismatch will effectively attenuate the signal prior to detection. Moreover, in the actual experiment, when the horn is rotated about 45° to the vertical polarization, it is discovered that the detected 8.3 GHz signal is maximized. From this observation, we can identify the polarization direction of this signal. However, this polarization is different for different modes. This strongly suggested that there is a need to design a circular-to-rectangular waveguide coupler in order to optimize the gain of the receiver. Therefore, these factors must be considered to calibrate the detected signals in order to determine the actual output power of each mode. Nevertheless, after the calibration the detected signals are still lower than the theoretical prediction. There are several candidates which may contribute to the discrepancy. The most dominant factors are:

- (1) the finite thickness of the annular cathode, which will cause an axial energy spread of the E-layer;
- (2) the non-ideal cusp field will lead to the problem of radial broadening and coherent off-centring of the E-layer (non-axisymmetric E-layer).

Another factor which affects the overall operating efficiency of the device is that a large percentage of the electrons are lost during passage through the anode plate. This is an inherent problem of the cusp field beam forming system. In order to achieve a narrower cusp transition width, an iron plate is constructed with an annular slit which is slightly larger than the radial thickness of the cathode. As a result, radial spread in the electron Larmor radius may lead to the loss of electrons through collision with the anode plate even before the beam's entry into the downstream side of the system. Experimentally, more than 50% of the electrons are lost through the anode.

In conclusion, we have detected radiation signals at the designed frequencies at

both the 2π and π modes. A signal at 10.0 GHz is also excited and has been frequency matched to the 15th harmonic. The detected power level of the π mode is much higher than that of the 2π mode, but the overall detected power level remains lower than that predicted theoretically, owing mainly to the poor receiving unit. In order to determine the actual radiated power, we should have to account for the losses due to the explained factors above. A comparison of the cross-section of the receiving horn with the window will add 10 dB to the detected signal. An estimated 20 dB loss is attributed to the mismatch in the dimensions of the waveguide and the chamber. A probable 10 dB loss is assigned to the reflection by the window. Finally, a 15 dB loss is added to account for the difference in geometry of the radiating and receiving units. Therefore a total loss of 55 dB must be taken into consideration to estimate the actual power output. For 2π -mode operation, the spectrum analyser trace gives a signal level of -18 dBm. With 55 dB added, the estimated radiated power is 37 dBm, or 5 W. Compare this with the theoretical prediction of 6.76% for a 16 kV 0.5 A beam (experimental parameters), i.e. 540 W. The corrected efficiency is still low. For π -mode operation, the estimated power is ~1.26 kW which compares favorably with a theoretical prediction of 2.4 kW (30% efficiency) in view of the less than ideal operating conditions as explained earlier. For the 10 GHz signal, the estimated power is about 500 W for the beam power used in other operations. It is noted that in the work of Chojnacki *et al.* (1987), the signal level from their spectrum analyser trace is about the same as our π -mode signal. However, Chojnacki *et al.* (1987) claimed a power level of 9.1 kW. In order to verify the results and to eliminate the rough estimation we have employed here, a better coupling system is required. This can be done by connecting a coupler having a cylindrical front end gradually tapered to a rectangular waveguide directly onto the resonant structure. A double-stub tuner should also be installed in the connection between the waveguide and the coupler to minimize the reflection incurred by the discontinuity in the structures. Nevertheless, in the present operating conditions in terms of signal controllability and step tunability this device has shown promise as a viable radiation source.

ACKNOWLEDGMENT

This work was supported by the Air Force Office of Scientific Research, Grant No. AFOSR-85-0316. Useful discussions with De W. NamKung is appreciated.

REFERENCES

- CARMEL, Y., CHU, K. R., READ, M., GANGULY, A. K., DIALETIS, D., SEELEY, R., LEVINE, J. S., and GRANATSTEIN, V. L., 1983, Realization of a stable and highly efficient gyrotron for controlled fusion research. *Physical Review Letters*, **50**, 112-116.
- CHOJNACKI, E., DESTLER, W. W., LAWSON, W., and NAMKUNG, W., 1987, Studies of microwave radiation from a low energy rotating electron beam in a multiresonator magnetron cavity. *Journal of Applied Physics*, **61**, 1268-1275.
- CHU, K. R., 1978, Theory of electron cyclotron laser interaction in a cavity at the harmonic frequencies. *Physics of Fluids*, **21**, 2354-2364.
- CHU, K. R., and DIALETIS, D., 1984, Theory of harmonic gyrotron oscillator with slotted resonant structure. *International Journal of Infrared and Millimeter Waves*, **5**, 37-55.
- CHU, K. R., DROBOT, A. T., SZU, H. H., and SPRANGLE, P., 1980, Theory and simulation of the gyrotron traveling wave amplifier operating at cyclotron harmonics. *I.E.E.E. Transactions on Microwave Theory and Techniques*, **28**, 313-317.
- DESTLER, W. W., WEILER, R. L., and STRIFFLER, C. D., 1981, High-power microwave generation from a rotating e-layer in a magnetron-type waveguide. *Applied Physics Letters*, **38**, 570-572.

GRANATSTEIN, V. L., and ALEXEFF, I., 1987, *High Power Microwave Sources* (Artech House).

KREISDER, K. E., and TEMKIN, R. J., 1987, Single-mode operation of a high-power, step-tunable gyrotron. *Physical Review Letters*, **59**, 547–550.

KUO, S. P., KUO, S. C., CHEO, B. R., and LEE, M. C., 1986, Analysis of the harmonic gyrotron traveling wave amplifier. *International Journal of Infrared and Millimeter Waves*, **7**, 635–651.

KUO, S. P., TIONG, K. K., MILLER, P. E., and NAMKUNG, W., 1988, A comparative study for an eighth harmonic cusptron tube operating in the π mode and the 2π mode. *Physics of Fluids*, **31**, 1821–1923.

LAU, Y. Y., and BARNETT, L. R., 1982, Theory of a low magnetic field gyrotron (gyromagnetron). *International Journal of Infrared and Millimeter Waves*, **3**, 619–642.

LAWSON, W., DESTLER, W. W., and STRIFLER, C. D., 1985, High power microwave generation from a large orbit gyrotron in vane and hole-and-slot conducting wall geometries. *I.E.E.E. Transactions on Plasma Science*, **13**, 444–453.

LAWSON, W., and STRIFLER, C. D., 1986, A linear growth rate fluid formulation for large orbit annular electron layers with finite thickness. *Physics of Fluids*, **29**, 1682–1694.

MCDERMOTT, R. B., LUHMANN, N. C., JR, FURUNO, D. S., KUPISZEWSKI, A., and JORY, H. R., 1983, Operation of a millimeter wave harmonic gyrotron. *International Journal of Infrared and Millimeter Waves*, **4**, 639–661.

NAMKUNG, W., 1984, Observation of microwave generation from a cusptron device. *Physics of Fluids*, **27**, 329–330.

NAMKUNG, W., CHOE, J. Y., UHM, H. S., and AYRES, V., 1987, Operation of cusptron oscillator for sixth harmonic frequency generation with six-vane circuit. *Proceedings Particle Accelerator Conference*.

TIONG, K. K., KUO, S. P., and KUO, S. C., 1988, Optimization of the design of cusptron microwave oscillator. *International Journal of Electronics*, **65**, 397–408.

TIONG, K. K., KUO, S. P., and MILLER, P. E., 1990, Operational characteristics of a cusptron microwave oscillator. *International Journal of Electronics*, **68**, 127–136.

FILAMENTATION INSTABILITY OF MAGNETOSONIC WAVES IN THE SOLAR WIND ENVIRONMENT

S. P. Kuo

Weber Research Institute, Polytechnic University, Farmingdale, New York

M.C. Lee

Massachusetts Institute of Technology, Cambridge

Abstract. Intense magnetosonic waves, originally propagating at the right angle with the interplanetary magnetic field, can excite a purely growing mode along the interplanetary magnetic field together with two symmetric magnetosonic sidebands propagating obliquely across the magnetic field. This instability process leads to the filamentation of the magnetosonic pump waves. These two excited magnetosonic sideband modes propagate together perpendicularly across the magnetic field and, meanwhile, form a standing wave pattern along the magnetic field. The thresholds of this filamentation instability can be exceeded in the solar wind environment. It is predicted that the density fluctuations produced by the filamentation instability along the interplanetary magnetic field have wavelengths greater than, at least, a few Earth radii. The polarization of the obliquely propagating magnetosonic waves excited by the filamentation instability is determined by the characteristics of the magnetosonic pump waves and the environmental plasmas.

Introduction

Recently, there has been a considerable effort in the study of the stability of Alfvén waves in the space plasmas. It is attributed to the frequent appearance, as detected by the space crafts, of large-amplitude Alfvén waves in the high-speed streams of the solar wind [Abraham-Shranner and Feldman, 1977], in the upstream Jovian bow shocks [Goldstein et al., 1985], and in the interplanetary shocks [Vinas et al., 1984]. In general, these waves appear to be circular polarization and propagating along the background magnetic field. Moreover, the ISEE 1 and 2 spacecrafts have detected both magnetosonic waves and Alfvén waves propagating upstream into the solar wind with phase velocities much less than the solar wind velocity. Hence, these waves are blown backward over the spacecraft and, consequently, an apparent change in polarization of waves occurs. Intrinsically right (left) hand polarized waves are seen to have an apparent left (right) handed polarization in spacecraft records [Hoppe and Russell, 1983].

The parametric decay instability and modulation instability of large-amplitude, circularly polarized Alfvén waves propagating in the solar wind along the magnetic field have been analyzed extensively by Lashmore-Davies [1976], Goldstein [1978], Derby [1978], Wong and Goldstein [1986], Longtin and Sonnerup [1986], and Terasawa et al [1986]. The filamentation instability, competing with these instabilities, can break up the large-amplitude Alfvén waves and induce not only plasma density fluctuations but magnetostatic fluctuations [Kuo et al., 1988]. Starting from small perturbations in plasma density, the filamentation instability gives rise to a modulation of the

plasma dielectric constant and then wave distribution that, in turn, enhances the density perturbations.

The modulation instability has also been analyzed in the region that describes the nonlinear evolution of the Alfvén wave propagating along a background magnetic field. It is shown that this evolution can be governed by a single "derivative nonlinear Schrödinger equation" [Mjølhus, 1976; Spangler, 1986; Hada et al., 1989]. The possible applications of Alfvén solitons to solar and astrophysical plasmas have been discussed by Ovenden et al [1983] and Spangler [1985].

While significant research has been directed to the Alfvén waves, the magnetosonic waves have received much less attention. The magnetosonic waves are hybrid and elliptically polarized modes that can propagate obliquely across the magnetic field. They become decoupled from the Alfvén waves when the direction of their propagation is exactly perpendicular to the ambient magnetic field. The purpose of the present work is to investigate the filamentation instability of the magnetosonic waves that propagate perpendicularly across the magnetic field. This instability excited obliquely propagating magnetosonic sideband modes. The concomitantly excited nonoscillatory (purely growing) modes have their wave normal parallel to the magnetic field. By contrast, the purely growing modes excited by the filamentation instability of Alfvén waves are magnetic field-aligned [Kuo et al., 1988, 1989]. Hence, the characteristics of the filamentation instability under consideration are distinctively different from those of the instability discussed in our previous work [Kuo et al., 1988, 1989].

This paper is organized as follows. The coupled mode equations are derived in section 2. They show how the magnetosonic sidebands and the purely growing modes are parametrically coupled through the magnetosonic pump wave. In section 3 the dispersion relation is obtained and analyzed to derive the threshold conditions and the growth rates of the filamentation instability. The relevance of the present work to some observations is discussed. Finally presented in section 4 are summary and conclusions.

Filamentation Instability of Magnetosonic Waves

Consider a magnetosonic wave propagating perpendicularly across the interplanetary magnetic field $\vec{B}_0 = \hat{z}B_0$. Its wave magnetic field is represented by

$$\vec{B}_p = \hat{z}B_p \exp[i(k_0 x - \omega_0 t)] + c.c. \quad (1)$$

where the unperturbed wave field intensity B_p is assumed to be constant and a real quantity for simplicity. The wave number k_0 and the angular frequency ω_0 are related by the dispersion relation $\omega_0^2 = k_0^2(v_A^2 + c_s^2)$, wherein v_A and c_s are the Alfvén speed and the ion acoustic speed, respectively. The velocity

responses of electrons and ions to the magnetosonic pump wave can be written as

$$\begin{aligned}\vec{v}_{pe} &= [\hat{x} + i(k^2 v_A^2 / \omega_0 \Omega_i) \hat{y}] (\omega_0 / k_0) (B_p / B_0) \exp[i(k_0 x - \omega_0 t)] \\ &\quad + \text{c.c.} \\ \vec{v}_{pi} &= \hat{x} (\omega_0 / k_0) (B_p / B_0) \exp[i(k_0 x - \omega_0 t)] + \text{c.c.} \quad (2)\end{aligned}$$

In the following we will investigate a filamentation instability which can break up a large-amplitude magnetosonic wave into filaments. The magnetosonic wave is assumed to be initially uniform as described by (1) for simplicity. The filamentation instability results from small fluctuations in plasma density which lead to modulation of plasma dielectric constant and spatial wave distribution, which, in turn, enhance the plasma density fluctuations. Such a positive feedback process involves a four-wave coupling process: through the magnetosonic pump wave (ω_0, \vec{k}_0), two side-band perturbations (ω_{\pm}) are coupled with a purely growing density perturbation (ω, \vec{k}). The wave frequency and wave vector matching conditions, are $\omega_{\pm} - \omega = \omega_0 - \omega + \omega^*$ and $\vec{k}_{\pm} = \vec{k}_0 + \vec{k}$, are satisfied where the asterisk denotes the complex conjugate. Illustrated in Figure 1 is the wavevector matching condition, showing the relative orientation of these wave vectors. It will be shown that these perturbations can be excited simultaneously. In other words, they grow exponentially with the same growth rate, $\gamma = -i\omega$ at the expense of magnetosonic pump wave energy. This instability requires a threshold to occur, which is going to be determined later. In the analysis of filamentation instability, pump field intensity is assumed to be a constant maintained by a source. Pump depletion effect which may contribute to the saturation of filamentation instability is, therefore, ignored within the present framework of instability analysis.

Our proposed theory is developed on the basis of the two-fluid plasma model. The fluid model is, in general, valid provided that the condition $k^2 c_s^2 / \Omega_i^2 \ll 1$ is satisfied where k , c_s , and Ω_i are the wave number of the purely growing mode, the ion acoustic speed, and the ion gyrofrequency, respectively. Therefore, the analysis of filamentation instability is limited to the region of $k/k_0 \lesssim 1.2$. To analyze the instability,

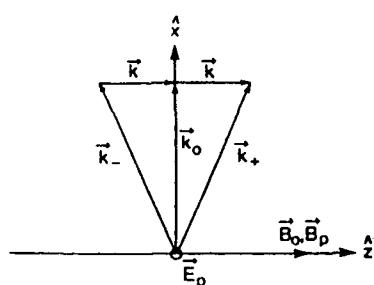


Fig. 1. The relative orientation and wave vector matching relation for the magnetosonic pump (ω_0, \vec{k}_0), two sidebands ($\omega_{\pm}, \vec{k}_{\pm}$) and the purely growing mode (ω, \vec{k}) as required in the proposed four-wave coupling process.

the complete set of fluid equations will be linearized with respect to the first-order perturbations in physical quantities such as density (n), velocity (v), wave electric field (\vec{E}) and wave magnetic field (\vec{B}). These first-order physical quantities associated with the sideband modes are denoted by δn_{\pm} , $\delta \vec{v}_{ej\pm}$, $\delta \vec{E}_{\pm}$, and $\delta \vec{B}_{\pm}$ those associated with the purely growing mode n_s , \vec{v}_{ses} , \vec{E}_s , and \vec{B}_s . Thus, the total density is given by $n = n_0 + n_s + (\delta n_+ + \delta n_- + \text{c.c.})$; similarly, $\vec{v}_{ej} = \vec{v}_{ses} + (\vec{v}_{pej} + \delta \vec{v}_{ej+} + \delta \vec{v}_{ej-} + \text{c.c.})$, $\vec{E} = \vec{E}_s + (\vec{E}_p + \delta \vec{E}_+ + \delta \vec{E}_- + \text{c.c.})$, and $\vec{B} = \vec{B}_0 + (\vec{B}_p + \delta \vec{B}_+ + \delta \vec{B}_- + \text{c.c.})$ for the concerned four-wave interaction process.

The purely growing mode is associated with electrostatic disturbances, varying spatially along the magnetic field, i.e., $\vec{k} = \hat{z}k$. The fluid equations used to derive the coupled mode equation for the purely growing mode include the linearized continuity equations for electrons and ions:

$$\frac{\partial n_s}{\partial t} + n_0 \frac{\partial}{\partial z} v_{ses} = 0 = \frac{\partial}{\partial t} n_s + n_0 \frac{\partial}{\partial z} v_{siz} \quad (3)$$

and the combined linearized equations of motion for electrons and ions:

$$\begin{aligned}m_e \frac{\partial}{\partial t} v_{ses} + m_i \frac{\partial}{\partial t} v_{siz} + (F_{es} \\ + F_{is}) = -m_i (c_s^2/n_0) \frac{\partial}{\partial t} n_s\end{aligned}$$

In deriving the above equations, quasi-neutrality has been assumed. F_{es} and F_{is} represent the z components of the nonlinear Lorentz forces experienced by electrons and ions, respectively, namely, $F_{eis} = -m_{ej}(\vec{v}_{ej} \cdot \nabla \vec{v}_{ej}) + q_{ej}(\langle \vec{v}_{ej}/c \rangle \times \vec{B})_s$ where angle brackets denote the time average over the pump wave period. The explicit expressions of F_{eis} are given by

$$\begin{aligned}F_{eis}/m_{ej} = \frac{\partial}{\partial z} (\vec{v}_{pej} \cdot \delta \vec{v}_{ej}) \\ + i \epsilon_{ej} \left(\frac{n_{ej}}{\omega_0} \right) \frac{\partial}{\partial z} [\delta v_{eix}^* v_{pejy} - v_{pejx} \delta v_{ejy}^*] + \text{c.c.} \quad (4)\end{aligned}$$

where $\delta \vec{v}_{ej} = \delta \vec{v}_{ej+} + \delta \vec{v}_{ej-}$ is the velocity responses of electrons and ions to the combined sideband mode; $\epsilon_{ej}(\epsilon_i) = +1(-1)$. The expression, (4) reduces to the form of ponderomotive force in an unmagnetized plasma. Without losing the generality, the density fluctuations of the purely growing mode can be expressed as

$$n_s = \tilde{n}_s \exp(i\gamma t) \cos kz$$

where \tilde{n}_s and γ are the real amplitude and the growth rate of the density fluctuations, respectively.

Combining the equations in (3) yields the coupled mode equation for the purely growing mode as

$$(\gamma^2 + k^2 c_s^2)(\tilde{n}_s/n_0) = (k/m_i)(\tilde{F}_{es} + \tilde{F}_{is}) \quad (5)$$

where $F_{eis} = \tilde{F}_{eis} \exp(\gamma t) \sin kz$ is assumed. One can see from (4) and (5) that the density fluctuations associated with the purely growing mode stem from the differential interaction of the magnetosonic pump wave and sideband modes. Hence, expressions for the physical quantities of the combined sideband mode have to be determined in a self-consistent manner. The purely growing mode is realized to be a nonlinearly driven mode. However, in the absence of the nonlinear Lorentz force, (5) reduces to the linear dispersion relation of the ion acoustic wave.

The magnetosonic sideband modes are excited through the beating current driven by the magnetosonic pump wave field in the density fluctuations of the purely growing mode. It should be noted that, since the magnetosonic pump wave propagates perpendicularly across the magnetic field and the purely growing mode oscillates spatially along the magnetic field, two magnetosonic sidebands are excited symmetrically around the pump wave and they propagate obliquely across the magnetic field (see Figure 1). Thus, these two sideband modes propagate together in the propagation direction of the pump wave and form a standing wave pattern along the magnetic field. In the following derivation of the coupled mode equations for the two sideband modes, we can, therefore, combine them into a single coupled mode equation for the combined sideband mode.

This combined sideband mode is characterized by the following physical quantities with self-consistent expressions:

$$\begin{aligned}\delta n &= \delta \tilde{n} \exp(\gamma t) \cos kz \exp[i(k_0 x - \omega_0 t)] + c.c. \\ \delta \vec{v}_{ej} &= [(\hat{x} \delta \tilde{v}_{eix} + i\hat{y} \delta \tilde{v}_{ey}) \cos kz + i\hat{z} \delta \tilde{v}_{eis} \sin kz] \exp(\gamma t) \\ &\quad \cdot \exp[i(k_0 x - \omega_0 t)] + c.c. \\ \delta \vec{B} &= [(k/k_0)(-i\hat{x} + \alpha \hat{y}) \sin kz + \hat{z} \cos kz] \delta \tilde{B} \exp(\gamma t) \\ &\quad \cdot \exp[i(k_0 x - \omega_0 t)] + c.c.\end{aligned}\quad (6)$$

where α , an unknown parameter defining the polarizations of the sideband modes, will be determined later on. The fluid equations, used to derive the coupled mode equation for the combined sideband mode, include the linearized continuity equations for electrons and ions:

$$\begin{aligned}\frac{\partial}{\partial t} (\delta n/n_0) + \nabla \cdot [\delta \vec{v}_e + (n_e/n_0) \vec{v}_{pe}] &= 0 \\ 0 &= \frac{\partial}{\partial t} (\delta n/n_0) + \nabla \cdot [\delta \vec{v}_i + (n_i/n_0) \vec{v}_{pi}]\end{aligned}\quad (7)$$

the linearized Maxwell equation for induction law:

$$\frac{\partial}{\partial t} (\delta \vec{B}/B_0) = \nabla \times (\delta \vec{v}_e \times \hat{z}) \quad (8)$$

the combined equations of motion for electrons and ions:

$$\frac{\partial}{\partial t} \delta \vec{v}_i = -c_s^2 \nabla (\delta n/n_0) + \Omega_i (\delta \vec{v}_i - \delta \vec{v}_e) \times \hat{z} \quad (9)$$

and the linearized Maxwell equation for Amperes' law:

$$\nabla \times (\delta \vec{B}/B_0) = (\Omega_i/v_A^2) [(\delta \vec{v}_i - \delta \vec{v}_e) + (n_i/n_0) (\vec{v}_{pi} - \vec{v}_{pe})] \quad (10)$$

Substituting (6) into equations (7)-(10), we obtain

$$\begin{aligned}\delta \tilde{v}_{ex} &= (\omega_0/k_0) (\delta \tilde{B}/B_0) \\ \delta \tilde{v}_{ey} &= \alpha (\omega_0/k_0) (\delta \tilde{B}/B_0) \\ \delta \tilde{v}_{ix} &= -(\omega_0/k_0) [(k_0^2 c_s^2 / \Omega_i^2) (\delta \tilde{n}/n_0) - (1 - \alpha \omega_0 / \Omega_i) (\delta \tilde{B}/B_0)] / (1 - \omega_0^2 / \Omega_i^2) \\ \delta \tilde{v}_{iy} &= (\omega_0/\Omega_i) [(k_0 c_s^2 / \omega_0) (\delta \tilde{n}/n_0) + [\alpha(\Omega_i/\omega_0) - 1] (\omega_0/k_0) (\delta \tilde{B}/B_0)] / (1 - \omega_0^2 / \Omega_i^2) \\ \delta \tilde{v}_{iz} &= (k c_s^2 / \omega_0) (\delta \tilde{n}/n_0) \\ \delta \tilde{v}_{ex} &= \delta \tilde{v}_{iz} + \alpha (k v_A^2 / \Omega_i) (\delta \tilde{B}/B_0) \\ \delta \tilde{n}/n_0 &= \{[(1 - \alpha \omega_0 / \Omega_i) / (1 - \omega_0^2 / \Omega_i^2)] (\delta \tilde{B}/B_0) \\ &\quad + (\tilde{n}_e/n_0) (B_p/B_0)\} / [1 - k^2 c_s^2 / \omega_0^2 + k_0^2 c_s^2 / (\Omega_i^2 - \omega_0^2)] \quad (11)\end{aligned}$$

Using the results in (11) together with the x and y components of (10), we can derive the following coupled mode equation for the combined sideband mode:

$$\begin{aligned}[\omega_0^2 - (k^2 + k_0^2)(v_A^2 + c_s^2) + k^2(k^2 + k_0^2)v_A^2 c_s^2 / \omega_0^2 \\ + \alpha(\omega_0/\Omega_i)[k_0^2 c_s^2 - \omega_0^2(1 - k^2 c_s^2 / \omega_0^2)]](\delta \tilde{B}/B_0) \\ = -k_0^2[v_A^2(1 - k^2 c_s^2 / \omega_0^2) - c_s^2](\tilde{n}_e/n_0)(B_p/B_0) \quad (12)\end{aligned}$$

as well as the expression for the parameter α

$$\alpha = (\omega_0/\Omega_i)[1 - 2(k^2 + k_0^2)c_s^2 / \omega_0^2] / [1 - c_s^2 / v_A^2 - (k^2 v_A^2 / \omega_0^2)(1 - k^2 c_s^2 / \omega_0^2)] \quad (13)$$

In the derivation of (12) and (13), $\omega_0^2 / \Omega_i^2 \ll 1$ has been assumed. Equation (12) shows that the magnetosonic sideband fields are produced by the magnetosonic pump field in the density fluctuations of the purely growing mode. Equations (5) and (12) thus form the complete set of coupled mode equations, which can be based on to analyze the proposed filamentation instability of magnetosonic waves in the solar wind environment.

Analysis of the Proposed Instability

The dispersion relation of the concerned instability can be derived from the two coupled mode equations, (5) and (12). Its derivation is briefly described as follows. With the aid of (2), (4), (6), and (11), the coupling term on the right-hand side of (5) can be expressed as

$$\begin{aligned}k(\tilde{F}_e + \tilde{F}_i)/m_i &= k^2[v_A^2 - c_s^2(1 - \alpha \omega_0 / \Omega_i) / (1 - k^2 c_s^2 / \omega_0^2)(B_p/B_0)(\delta \tilde{B}/B_0 + \delta \tilde{B}'/B_0) \\ &- 2(k^2 c_s^2 / (1 - k^2 c_s^2 / \omega_0^2))(\tilde{n}_e/n_0)(B_p/B_0)^2]\end{aligned}\quad (14)$$

Substituting (14) into (5) and combining it with (12) yield the dispersion relation

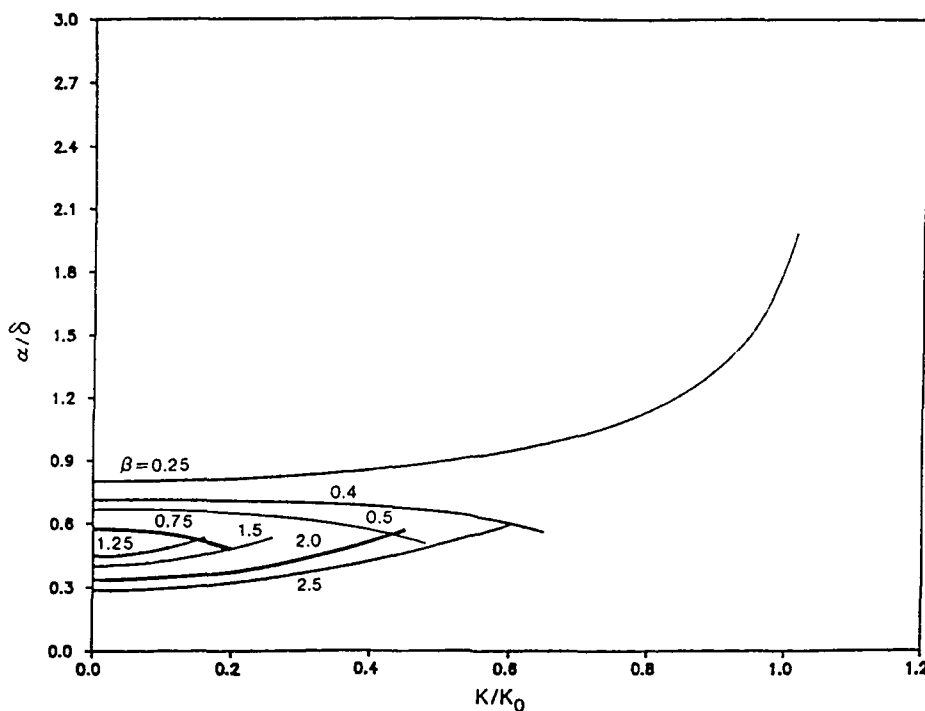


Fig. 2. α/δ versus k/k_0 for several selected values of β in the range of 0.25-2.5; it shows how the polarization of the excited magnetosonic sidebands is determined by the characteristics of the magnetosonic pump waves and the environmental plasmas.

$$\begin{aligned} \gamma^2 + k^2 c_s^2 = & 2k^2 v_A^2 \left\{ [1-\beta(1+\beta)/(\beta+1-\beta k^2/k_0^2)] \right. \\ & [1-\beta(1+\beta)(1-\alpha\delta)/(\beta+1-\beta k^2/k_0^2)] \\ & (\beta+1-\beta k^2/k_0^2)/[(\beta+1)^2 - \beta(1+k^2/k_0^2) + \alpha\delta(\beta+1)(k_0^2/k^2 - \beta)] \\ & \left. -(k^2/k_0^2)\beta(\beta+1)/(\beta+1-\beta k^2/k_0^2)(B_p/B_0)^2 \right\} \quad (15) \end{aligned}$$

where $\beta = c_s^2/v_A^2$ is the ratio of the plasma kinetic pressure to the background magnetic pressure, and $\delta = \omega_0/\Omega_i$.

Setting $\gamma=0$ in (15) determines the threshold field of the filamentation instability

$$\begin{aligned} (B_{\text{pth}}/B_0)^2 = & (k^2/2k_0^2)\beta(\beta+1)^2 - \beta(1+k^2/k_0^2) \\ & + \alpha\delta(\beta+1)(k_0^2/k^2 - \beta)/(1-\beta(\beta+1)) \\ & (\beta+1-\beta k^2/k_0^2)[1-\beta(\beta+1)(1-\alpha\delta)/(\beta+1-\beta k^2/k_0^2)] \\ & (\beta+1-\beta k^2/k_0^2) - (k^2/k_0^2)\beta(\beta+1)[(\beta+1)^2 - \beta(1+k^2/k_0^2) \\ & + \alpha\delta(\beta+1)(k_0^2/k^2 - \beta)]/(\beta+1-\beta k^2/k_0^2) \quad (16) \end{aligned}$$

In terms of (16), the growth rate of the instability derived from (15) is found to be

$$\gamma = [(B_p/B_{\text{pth}})^2 - 1]^{1/2} k c_s \quad (17)$$

The threshold condition defined by (16) is conveniently expressed for the normalized threshold field intensity (B_{pth}/B_0) as a function of the normalized wave number (k/k_0) . The parameters $\beta (= c_s^2/v_A^2)$, $\delta (= \omega_0/\Omega_i)$, and α (defined by (13)) characterize the solar wind plasmas and the

propagating magnetosonic waves. In fact, the parameter α can also be expressed in terms of (k/k_0) , δ , and β as follows:

$$\alpha = \delta[1 - 2(1 + (k/k_0)^2)\beta/(1 + \beta)/(1 - \beta[(k/k_0)^2 / (1 + \beta)][1 - (k/k_0)^2\beta/(1 + \beta)])] \quad (18)$$

Displayed in Figure 2 is (α/δ) as a function of (k/k_0) for several values of β chosen from the range of 0.25-2.5. The result shows that α is, in general, larger than one for $\delta \leq 0.3$ which is the region of practical interest. Especially, $\alpha \gg 1$ for $\beta \ll 1$ and $\delta \ll 1$. In this parameter range, the decay sidebands become linear polarization on the $y-z$ plane and are dominated in the nature of shear mode.

The threshold fields (B_{pth}/B_0) as a function of (k/k_0) are shown in Figures 3-6. For illustrative purposes, the values of β are again selected from the range of 0.25-2.5 and $\delta = 0.01, 0.03, 0.06$, or 0.3 is chosen. The corresponding growth rates, for $(B_p/B_0)^2 = 0.05$, as a function of k are given in Figures 7-10. Several outstanding features of the proposed instability can be seen from these figures. For instance, the threshold field generally increases with k , the wave number of the excited purely growing mode, and it finally reaches infinity at certain $k < k_0$. While the threshold field increases with β in the region $0 < \beta < 1$, it decreases with β for $\beta > 1$. The growth rate has a peak value (denoted by γ_{\max}) at certain k (denoted by k_m). We note that both γ_{\max} and k_m decrease with β for $0 < \beta < 1$, but they increase with β for $\beta > 1$. By contrast, while γ_{\max} decreases with δ , k_m increases with δ . The thresholds and growth rates of the instability vary with the magnetosonic wave frequency.

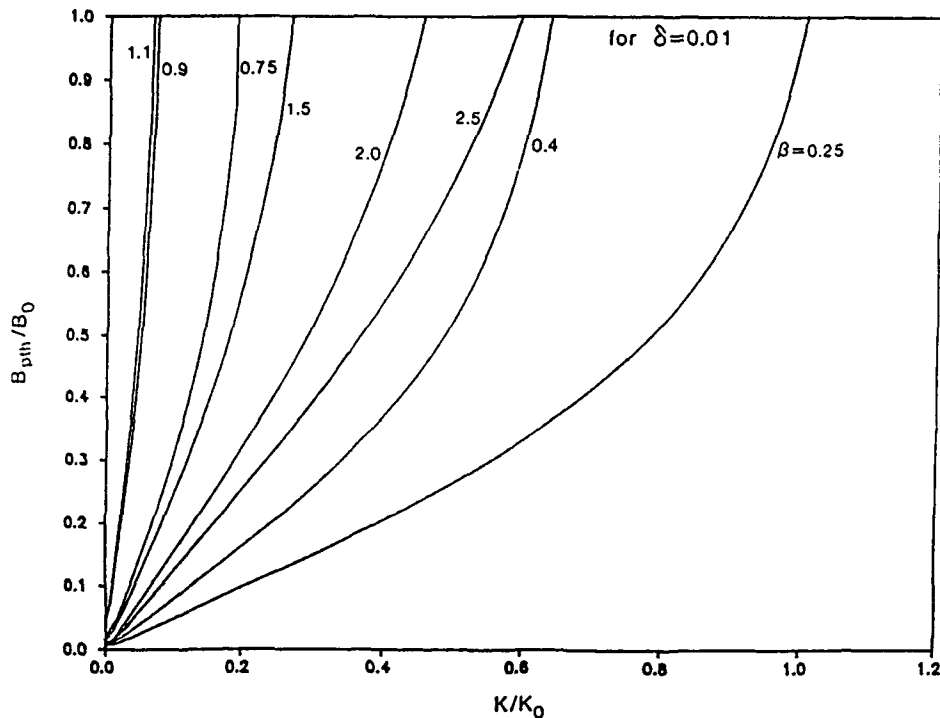


Fig. 3. The normalized threshold field intensity (B_p/B_0) versus (k/k_0) with several selected values of β in the range of 0.25-2.5 for $\delta=0.01$.

It is found that the threshold fields (growth rates) increase (decrease) with the magnetosonic wave frequency.

Let us base upon the observed characteristics of magnetosonic waves [Hoppe and Russell, 1983, and

references therein] to examine the excitation of the proposed filamentation instability. The magnetosonic waves observed by the ISEE 1 and 2 typically have low frequencies of order of 0.01 Hz, which is about 0.1 times the local proton gyrofrequency (i.e., $\delta=\omega_0/\Omega_p=0.1$).

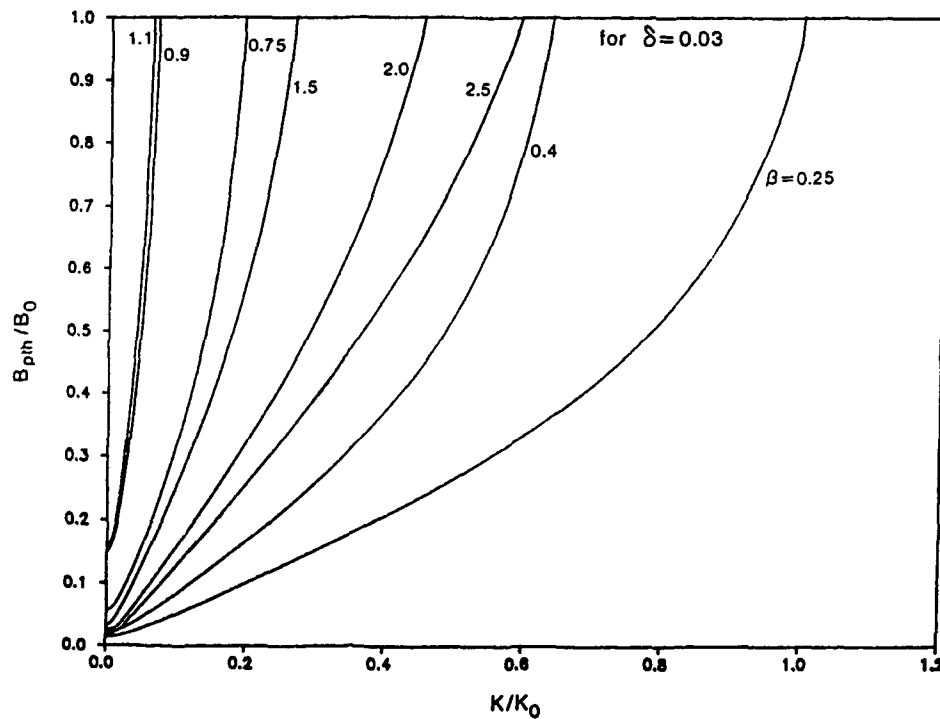
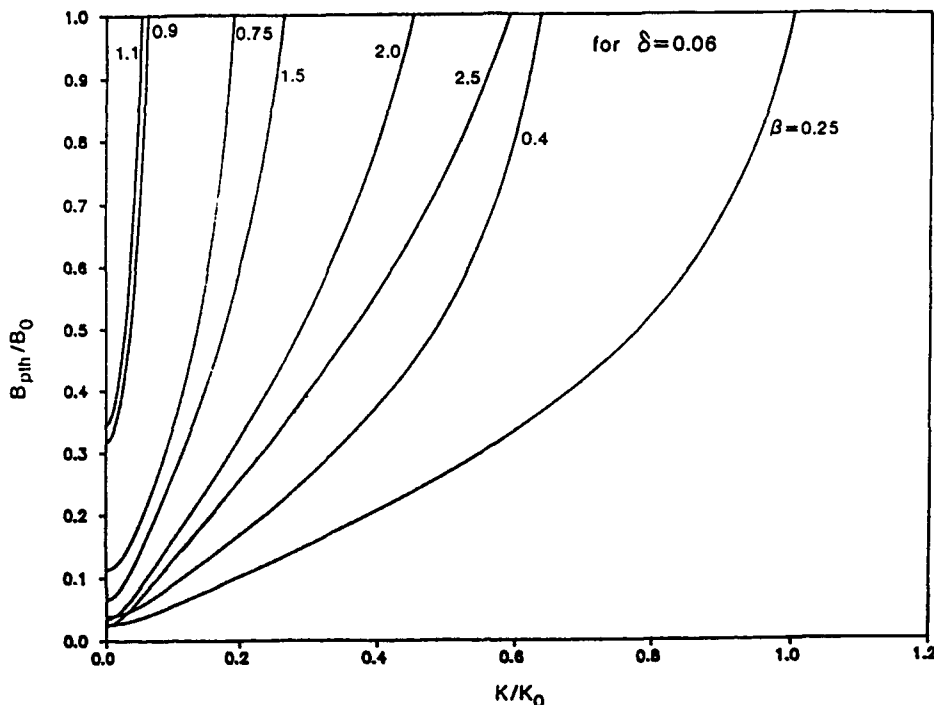
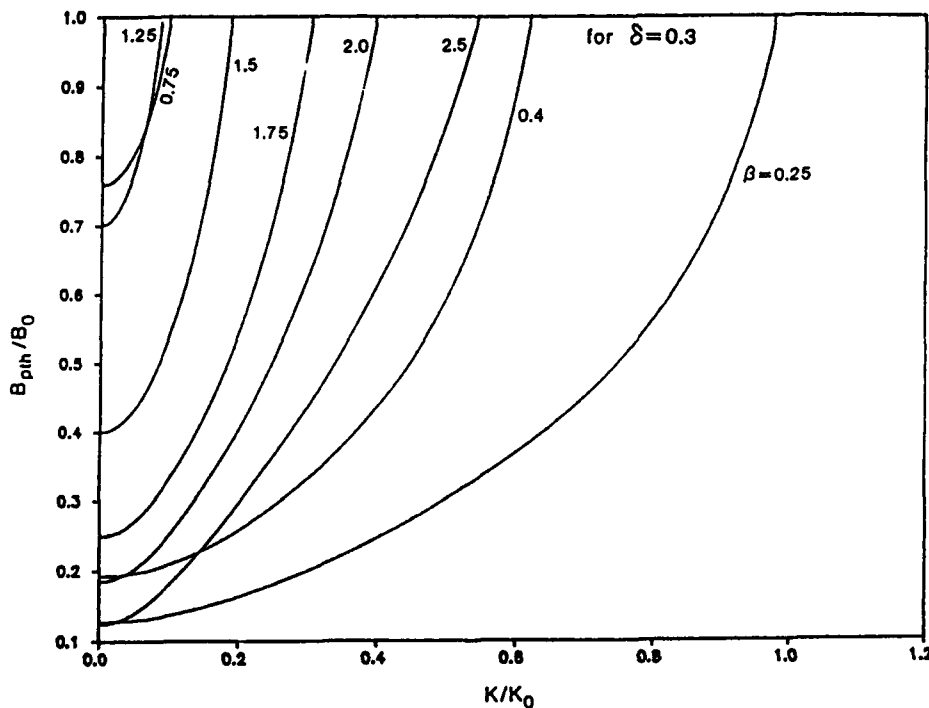


Fig. 4. (B_p/B_0) versus (k/k_0) for $\delta=0.03$.

Fig. 5. (B_p/B_0) versus (k/k_0) for $\delta=0.06$.

The local interplanetary magnetic field (B_0), therefore, is of order of 100 nT. The magnetosonic waves typically have amplitudes (B_p) of about 10 nT, namely, $B_p/B_0 \sim 0.1$ with wavelengths ~ 1 RE. The parameters adopted in the analysis of our proposed instability are generally in agreement with these observations. Under

the condition of $B_p/B_0 \sim 0.1$, the thresholds of the proposed instability can be exceeded for $k/k_0 (= \lambda_0/\lambda)$ less than 0.1 or so, where λ_0 and λ are the wavelength of the magnetosonic wave and the scale length of the excited purely growing mode, respectively. An important prediction of the proposed process is that

Fig. 6. (B_p/B_0) versus (k/k_0) for $\delta=0.3$.

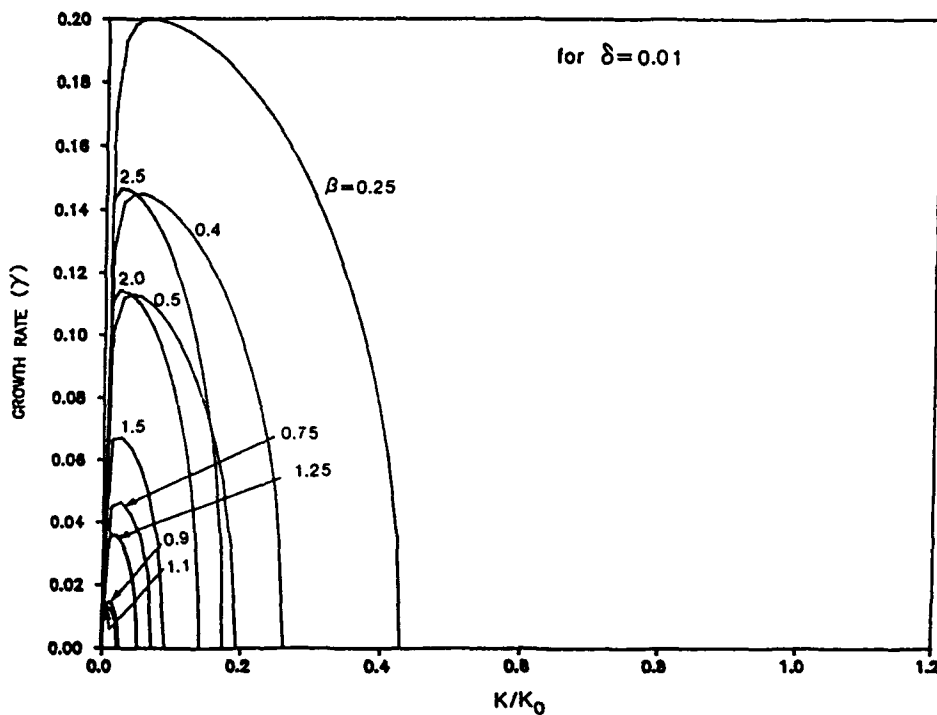


Fig. 7. The growth rate (γ), assuming $(B_p/B_0)^2=0.05$, as a function of k for $\delta=0.01$.

plasma density fluctuations with scale lengths longer than at least, a few RE (Earth radius) can be generated along the magnetic field by magnetosonic waves. The polarization of the obliquely propagating magnetosonic waves is determined by the value of α which in turn, is a function of the characteristic parameters of the environment: δ , β , and k_0 (see equation (18)).

However, we note that there seems to exist a discrepancy between the observed and the predicted propagation directions of magnetosonic waves. The waves upstream of Earth's bow shock with frequencies of 0.01 Hz were observed to propagate nearly parallel to the magnetic field, while the predicted magnetosonic waves propagate obliquely across the field. We suspect that this

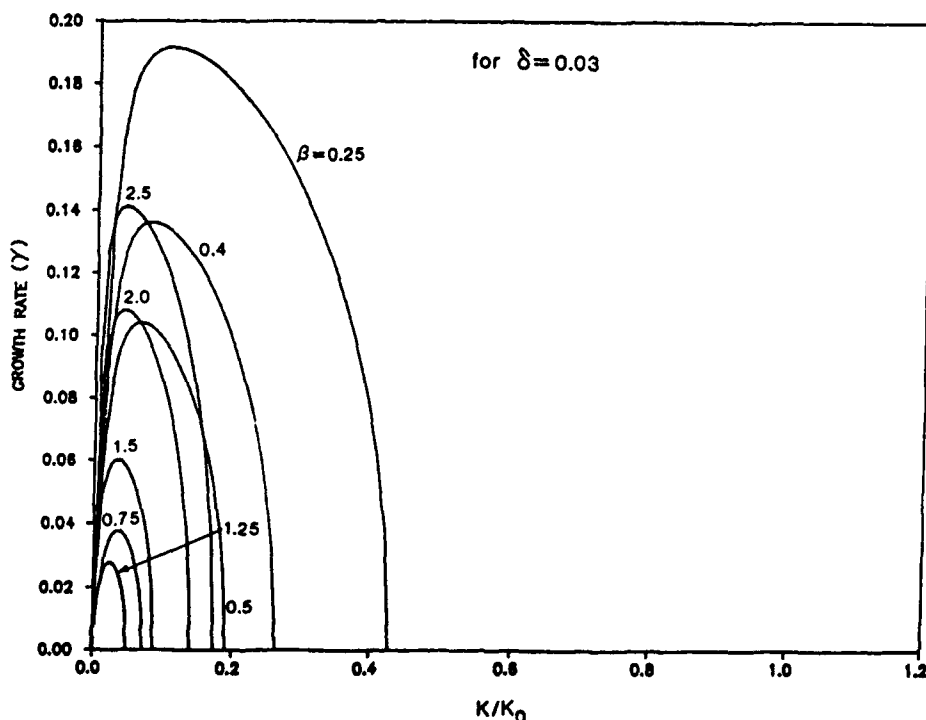
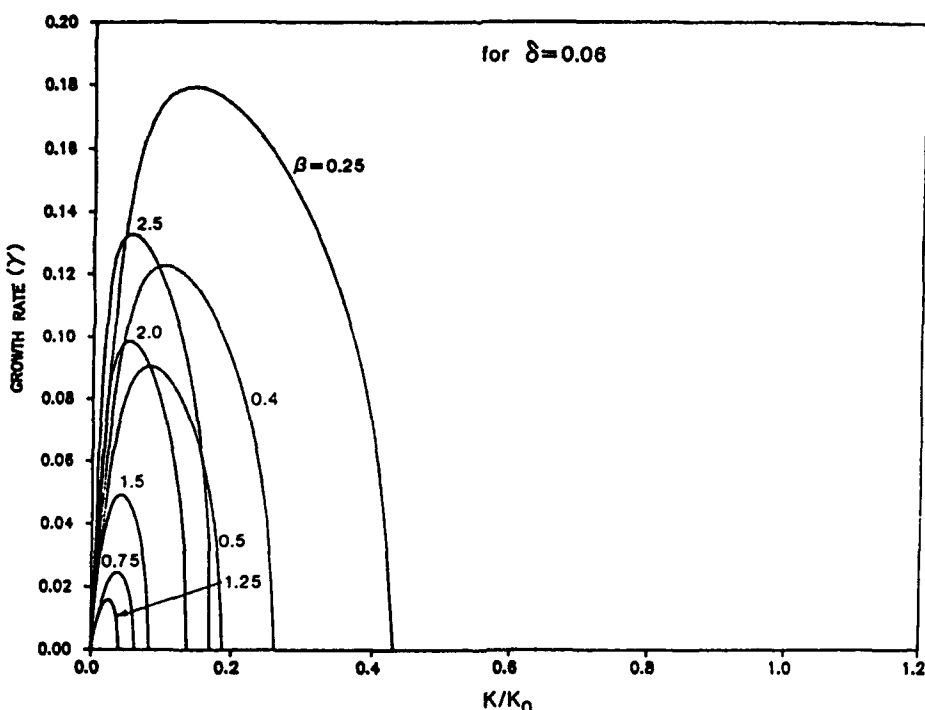


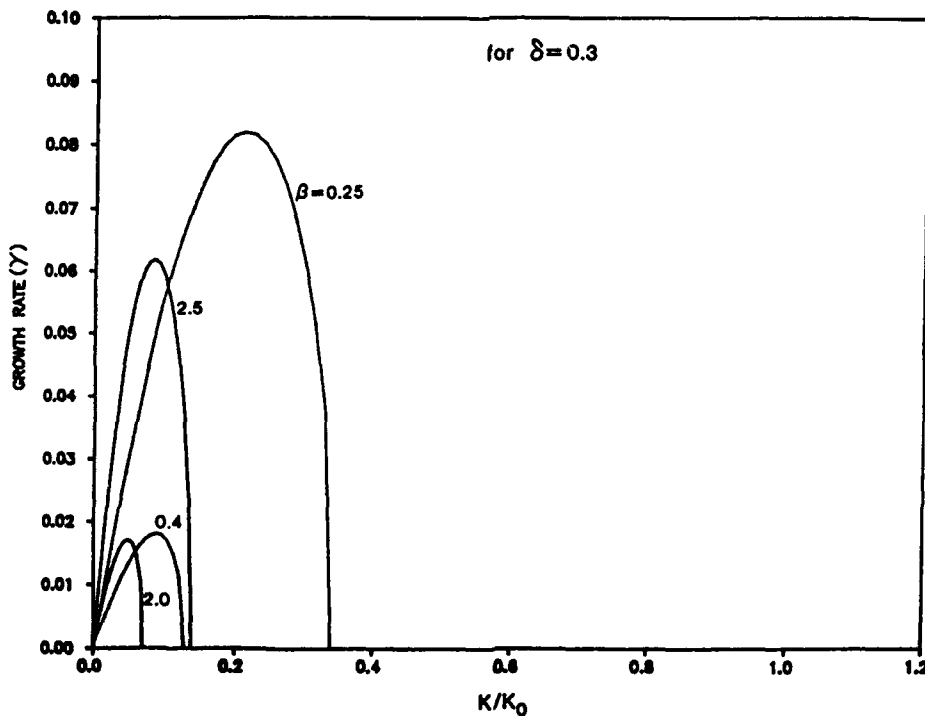
Fig. 8. γ versus (k/k_0) for $\delta=0.03$.

Fig. 9. γ versus (k/k_0) for $\delta=0.06$.

discrepancy may arise from the intrinsic difficulty in the in situ measurements of upstream waves by satellites. Since the speed of solar wind is far greater than those of satellites, all measured waves appear to be nearly parallel propagating. The predicted oblique propagation of magnetosonic waves excited by filamentation instability awaits the corroboration of future observations.

4. Summary and Conclusions

The excitation of a parametric instability by magnetosonic waves in the solar wind environment is proposed. The magnetosonic pump wave originally propagates at the right angle with the magnetic field. This instability can excite a purely growing mode along

Fig. 10. γ versus (k/k_0) for $\delta=0.3$.

the magnetic field together with two symmetric magnetosonic sidebands propagating obliquely across the magnetic field. These two sideband modes thus propagate together perpendicularly across the magnetic field and, meanwhile, form a standing wave pattern along the magnetic field. The physical process responsible for the instability can be described as the scattering of the magnetosonic pump wave into obliquely propagating sidebands by the simultaneously excited plasma density fluctuations, which are associated with a purely growing mode. This instability leads to the filamentation of the magnetosonic pump wave. The thresholds of this filamentation instability can, indeed, be exceeded in the solar wind environment. The density fluctuations produced by the filamentation instability along the magnetic field are predicted to have wavelengths greater than, at least, a few Earth radii. As shown in (18), the polarization of the obliquely propagating magnetosonic waves excited by the filamentation instability is determined by the environmental characteristic parameters: $\delta (= \omega_0 / \Omega_i)$, $\beta (-c_s^2 / v_A^2)$, and k_0 . The predicted oblique propagation of magnetosonic waves, however, has not been confirmed by the available observations yet.

Acknowledgements. This work was supported by the Air Force Office of Scientific Research, grants AFOSR-88-0127 and AFOSR-85-0316, at Polytechnic University; the work was supported by NASA grant NAGS-1055 at the Massachusetts Institute of Technology. The numerical work was performed by M. H. Whang with the Pittsburgh Supercomputing Facility of NSF. The two referees' constructive comments are appreciated.

The Editor thanks S. R. Spangler and another referee for their assistance in evaluating this paper.

References

Abraham-Shranner, B., and W. C. Feldman, Nonlinear Alfvén waves in high-speed solar wind streams, *J. Geophys. Res.*, **82**, 618, 1977.

Derby, N. F., Modulational instability of finite amplitude circularly polarized Alfvén waves, *Astrophys. J.*, **224**, 1013, 1978.

Goldstein, M. L., An instability of finite amplitude circularly polarized Alfvén waves, *Astrophys. J.*, **219**, 700, 1978.

Goldstein, M. L., H. K. Wong, A. F. Vinas, and C. W. Smith, Large-amplitude MHD waves upstream of Jovian bow shock: Reinterpretation, *J. Geophys. Res.*, **90**, 302, 1985.

Hada, T., C. F. Kennel, and B. Buti, Stationary nonlinear Alfvén waves and solitons, *J. Geophys. Res.*, **94**, 65, 1989.

Hoppe, M. M. and C. T. Russell, Plasma rest frame frequencies and polarizations of the low-frequency upstream waves: ISEE 1 and 2 observations, *J. Geophys. Res.*, **88**, 2020, 1983.

Kuo, S. P., M. H. Whang, and M. C. Lee, Filamentation of large-amplitude Alfvén waves, *J. Geophys. Res.*, **93**, 9621, 1988.

Kuo, S.P., M. H. Whang, and G. Schmidt, Convective filamentation instability of circularly polarized Alfvén waves, *Phys. Fluids B*, **32**, 734, 1989.

Lashmore-Davies, C.N., Modulation instability of a finite amplitude alfvén wave, *Phys. Fluids*, **19**, 587, 1976.

Longtin, M., and B.U.O. Sonnerup, Modulational instability of circularly polarized Alfvén waves, *J. Geophys. Res.*, **91**, 6816, 1986.

Mjøehus, E., On the modulation instability of hydromagnetic waves parallel to the magnetic field, *J. Plasma Phys.*, **16**, 321, 1976.

Ovenden, C. R., H. A. Shah, and S. J. Schwartz, Alfvén solitons in the solar wind, *J. Geophys. Res.*, **88**, 6095, 1983.

Spangler, S. R., Nonlinear astrophysical Alfvén waves: Onset and outcome of the modulational instability, *Astrophys. J.*, **299**, 122, 1985.

Spangler, S. R., The evolution of nonlinear Alfvén waves subject to growth and damping, *Phys. Fluids*, **29**, 2535, 1986.

Terasawa, T., M. Hoshino, J. I. Sakai, and T. Hada, Decay instability of finite-amplitude circularly polarized Alfvén waves: A numerical simulation of stimulated Brillouin scattering, *J. Geophys. Res.*, **91**, 4171, 1986.

Vinas, A. F., M. L. Goldstein, and M. H. Acuna, Spectral analysis of magnetohydrodynamic fluctuations near interplanetary shocks, *J. Geophys. Res.*, **89**, 6813, 1984.

Wong, H. K. and M. L. Goldstein, Parametric instabilities of circularly polarized Alfvén waves including dispersion, *J. Geophys. Res.*, **91**, 5617, 1986.

S.P. Kuo, Weber Research Institute, Polytechnic University, Farmingdale, NY 11735.

M.C. Lee, Massachusetts Institute of Technology, Cambridge, MA 02139.

(Received December 5, 1988;
revised April 5, 1989;
accepted May 17, 1989.)

Bragg scattering of electromagnetic waves by microwave-produced plasma layers

S. P. Kuo and Y. S. Zhang

Weber Research Institute, Polytechnic University, Route 110, Farmingdale, New York 11735

(Received 18 July 1989; accepted 26 October 1989)

A set of parallel plasma layers is generated by two intersecting microwave pulses in a chamber containing dry air at a pressure comparable to the upper atmosphere. The dependencies of breakdown conditions on the pressure and pulse length are examined. The results are shown to be consistent with the appearance of tail erosion of the microwave pulse caused by air breakdown. A Bragg scattering experiment, using the plasma layers as a Bragg reflector, is then performed. Both time domain and frequency domain measurements of wave scattering are conducted. The experimental results are found to agree very well with the theory.

I. INTRODUCTION

Over the years there has been considerable effort concentrated on investigating the propagation of high-power microwave pulses through the air. Ionization enhances the electron density in the plasma trail following the pulse and in turn, radically modifies wave propagation.¹⁻⁶ However, the possibility of generating plasma layers by high-power radio waves in the atmosphere at heights of 30–60 km was first studied theoretically by Gurevich and his co-workers.⁷⁻¹⁰ An artificial atmospheric plasma is thought to be capable of reflecting radio waves and extends the capability of ionospheric radio communications. In general, there are two processes that can be used for the reflection of radio waves. One process is through the cutoff reflection for which the frequency of the incident wave has to be lower than the maximum effective plasma frequency. Therefore the maximum frequency of a radio wave reflecting from the plasma is determined by the electron density of the plasma and the collision frequency between electrons and neutrals. On the other hand, if the plasma is structured with layers, it is believed that Bragg scattering would be an effective process for reflecting radio waves off the plasma layers. In this case, there is no upper bound in the frequency of reflection; however, the Bragg condition determines the region of frequency of radio waves for achieving the maximum reflection. One of the apparent advantages of the Bragg scattering process is that much less dense plasma than that required for the cutoff reflection process can be used for reflecting waves of the same frequencies. This implies that much less power is needed for plasma generation and its sustainment if the Bragg scattering process is adopted. Although the use of the Bragg scattering process requires the scattering plasma to be structured, it may well be the inherent property of the plasma depending on the scheme of plasma generation.

It turns out that the most promising method of plasma generation by electromagnetic radiation is to strike a discharge in the intersection region of parallel polarized wave beams.¹¹ The interference between the fields of the two beams (for example) enhances the peak field amplitude and thus reduces the required power level of each γf beam. This, in turn, helps to reduce the propagation loss in pulse energy before the two beams intersect. In fact, more energy will be

delivered to the destination because the pulse tail erosion problem can be almost completely suppressed, especially when the intersection altitude is chosen to be near 50 km (1 Torr pressure) where the breakdown threshold (for γf pulses in the GHz frequency range) is minimum (so that the most effective ionization can be achieved). In the intersection region, the field amplitude varies periodically in space in the direction perpendicular to the plane bisecting the two beams. Consequently, the induced ionization patch consists of a set of parallel plasma layers, as an ideal set up for Bragg scattering purposes.

In this paper, we report some laboratory experiments on the characteristic features of air breakdown produced by two microwave beams intersecting at right angles to each other and Bragg scattering of test waves off the induced plasma layers. The organization of this paper is as follows. The experimental setup is described in Sec. II, in which the experimental results characterizing the dynamics and structure of induced plasma are also given. In Sec. III the Bragg scattering experiment is reported. Both time domain and frequency domain measurements of scattering signals are performed. The experimental results are compared with the theory. The work is summarized and discussed in Sec. IV.

II. CHARACTERISTICS OF AIR BREAKDOWN BY MICROWAVE PULSES

Chamber experiments to study the Bragg scattering off microwave-generated plasma layers are conducted. The chamber is a 2 ft Plexiglas cube that is filled with dry air to a pressure corresponding to the simulated altitude. The microwave power is generated by a single magnetron tube (OKH 1448) driven by a soft tube modulator. The magnetron delivers 1 MW peak output power at a center frequency of 3.3 GHz. The modulator uses a pulse forming network having a pulse width that can be varied from 1.1 to 3.3 μ sec, with respective repetition rates from 60 to 20 Hz. The microwave beams are fed into the cube, with parallel polarization direction, by two S-band microwave horns placed at right angles to the adjacent sides. The plasma layers are then generated in the central region of the chamber where the two beams intersect. Shown in Fig. 1 is a photo of the plasma layers that are manifested by the enhancement of the airglow

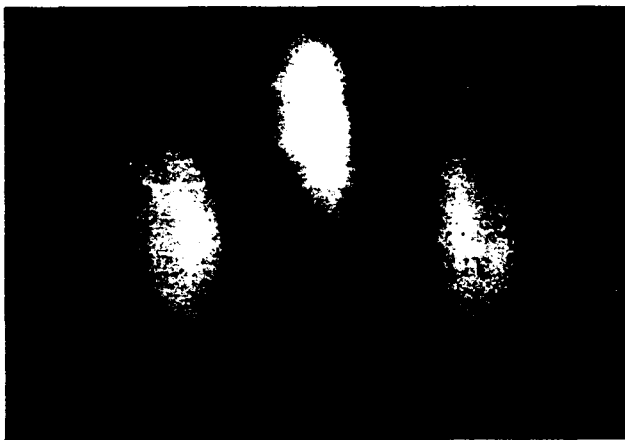


FIG. 1. A top view of plasma layers produced in the chamber

from the corresponding locations. A maximum of eight layers can be generated, though only a few of them are shown in the photo. Shown in Fig. 2(a) is the typical envelope of a 1.1 μ sec pulse used for plasma generation. Using a focusing lens to localize the enhanced airglow, its temporal evolution between the two consecutive pulses is then recorded on the oscilloscope through a photomultiplier tube. A typical result is shown in Fig. 2(b), which shows the growth and decay of the enhanced ionization. We have also measured the breakdown threshold field as a function of the pressure. The microwave field is measured by a microwave probe that has been calibrated by a known waveguide field. The breakdown

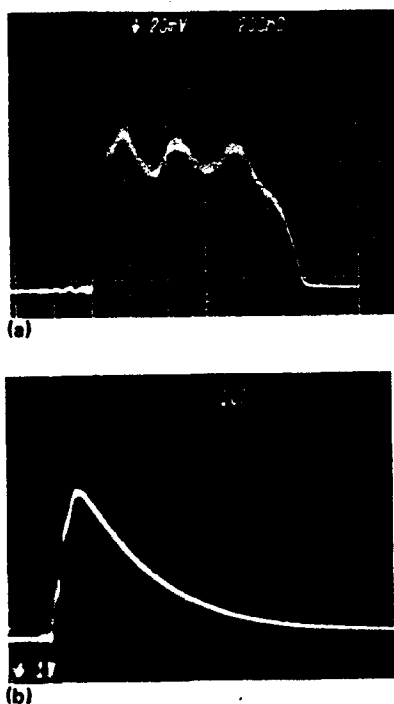


FIG. 2. The optical measurement of the growth and decay of the airglow from a plasma generated by two intersecting 1.1 μ sec microwave pulses. (a) Envelope of a 1.1 μ sec microwave pulse; the horizontal axis is 200 nsec/division. (b) Growth and decay of plasma glow measured by an optical probe, 1 μ sec/division.

threshold is defined as the wave field that is able to enhance minimum observable airglow monitored by the photomultiplier tube. Shown in Fig. 3 are the Paschen breakdown curves for the cases of 1.1 and 3.3 μ sec pulses. Since a shorter pulse requires a larger ionization rate in order to generate the same amount of electrons (which are proportional to the enhanced airglow flux), the threshold field is, therefore, accordingly increased. This tendency is clearly demonstrated in Fig. 3. It shows that the breakdown threshold field for a 1.1 μ sec pulse is always larger than that for a 3.3 μ sec pulse. The results also show that in both cases, the breakdown threshold field decreases with a decrease in air pressure and reaches a minimum in the 2 to 1 Torr region, where $\omega \approx \nu_c$; ω and ν_c are the microwave frequency and electron-neutral collision frequency, respectively. With a further decrease in the pressure, the breakdown threshold field increases again. The increase of the threshold field also occurs because the wave is in the pulse mode. The ionization frequency and collision frequency are proportional to the neutral density; lower pressure requires a larger field in order to maintain the ionization frequency.

The dependence of the breakdown threshold field on the pressure is also manifested by a similar dependence of the degree of attenuation in the tail portion of a single transmitted pulse through the chamber. The experiment is performed by reducing the chamber pressure consecutively from 8 Torr to 50 m Torr, while the incident pulse is fixed at constant amplitude. A series of snapshots demonstrating this behavior is presented in Fig. 4. In the high pressure region (> 8 Torr), the breakdown threshold field is higher than that of the incident pulse and, therefore, very little ionization can occur; thus the pulse can pass through the chamber almost without any distortion [Fig. 4(a)]. However, as the pressure drops, the breakdown threshold also decreases before reaching the minimum, and hence, more ionization occurs and so does more distortion to the pulse [Figs. 4(b)-4(d)]. The distortion always starts from the tail portion of the pulse

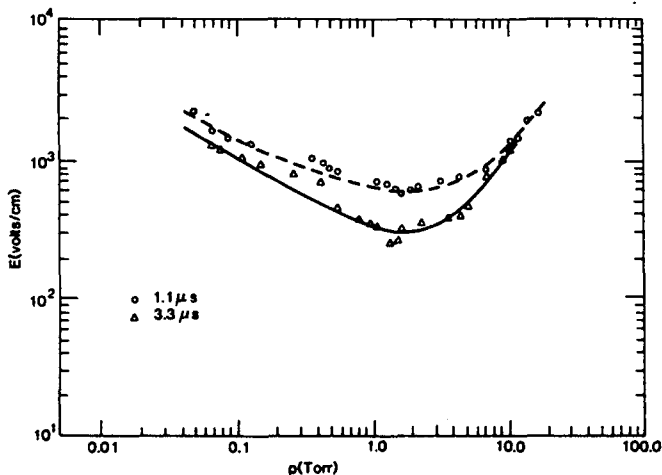


FIG. 3. Dependence of the air breakdown threshold field on the pressure for two pulse lengths.

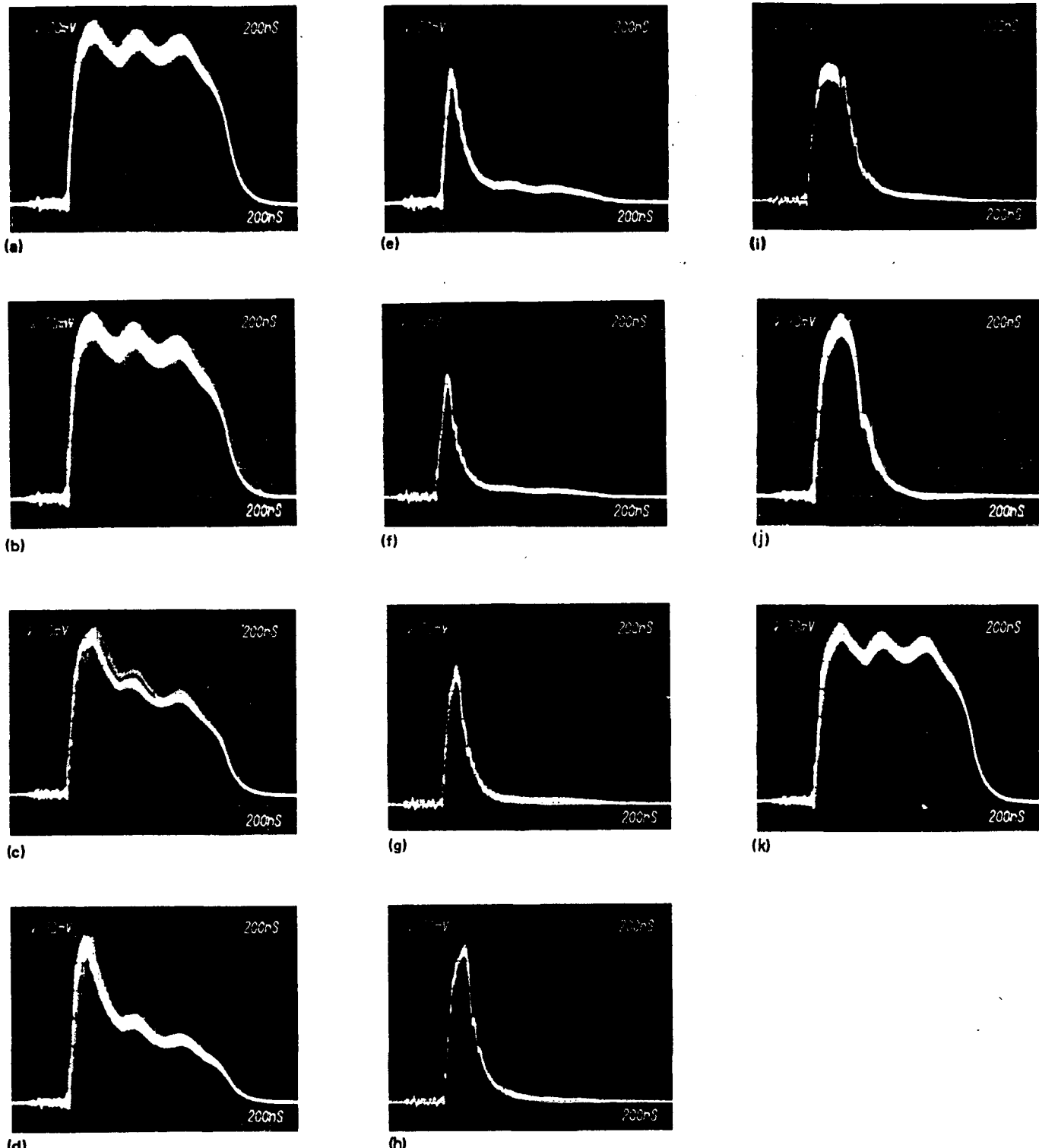


FIG. 4. Pulse received after passing through the chamber at different air pressures, (a) $p = 8$ Torr, (b) $p = 6$ Torr, (c) $p = 5$ Torr, (d) $p = 4$ Torr, (e) $p = 2$ Torr, (f) $p = 1$ Torr, (g) $p = 0.45$ Torr, (h) $p = 0.2$ Torr, (i) $p = 0.1$ Torr, (j) $p = 0.07$ Torr, and (k) $p = 0.05$ Torr.

(i.e., tail erosion) because it takes a finite time for the plasma to build up and thus maximum absorption of pulse energy by the generated electrons always appears in the tail of the pulse. Consequently, the leading edge of the pulse is usually not affected. Between 2 to 1 Torr, the pulse appears to suffer maximum tail erosion and hence only the very narrow lead-

ing edge of the pulse can pass through the chamber [Figs. 4(e) and 4(f)]. The tail erosion becomes weak again for a further decrease in the pressure [Figs. 4(g)-4(j)] and eventually vanishes [Fig. 4(k)] once the pressure becomes so low (<0.05) Torr that the breakdown threshold power exceeds the peak power of the incident pulse.

III. BRAGG SCATTERING

The plasma layers generated by the two crossed microwave pulses are used for the Bragg scattering study. The spatial distribution of the plasma layers is first measured with a Langmuir double probe. This is done by using a microwave phase shifter to move the plasma layers across the probe. The peak density distribution for a spatial period is thus obtained and presented in Fig. 5. The result shows that we have indeed produced very sharp plasma layers with very good spatial periodicity (Fig. 1). A Bragg scattering experiment has then been conducted and described as follows.

Presented in Fig. 6 is a block diagram of the experiment setup. In addition to the facility used for plasma generation (located to the left of the Plexiglas chamber), a sweep microwave generator (4–8 GHz) is used to generate a test wave that is incident into the chamber through a C-band horn. The incident angle of the test wave with respect to the normal of the plasma layers is 45°. Hence the S-band horn #2 located at a right angle to the adjacent side can be used as the receiver of the Bragg scattering test wave. In order to separate the Bragg coherent reflection mechanism from the cut-off reflection mechanism, the test wave is swept in a frequency range much higher than the plasma cutoff frequency. Consequently, the test wave will be received by the S-band horn #1 even while the plasma is present. The amplitude of this undesired signal is reduced by using a directional coupler; nevertheless it represents a large noise to the real scattering signal. To resolve this problem, a standard noise cancellation technique is used. The microwave components used for noise cancellation are shown in the diagram (Fig. 6). An HP spectrum analyzer (8569B) is used for recording the scattering signal. It is noted that the attenuation of the directional coupler is frequency dependent. Only test waves with frequencies leading to more than 15 dB attenuation of the directional coupler are used in the experiment. Conse-

quently, the perturbations of the noise signal as a result of the presence of the plasma, which in principle is in the same intensity level as the scattering signal, is reduced by 15 or more decibels, and will not affect the measurement of the Bragg scattering signal.

Presented in Fig. 7 are the outputs of the spectrum analyzers for two cases. Figure 7(a) shows that no signal is received when there is no plasma. However, an appreciable scattering signal is detected, as shown in Fig. 7(b), whenever plasma layers are produced. The frequency of the test wave is 4.01 GHz, which is much higher than the cutoff frequency. A clear signature of Bragg scattering has been demonstrated. The temporal evolution of the scattering signal has also been measured. The result for a test wave with frequency 5.5 GHz is presented in Fig. 8(a). For comparison, one of the two microwave pulses (both are 1.1 μ sec) used for plasma generation is shown in Fig. 8(b). As we can see, the scattering signal continues to persist for about 100 μ sec after the breakdown pulses are turned off. This result indicates that the coherent scattering process can be very effective even when the plasma frequency is well below (~ 2 order of magnitude) the cutoff frequency of the test wave.

The next question is how the experimental results compare with the theory. Considering a set of N parallel plasma slabs with thickness δ and separation d , and using the Bragg condition $2d \sin \theta = n\lambda_s$, where θ is the angle of Bragg scattering, λ_s is the wavelength of the scattered wave, and n is a positive integer, the scattering (reflection) coefficient S of the wave intensity is derived analytically and expressed as

$$S = |\epsilon_r/\epsilon_s|^2 = (k^2 \alpha/2)^2 [\sin(n\pi\delta/d)/(n\pi/d)^2]^2 \times [\sin N\theta_s/\sin \theta_s]^2, \quad (1)$$

where ϵ_s and ϵ_r are the field amplitudes of the test wave and scattering wave, respectively; $\alpha = \omega_{pe}^2/\omega_s (\omega_s^2 + v_c^2)^{1/2}$; k , and ω_s are the wavenumber and frequency of the test wave; and $\theta_s = (\omega_s - \omega_t)d \sin \theta/c$ and $\omega_s = 2\pi c/\lambda_s$.

This reflection coefficient is then plotted as a function of the test wave frequency in Fig. 9. By sweeping the test wave frequency, such a dependence is also determined experimentally in a relatively small frequency range (4.3–7.8 GHz) and presented in Fig. 9 for comparison. The frequency dependencies of output intensity of the sweep generator and the antenna gain of the receiving horn (S-band horn #2) have been examined and taken into account in calibrating the intensity of the scattering signals. Though a maximum of eight layers can be produced, only three of them have significant overlap along a line of sight. Therefore only these layers can significantly contribute to the Bragg scattering process. Besides an uncalibrated absolute magnitude, the two functional dependencies are shown to agree with each other very well. It is noted that the separation d between the two adjacent plasma layers is related to the wavelength λ_0 of the microwave pulses and the angle ϕ between the propagation directions of the two intersecting pulses with the relationship $d = \lambda_0/2 \sin(\phi/2)$. Using the Bragg condition $2d \sin \theta = n\lambda_s$, the optimum frequency for Bragg scattering is given by

$$f_s = nf_0 \sin(\phi/2)/\sin \theta.$$

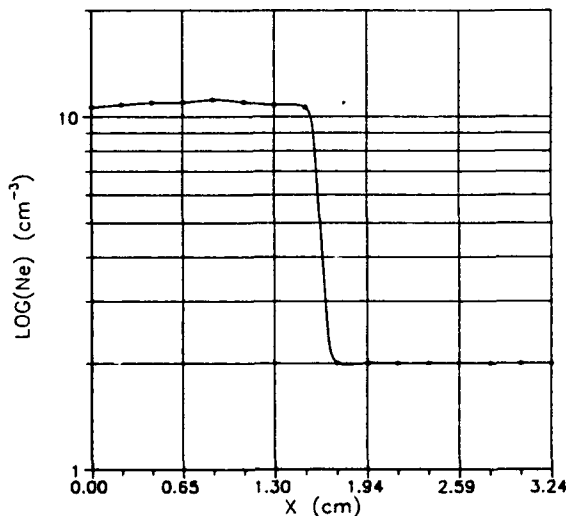


FIG. 5. Probe measurement of the plasma density distribution along the direction transverse to the plasma layers. Measurement is from the central point $x = 0$ of one layer to the midpoint $x = 3.24$ of the next layer. The minimum density 10^2 is an estimated value.

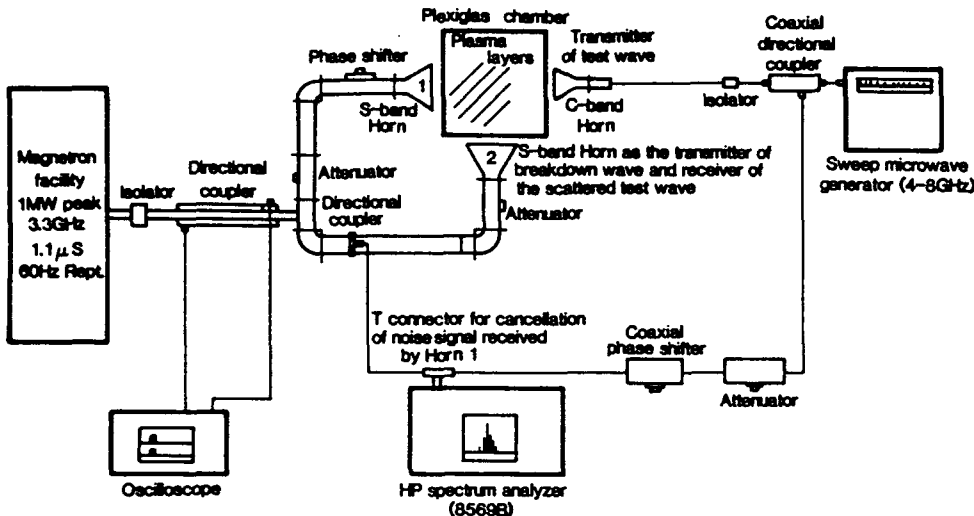
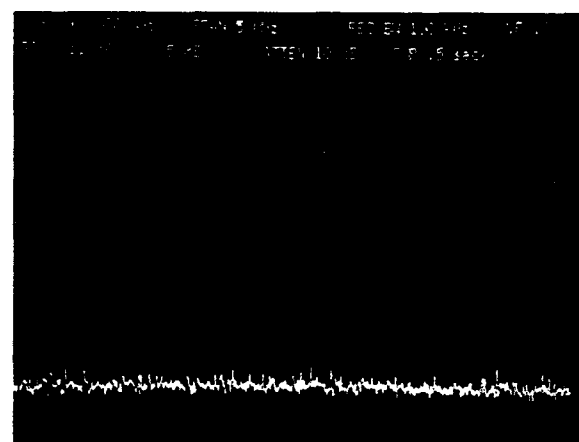


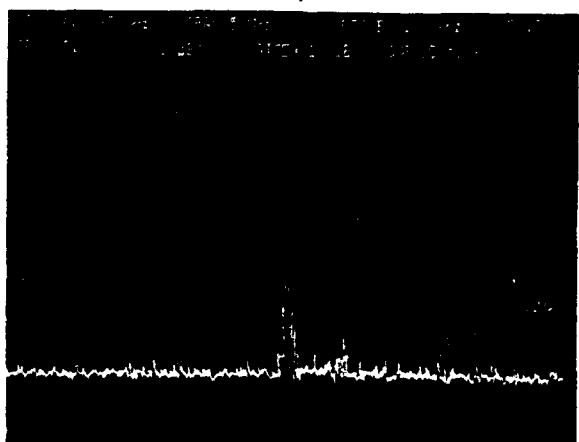
FIG. 6. Microwave Bragg scattering experimental setup.

In the present experiment, $\phi = 90^\circ$ and $\theta = 45^\circ$, and thus $f_s = nf_0$. This indicates that the frequency of the test wave, which satisfies the Bragg condition for the current experimental arrangement, is equal to the frequency and its harmonics of the breakdown pulses. Consequently, the breakdown wave cannot be filtered out and represents a very strong noise, which prevents any meaningful test of Bragg

scattering at these frequencies, and in fact, also in the neighborhood frequency regions. Although the optimum frequency region for Bragg scattering is not examined, nevertheless the consistency between prediction and experimental results may lead us to conclude, based on the maximum theoretical reflection coefficient, that plasma layers can indeed be an



(a)



(b)

FIG. 7. Spectrum analyzer CRT display. (a) No signal is received when the plasma is off. (b) The spectrum of scattering signals when plasma layers are present.



(a)

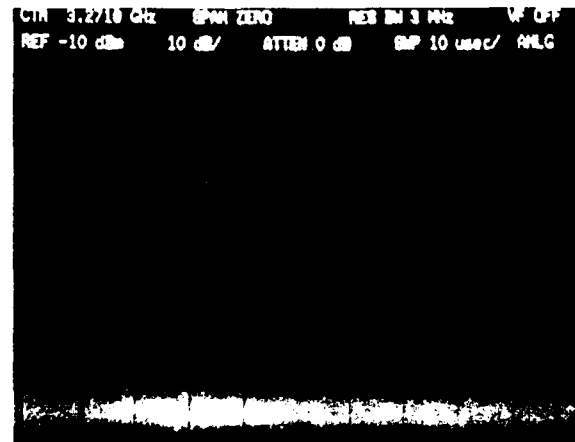


FIG. 8. The time domain measurement of the scattering signal and the microwave pulse used for plasma generation, 10 μ sec/division. (a) Growth and decay of the scattering signal over a 100 μ sec time interval. (b) A 1.1 μ sec pulse similar to that of Fig. 2(a).

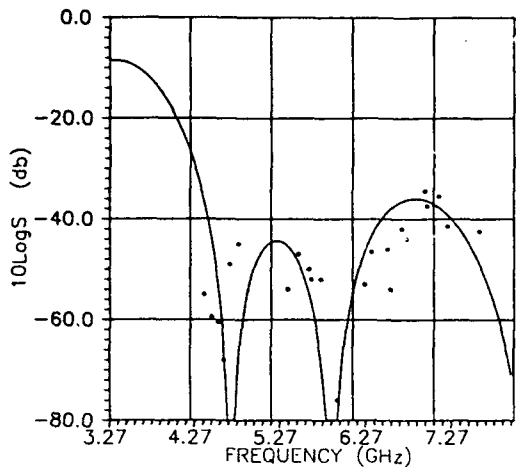


FIG. 9. The dependence of the reflectivity S of plasma layers on wave frequency. Experimental and theoretical results. The 0 dB on the vertical axis is an arbitrary reference.

effective Bragg reflector, especially if more layers can be produced for scattering purposes.

IV. SUMMARY AND DISCUSSION

Plasma layers generated by two intersecting microwave pulses are used for the study of Bragg scattering. The experiment is conducted in a large Plexiglas chamber shielded with a microwave absorber so that the microwave reflection from the wall can be minimized. Hence the experiment can be considered to be a laboratory simulation of conceptualized plasma layers generated by high-power radio waves in the upper atmosphere, as investigated theoretically by Gurevich.

We first determine the characteristics of air breakdown by powerful microwave pulses. We have observed that it is very difficult to generate plasma in the center of the chamber with a single pulse. This is mainly because the plasma generated near the wall adjacent to the microwave horn causes erosion of the tail of the incident pulse and the pulse becomes too short, by the time it reaches the central region of the chamber, to cause appreciable ionization. However, this problem is easily overcome when the scheme of two intersecting pulses is used for plasma generation. In this approach, each pulse has its field amplitude below the breakdown threshold to avoid the tail erosion. However, the fields in the intersecting region can add up and exceed the breakdown threshold. This scheme is most effective when the two pulses have the same polarization and are coherent. In this case, the wave fields form a standing wave pattern in the intersecting region in the direction perpendicular to the bisecting line of the angle ϕ between the intersecting pulses. Thus parallel plasma layers with a separation $d = \lambda_0/2 \sin(\phi/2)$ can be generated. This result is shown in Fig. 1.

Since there are no electrodes involved in the current experiment of air breakdown, we can determine the breakdown threshold field as a function of the air pressure within the accuracy of microwave probe measurement. Two Paschen breakdown curves for the cases of 1.1 and 3.3 μ sec

pulses are determined as shown in Fig. 3. The appearance of a Paschen minimum can be explained as the result of breakdown by a short pulse that is equivalent to a dc discharge with short separation between electrodes (i.e., short electron transit time). The result that the breakdown threshold by a longer pulse (3.3 μ sec) is lower than that by a shorter pulse (1.1 μ sec) agrees with the explanation. The characteristic of the curves is also confirmed phenomenologically by the various degrees of tail erosion of the same pulse passing through the chamber at different pressures, as shown in Fig. 4.

An optical probe has been used to monitor the growth and decay of airglow enhanced by microwave-generated electrons. Two processes are, in general, responsible for the airglow; one is electron-ion recombination and the other is impact excitation of natural gas. Since only weakly ionized plasma is generated, the second process is believed to be dominant. However, the second process requires that the electron energy exceed 2 eV. Therefore the decay rate of airglow intensity shown in Fig. 2(b) accounts for not only the decay of the electron density caused by the dissociative attachment loss but also for the decay of the electron temperature caused by energy loss to the neutrals and the loss of fast electrons.

We then conducted the Bragg scattering experiment with the produced plasma layers. Both temporal evolution of the scattering signal from a test wave and the spectral dependence of the scattering coefficient have been examined. Good agreement between theoretical and experimental results on the spectral dependence of the scattering coefficient has been achieved (Fig. 9). The theoretical result (1) shows that the scattering coefficient is proportional to the square of the electron density and insensitive to the electron temperature. Therefore the electron decay rate after the breakdown pulses have passed through can be evaluated from Fig. 8(a). The figure shows that the initial decay rate is about $6 \times 10^4 \text{ sec}^{-1}$, which is consistent with the dissociative attachment rate. It also shows that the electron density after 70 μ sec is reduced by a factor of about 30. Similarly, the electron decay rate is also reduced over a factor of 10 from the initial decay rate. In this region the decay rate is consistent with the recombination loss rate. This is realized by the fact that when enough negative molecule ions are produced through the electron attachment process, the detachment rate for electron regeneration is increased and eventually balances out the electron attachment loss rate. Thus the dominant electron loss mechanism is shifted to the recombination process. It should be noted that the attachment process causes only the decay of free electrons. The ion density decays at a relatively slow rate determined by the recombination process and the ambipolar diffusion process.

ACKNOWLEDGMENTS

We wish to acknowledge useful discussions with Professor N. Marcuvitz of the Polytechnic University, with Dr. Paul Kossey of the Air Force Geophysics Laboratory, and with Dr. M. C. Lee of the Massachusetts Institute of Technology and helpful technical assistance from K. K. Tiong.

This work was supported by the Air Force Geophysics Laboratory through a NASA Grant No. NAG5-1051 and by the Air Force Office of Scientific Research, Air Force Systems Command, Grant No. AFOSR-85-0316.

¹A. D. MacDonald, D. U. Gaskell, and H. N. Gitterman, Phys. Rev. **5**, 1841 (1963).

²W. M. Bollen, C. L. Yee, A. W. Ali, M. J. Nagurney, and M. E. Read, J. Appl. Phys. **54**, 101 (1983); C. L. Yee, A. W. Ali, and W. M. Bollen, *ibid.* **54**, 1278 (1983).

³J. H. Yee, R. A. Alvarez, D. J. Mayhall, N. K. Madsen, and H. S. Ca-

bayan, J. Radiation Effects Res. Eng. **3**, 152 (1984).
⁴B. Goldstein and C. Longmire, J. Radiation Effects Res. Eng. **3**, 1626 (1984).
⁵W. Woo and J. S. DeGroot, Phys. Fluids **27**, 475 (1984).
⁶J. H. Yee, R. A. Alvarez, D. J. Mayhall, D. P. Byrne, and J. DeGroot, Phys. Fluids **29**, 1238 (1986).
⁷A. V. Gurevich, Geomagn. Aeron. **12**, 631 (1972).
⁸A. V. Gurevich, Geomagn. Aeron. **19**, 428 (1979).
⁹N. D. Borisov and A. V. Gurevich, Geomagn. Aeron. **20**, 841 (1980).
¹⁰A. V. Gurevich, Sov. Phys. Usp. **23**, 862 (1981).
¹¹A. L. Vikharev, V. B. Gil'denburg, O. A. Ivanov, and A. N. Stepanov, Sov. J. Plasma Phys. **10**, 96 (1984); A. L. Vikharev, O. A. Ivanov, and A. N. Stepanov, *ibid.* **10**, 460 (1985).

Propagation of high-power microwave pulses in air breakdown environment

S. P. Kuo and Y. S. Zhang

Department of Electrical Engineering and Computer Science, Polytechnic University, Farmingdale,
New York 11735

Paul Kossey

Air Force Geophysics Laboratory, Hanscom Air Force Base, Massachusetts 01731

(Received 28 August 1989; accepted for publication 29 November 1989)

A chamber experiment is conducted to study the propagation of high-power microwave pulses through the air. Two mechanisms responsible for two different degrees of tail erosion have been identified experimentally. The optimum pulse amplitude for maximum energy transfer through the air has also been determined.

I. INTRODUCTION

The propagation of high-power microwave pulses through the atmosphere has been a subject with considerable scientific interest.¹⁻⁵ This is because air breakdown produces ionization phenomena that can radically modify wave propagation. Ionization gives rise to a space-time-dependent plasma which attenuates the tail of the pulse but hardly affects the leading edge because of the finite time for the plasma to build up. A mechanism which is called "tail erosion" plays the primary role in limiting transmission of the pulse.¹⁻³ Moreover, the nonlinear and nonlocal effects brought about by the space-time-dependent plasma also play important roles in determining the propagation characteristic of the pulses.⁵ Therefore, any meaningful theoretical effort requires a self-consistent description of the propagation process. Consequently, an experimental effort could be more relevant and useful.

Basically, there are two fundamental issues to be addressed. One concerns the optimum pulse characteristics for maximum energy transfer through the atmosphere by the pulse. The second concern is maximizing the ionizations in the plasma trail following the pulse. In general, these two concerns are interrelated and must be considered together. This is because in order to minimize the energy loss in the pulse before reaching the destination, one has to prevent the occurrence of excessive ionization in the background air. Otherwise, the overdense plasma can cutoff the propagation of the remaining part of the pulse and cause the tail of the pulse to be eroded via the reflection process. This process is believed to be far more severe in causing tail erosion than the normal process attributed to ionization and heating. Once this process occurs, the remaining pulse will become too narrow to ionize dense enough plasma whose nonlinear effect is thought to help in sufficient focusing to compensate for wave spreading beyond the Fresnel distance.

The purpose of our experimental effort is to understand the fundamental behavior of tail erosion and address the question of how energy loss depends on basic parameters such as pulse intensity and width, and background pressure. The experimental data can then be incorporated for the development of a useful theoretical model for a self-consistent derivation of pulse propagation.

II. TAIL EROSION MECHANISMS

Experiments have been conducted in a large chamber made of a 2-ft cube of plexiglass and filled with dry air at various pressures. A microwave pulse is fed into the cube by an S-band microwave horn placed at one side of the chamber. A second S-band horn placed at the opposite side of the chamber is used to receive the transmitted pulse. The chamber is shielded with microwave absorbers so that the microwave reflection from the walls and nearby structures can be minimized. The microwave power is generated by a single magnetron tube (OKH 1448) driven by a soft-tube modulator. The magnetron produces 1 MW peak output power at a frequency of 3.27 GHz. The modulator uses a pulse-forming network (PFN) having a pulse width of 1.1 μ s and a repetition rate of 60 Hz. The PFN can also be adjusted to increase the pulse width to 3.3 μ s, while reducing the repetition rate to 20 Hz. Figure 1 shows the block diagram of the experimental setup.

Breakdown of air was detected either visually, as the first sign of a glow in the chamber, or as the distortion in the shape of the pulse received by the horn placed at the opposite side of the chamber. The dependence of the breakdown threshold field on the pressure can thus be manifested by a dependence of the degree of distortion of the tail portion of the transmitted pulse through the chamber. A series of snapshots demonstrating this behavior is presented in Fig. 2. In

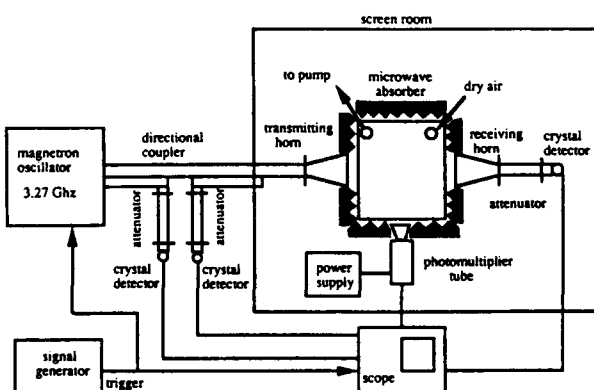
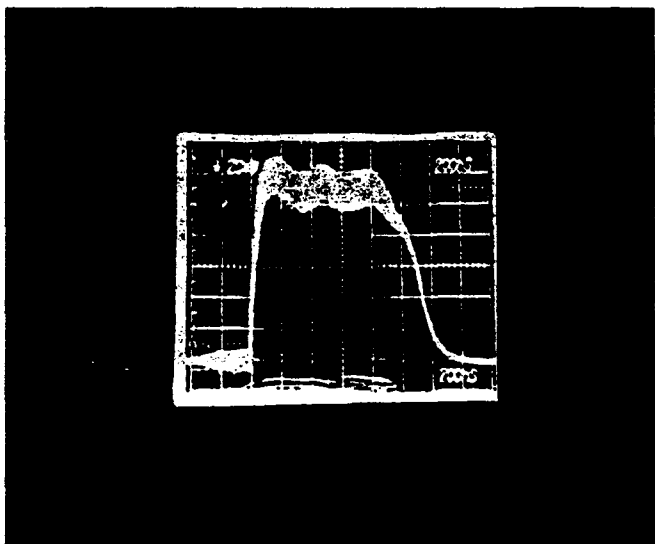
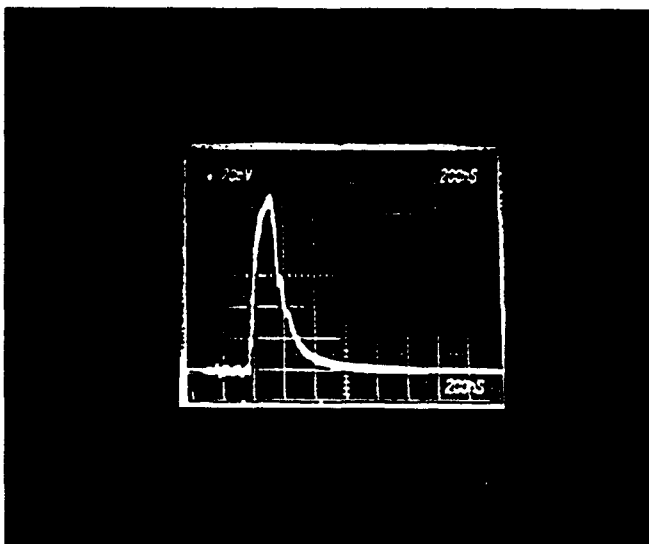


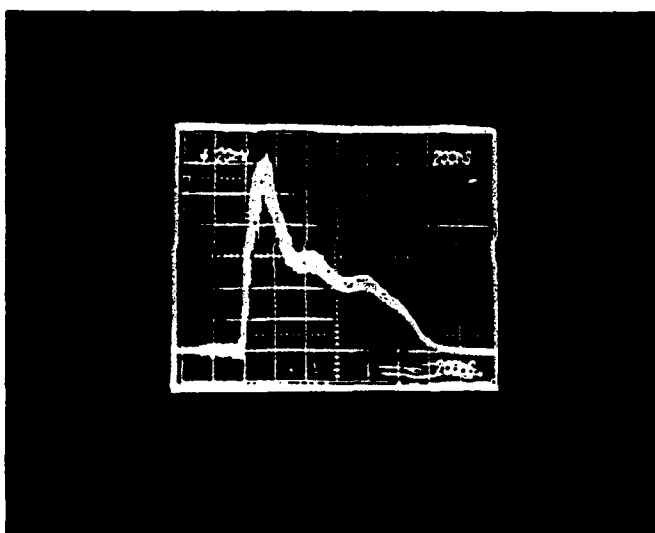
FIG. 1. Experimental setup.



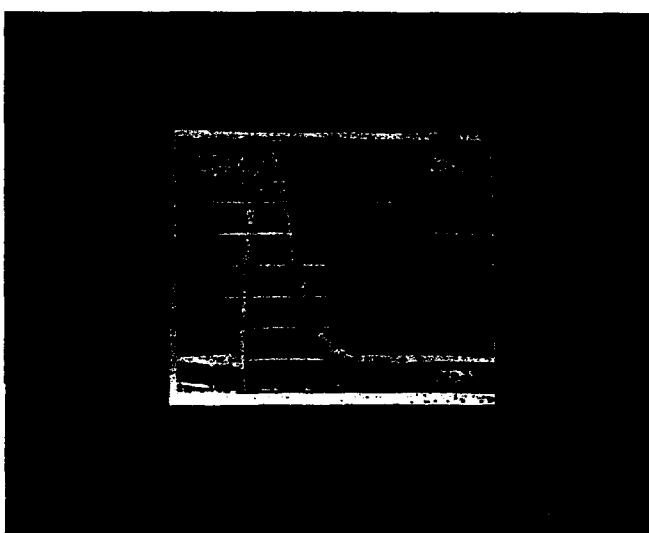
(a)



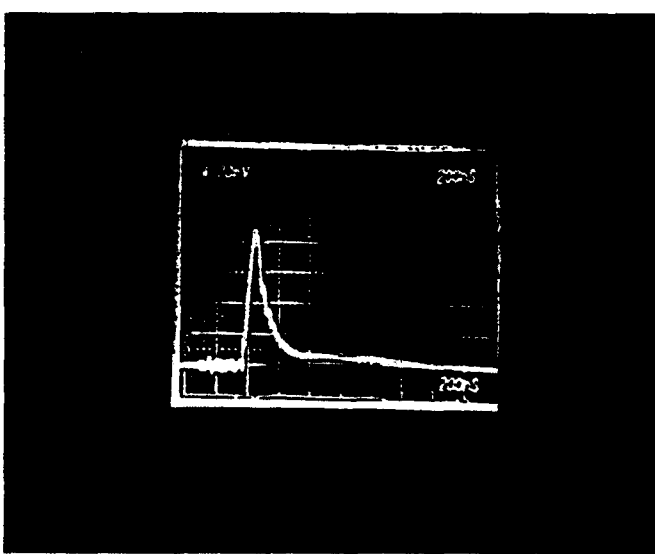
(d)



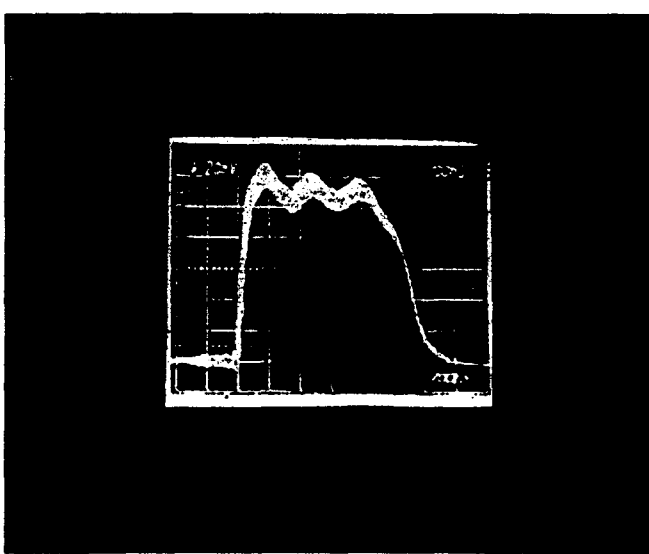
(b)



(e)



(c)



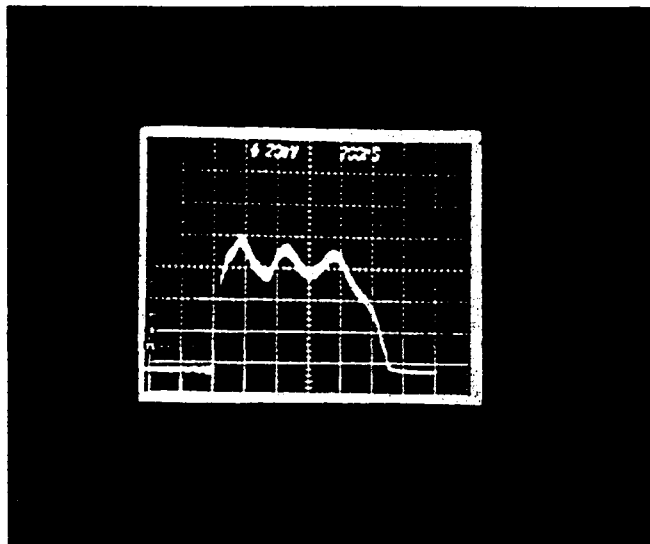
(f)

FIG. 2. Pulses propagating through chamber at different air pressures. (a) $p = 8$, (b) $p = 4$, (c) $p = 1$, (d) $p = 0.2$, (e) $p = 0.07$, and (f) $p = 0.05$ Torr.

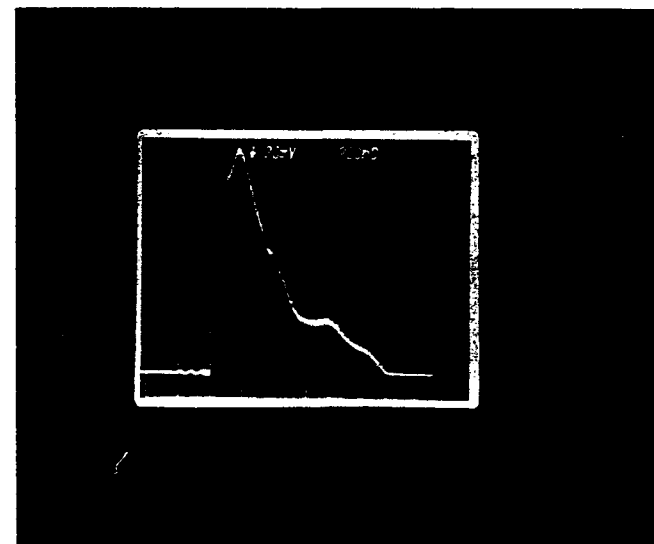
the high-pressure regions pictured, the breakdown threshold is expected to be high and, therefore, very little ionization can occur and the pulse can pass through the chamber almost without any loss (or distortion). However, as the pressure drops, the breakdown threshold also decreases before reaching the minimum, hence, more ionization occurs and also more distortion to the pulse. The distortion always starts from the tail of the pulse (i.e., tail erosion) because it takes finite time for the plasma to build up and, thus, maximum absorption of pulse energy by the generated electrons always appears in the tail of the pulse. Consequently, the leading edge of the pulse is usually not affected. Between 1 and 2 Torr, the pulse appears to suffer maximum tail erosion and hence only very narrow leading edge can pass through the chamber. The tail erosion becomes weak again for a further decrease in the pressure and can eventually be prevented once the pressure becomes so low that the breakdown

threshold power exceeds the peak power of the incident pulse.

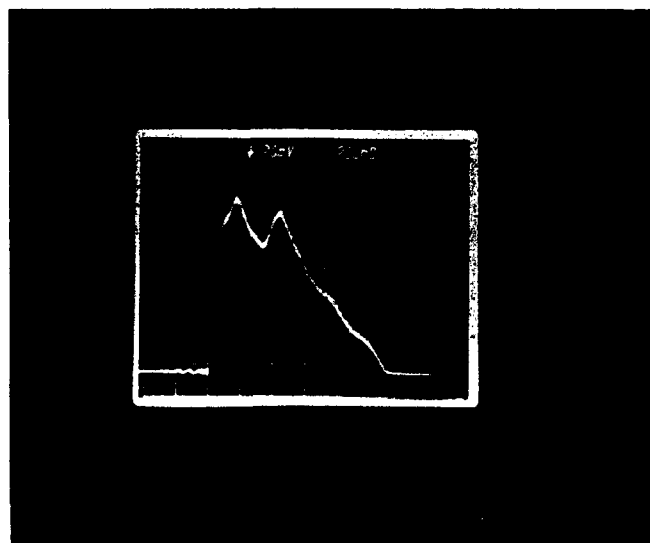
Tail erosion is a common phenomenon appearing in the propagation of a high-power microwave pulse (HMP). This phenomenon is further demonstrated by the snap shots presented in Fig. 3, where $1.1\ \mu\text{s}$ pulses, with four consecutively increasing amplitudes, are transmitted into the chamber of 1 Torr pressure from one side and received at the opposite side. The first pulse has amplitude below the breakdown threshold, and hence, nothing is expected to happen. Consequently, the received pulse shape, as shown in Fig. 3(a), is undistorted from that of transmitted pulse. Once the amplitude exceeds the breakdown threshold, more tail erosion occurred to the larger amplitude pulses, as is observed by the subsequent three snapshots [Figs. 3(b)-3(d)]. This is because the increase of the ionization rate with field amplitude allows more electrons, which attenuate the pulse, to build



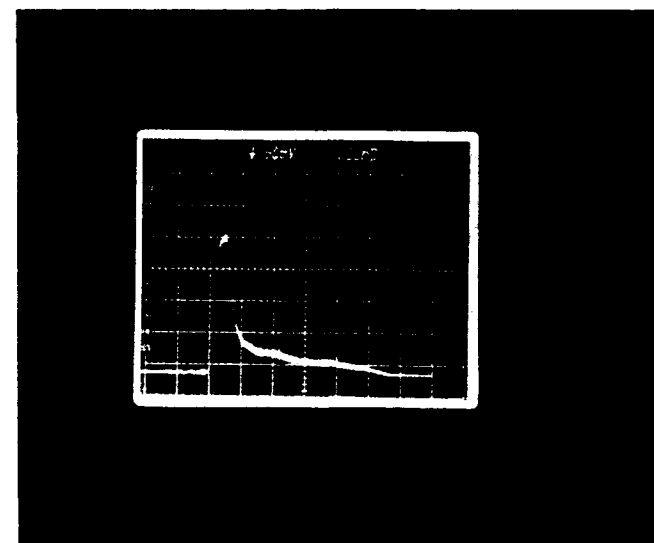
(a)



(c)



(b)



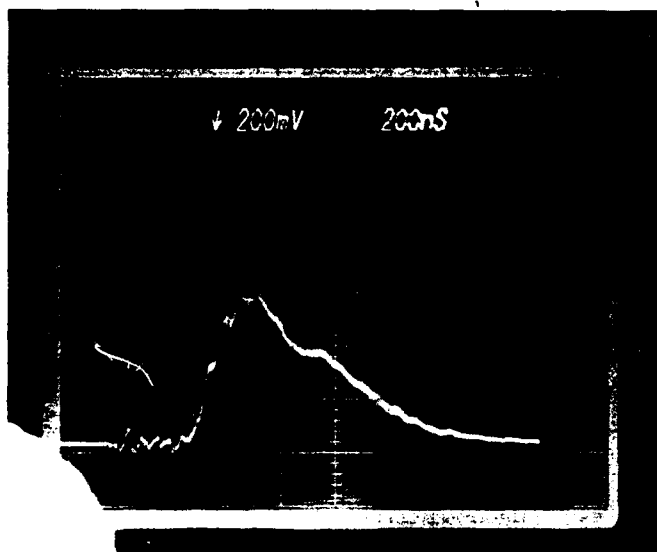
(d)

FIG. 3. Tail erosion of microwave pulses of four consecutively increasing amplitudes A_0-A_4 , after propagating through the chamber with 1 Torr background pressure. (a) Amplitude A_0 , below the breakdown threshold and no erosion. (b) $A_1 = 1.5 A_0$. (c) $A_2 = 2A_0$. (d) $A_3 = 3A_0$.

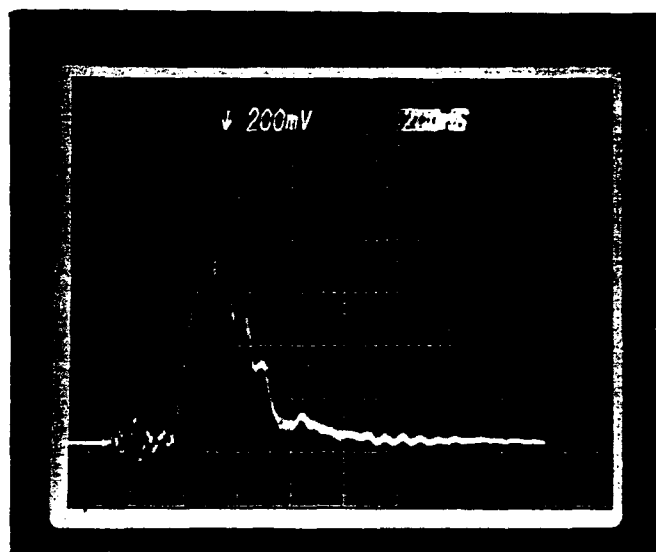
up. Now let us focus on the last two pictures [Figs. 3(c) and 3(d)]. Pulses have been eroded strongly in both cases. However, a clear distinction between the two cases is noticed. In one case corresponding to the third picture [Fig. 3(c)], the erosion to the tail of the pulse is not complete. In other words, the received pulse width extends to the original width. In the other case [Fig. 3(d)], a large portion of the pulse is more or less eroded completely during the finite propagation period. Obviously it is a different mechanism responsible for the second case. The ionization frequency becomes so large in the second case that the electron density exceeds the cutoff density of the wave before the whole pulse passes through. The overdense plasma screen reflects the remaining portion of the pulse and causes even more severe tail erosion. In summary, two mechanisms responsible for the tail erosion are identified. One is due to attenuation by the self-generated underdense plasma. The other one is

caused through reflection by the self-generated overdense plasma screen. These two processes are also verified by the reflected power level measured for each case. As shown in Fig. 4, the snap shots of Figs. 4(b) and 4(d) are the reflected pulse shape corresponding to each received pulse of Figs. 4(a) and 4(c), respectively. As shown by the last set of pictures [Figs. 4(c) and 4(d)], strong reflection and complete erosion are observed consistently.

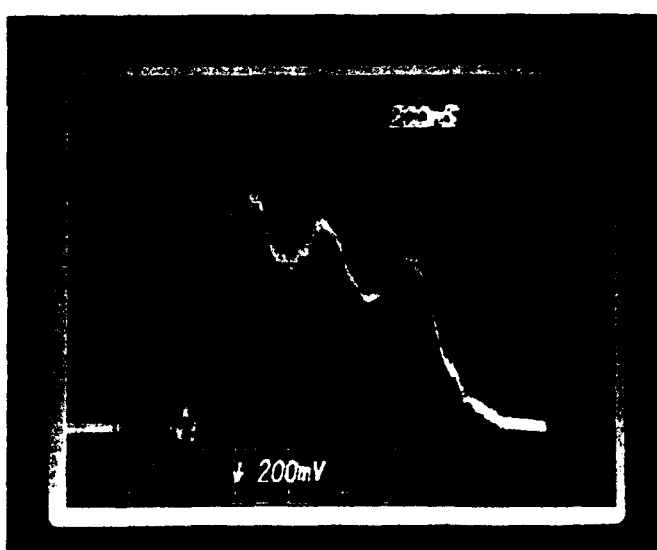
In order to avoid cutoff reflection, the power of the pulse should be lower than a critical power P_c which is defined as the minimum required power for generating an overdense plasma screen. When an overdense plasma screen is formed the shape of the reflected pulse changes drastically and can be monitored easily. Thus, the critical power P_c can be determined. This critical power varies in general with the pressure. Measurements are made to determine this functional dependency as shown in Fig. 5, where $P = P_r/P_c$ is the criti-



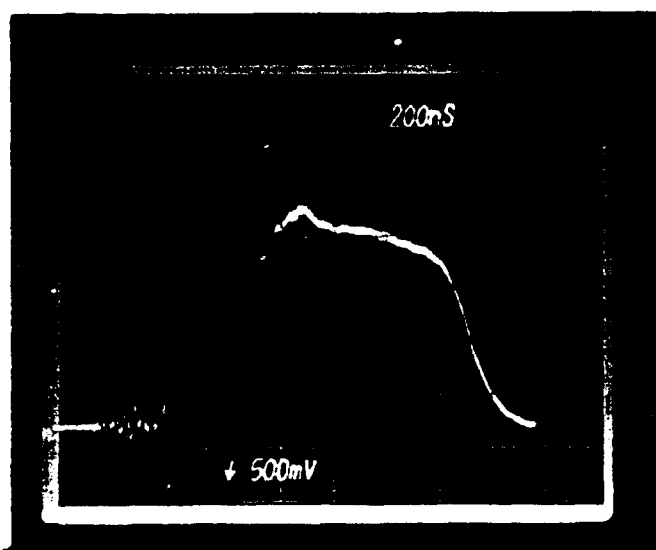
(a)



(c)



(b)



(d)

FIG. 4. Received pulses and the corresponding reflected pulses. (a) Envelope of received pulse. (b) Reflected pulse corresponding to case (a). (c) Received pulse with larger incident amplitude than that of case (a). (d) Reflected pulse corresponding to case (c).

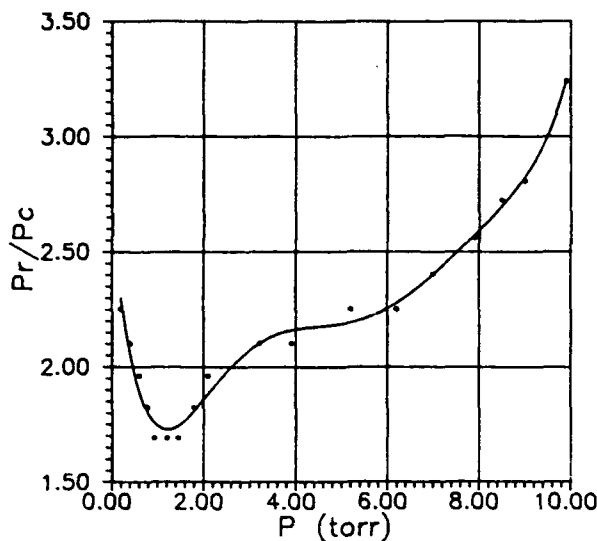
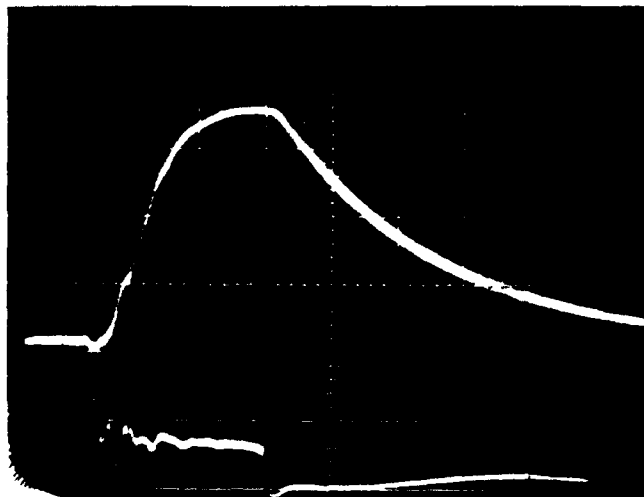


FIG. 5. The dependence of the normalized critical power $P = P_r/P_c$ on pressure for $1.1 \mu\text{s}$ pulse.

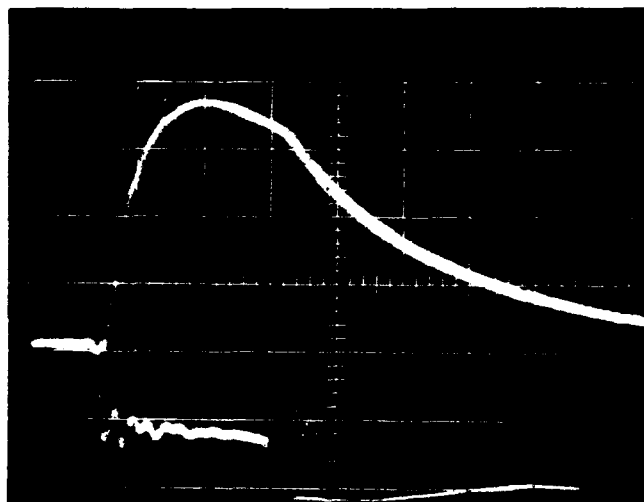
cal power normalized to the breakdown threshold power P_c which has been presented elsewhere.⁶ Due to the limited available microwave power, only the region 0.2–10 Torr is examined. Outside this pressure region, the breakdown threshold power becomes too high to be exceeded by the maximum output power of our microwave source. Nevertheless, this is the pressure region of main concern because air breakdown has its lowest threshold.

III. DISCUSSION

Our study indicates that an increase of pulse amplitude may not help to increase the energy transfer by the pulse. This is because two tail erosion mechanisms are at play to degrade the energy transfer. A demonstration is presented in Fig. 6, where the growth and decay of airglow enhanced by electrons through air breakdown by $3.3 \mu\text{s}$ pulse are recorded for two different power levels. In Fig. 6(a) the power level is below the critical power and the airglow grows for the entire $3.3 \mu\text{s}$ period of the initial pulse width. As power is increased beyond the critical value, the initial growth of the airglow becomes faster as shown in Fig. 6(b). However, it is also shown in Fig. 6(b) that the airglow saturates at about the same level as that of Fig. 6(a). Moreover, the airglow already starts to decay even before the $3.3 \mu\text{s}$ period. In other words, cutoff reflection happening in the second case limits the energy transfer by the pulse. The additional energy added to the pulse is wasted by reflection. The way to solve the problem is either to lower the amplitude of the pulse or to narrow the pulse width so that the propagation loss can be minimized. The remaining question is about the optimum parameters for the pulse in order to achieve effective ionization for a self-focusing purpose. Unfortunately, this question cannot easily be answered by the chamber experiments. This is because the effect of pressure gradient and large propagation distance cannot be incorporated in the investigation. Nevertheless, the understanding of the fundamental behav-



(a)



(b)

FIG. 6. The growth decay of enhanced airglow (upper trace). Pulses of $3.3 \mu\text{s}$ duration and at two different power levels P_1 [for (a)] and P_2 [for (b)] are used for causing air breakdown, where $P_2/P_1 = 1.32$. The lower trace of each photo represents the time dependence of the amplitude of the microwave pulse. The horizontal scales are $1 \mu\text{s}/\text{div}$.

ior of tail erosion and the set of experimental data obtained should be very useful for guiding the development of a practical theoretical model.

ACKNOWLEDGMENTS

This work is being supported by the Air Force Geophysical Laboratory through NASA Grant No. NAG 5-1051 and by the Air Force Office of Scientific Research Grant No. AFOSR-85-0316. Useful discussion with Dr. M. C. Lee is appreciated.

¹W. M. Bollen, C. L. Yee, A. W. Ali, M. J. Nagurney, and M. E. Read, *J. Appl. Phys.* **54**, 101 (1983); C. L. Yee, A. W. Ali, and W. M. Bollen, *ibid.* **54**, 1278 (1983).

²J. H. Yee, R. A. Alvarez, D. J. Mayhall, N. K. Madsen, and H. S. Cabayan, *J. Radiat. Eff. Res. Eng.* **3**, 152 (1984).

³B. Goldstein and C. Longmire, *J. Radiat. Eff. Res. Eng.* **3**, 1626 (1984).

⁴Wee Woo and J. S. DeGroot, *Phys. Fluids* **27**, 475 (1984).

⁵J. H. Yee, R. A. Alvarez, D. J. Mayhall, D. P. Byrne, and J. DeGroot, *Phys. Fluids* **29**, 1238 (1986).

⁶S. P. Kuo and Y. S. Zhang, *Phys. Fluids B* (to be published).

Frequency Up-Conversion of Microwave Pulse in a Rapidly Growing Plasma

S. P. Kuo

Weber Research Institute and Department of Electrical Engineering, Polytechnic University,
Route 110, Farmingdale, New York, 11735
(Received 7 February 1990)

Two crossed microwave pulses are used to generate plasma in their intersection region inside a chamber. It is shown that the frequency of each output pulse is up-shifted. The percentage of frequency shift is consistent with the theory of Wilks, Dawson, and Mori. Besides frequency shift and some attenuation, the similarity between the spectral distributions of the output and input pulses indicates that there is very little distortion to the pulse shape.

PACS numbers: 52.40.Db

Recently, Wilks, Dawson, and Mori¹ have studied an initial-value problem concerning the propagation of an electromagnetic wave through a gas which is ionized in a very short time interval on the order of the period of this wave. The results of their 1D and 2D particle-in-cell computer simulations show that the frequency of the wave is up shifted and confirm their linear theory for the ideal case of instantaneous plasma creation. The physical mechanism of this frequency up-conversion phenomenon becomes quite clear by noting that the wavelength of the wave does not change after the ionization of the gas since the wave does not encounter any spatial variation in the medium; however, the sudden reduction of the index of refraction of the gas by converting it into a plasma forces the wave to propagate with larger phase velocity and, thus, to oscillate with higher frequency at subsequent times.

However, using a single high-power laser pulse for plasma generation and, subsequently, for its frequency up-conversion purpose was shown to be unpractical in the previous experiment by Yablonovitch.² His experiment showed only spectral broadening in the CO₂ laser pulse transmitting through a rapidly growing plasma. We believe that this is because plasma is preferentially generated at the boundary where input pulse and ionized medium first encounter.

In this work, we use two crossed microwave beams with parallel polarization for establishing an initial-value problem. In doing so, we can adjust the intensity of each beam so that a discharge of background gas occurs only in the intersection region of the two beams. The experiment is conducted in a chamber of a 2-ft Plexiglas cube. The carrier frequency of the 1.1-μsec microwave pulses used in the experiment is 3.27 GHz. Shown in Fig. 1(a) is the envelope of each pulse. The chamber is hence more than six wavelengths long and is long enough to shield the boundary effect from the wave over a single wave period. The microwave power is generated by a single magnetron tube (OKH1448) driven by a soft tube modulator having a repetition rate of 60 Hz. The peak output power of the tube is 1 MW. Since we are in-

terested in an initial-value problem, we have to ionize the gas simultaneously over the chamber. However, using a single pulse can only generate a localized plasma near the chamber wall. A second pulse provided by the same magnetron tube is fed into the cube through a second S-band microwave horn placed at a right angle to the first one. With such an arrangement, the power of each pulse can be reduced to below the breakdown threshold of the gas and breakdown of gas can occur only in the central

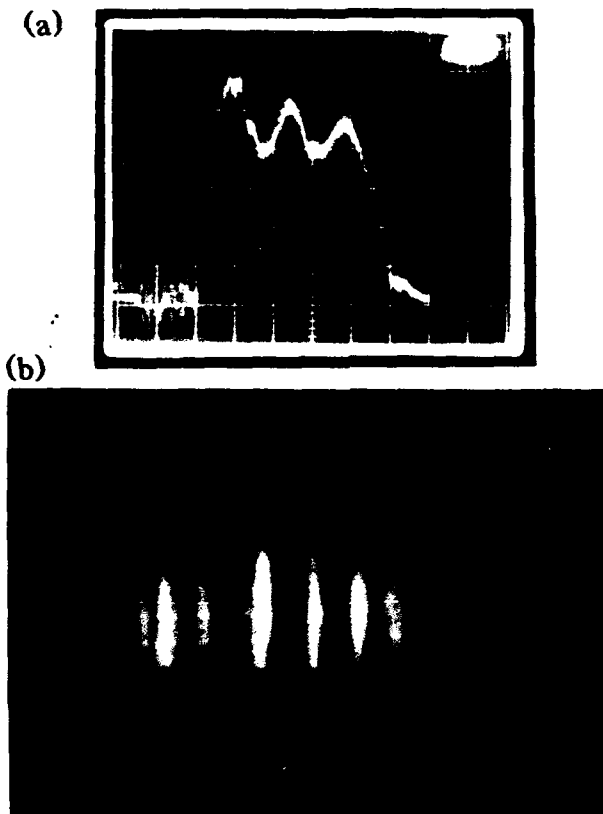


FIG. 1. (a) Envelope of a 1-μsec microwave pulse. (b) A photo of plasma layers generated by two cross pulses having parallel polarization.

region of the chamber where the two pulses intersect. The undesired tail erosion to the pulses by the generated plasma can also be minimized. The wave fields add up to form a standing-wave pattern in the intersecting region in the direction perpendicular to the bisecting line of the angle between the two intersecting pulses. Thus, parallel plasma layers with a separation $d = \lambda_0/\sqrt{2}$ can be generated, where λ_0 is the wavelength of the wave. Two phase shifters are used to extend the region covered by the plasma layers. A maximum of eight layers detected visually can be generated to cover almost the entire path of the first pulse in the chamber.³ A photo of the plasma layers is presented in Fig. 1(b), where only seven layers are clearly shown. A block diagram of the experimental setup is shown in Fig. 2.

Although the produced plasma is not spatially uniform, it extends over several wavelengths and has a temporal growing average density along the path of the first pulse. The periodic spatial variation of plasma density may cause scattering and, hence, additional attenuation to the incident pulse. Nevertheless, it should not affect the observation on frequency up-shift phenomenon. Since our pulse length is about 300 m long, which is much longer than the length 0.6 m of the chamber, one may divide the pulse into 500 segments and each segment of the pulse experiences a frequency shift while it is inside the chamber. Therefore, the maximum frequency shift on the output pulse is just the maximum frequency shift on each segment. Consequently, only a small fraction of total density change over the pulse period can contribute to the frequency shift. In order to enhance frequency shift, one would have to increase the ionization rate. However, this cannot be done by simply increasing the pulse amplitude because gas breakdown can occur locally near the chamber wall, and the nature of initial-value problem is demolished. We find that if we mix dry air with argon gas with total pressure about 2.3 Torr, maximum frequency up-shift is achieved. This is because dry air has a high breakdown threshold which

enables us to increase the pulse amplitude without causing serious tail erosion and argon is helping the initial ionization for the subsequent electron-density growth. Shown in Fig. 3 is the frequency spectra of output pulses with and without plasma generation. The corresponding input spectra were also examined. No noticeable difference between the two input spectra was observed. A 1.5-MHz frequency up-shift is clearly demonstrated in Fig. 3. It is noted that the sweep time of the spectrum analyzer is 50 sec. Thus, each recorded spectrum of Fig. 3 represents an average sampling spectrum of 3000 pulses. If the frequency shift of each pulse is not the same, the recorded spectrum should reveal a mean frequency shift as well as spectral broadening. However, no noticeable spectral broadening appeared in the recorded spectrum (curve 2 of Fig. 3), and no noticeable change in the amount of frequency up-shift over many sweeping periods can be detected either. Besides a frequency shift and an attenuation caused by the plasma generation, the similarity between the spectrum of the two pulses indicates that the distortion to the pulse shape due to the plasma generation is very small.

In the density range of interest ($\leq 10^{11} \text{ cm}^{-3}$), the dominant loss mechanism of free electrons in the dry air is through their attachment with neutral molecules. The maximum attachment rate⁴ v_a of dry air at 2.3 Torr is about $3.22 \times 10^5 \text{ sec}^{-1}$. Hence, breakdown occurs only when the ionization rate v_i is larger than the attachment rate v_a . The relationship between v_i and v_a is shown⁴ to be $v_i/v_a \sim (E/E_c)^{5.3}$ for a long pulse and $1.3 < E/E_c < 3.5$, where E_c is the breakdown threshold field of the dry air and can be expressed⁴ as

$$E_c \approx 28(N_m/2.7 \times 10^{19})(1 + \omega_0^2/v_c^2)^{1/2} \text{ kV/cm},$$

N_m is the number of neutrals per cubic centimeter, and

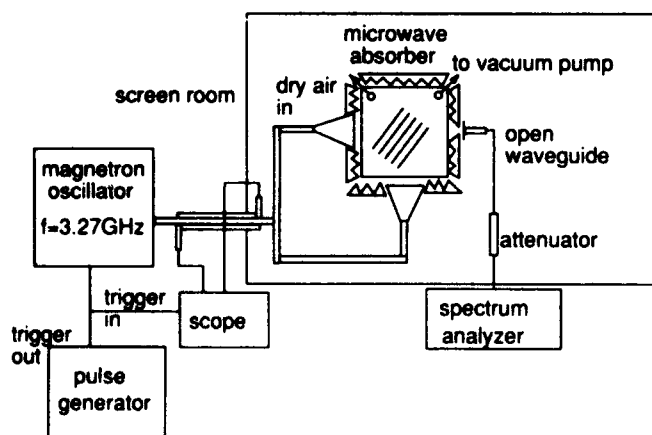


FIG. 2. Experimental configuration.

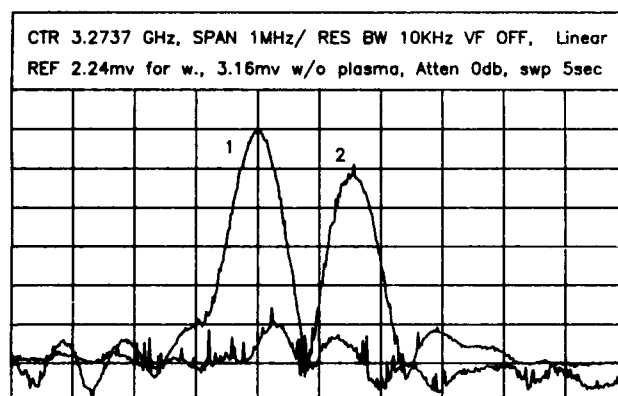


FIG. 3. Frequency spectra of two output pulses with same input. Curve 1 is the spectrum of the pulse passing through the chamber (at the pressure ~ 1 atm) without plasma generation and curve 2 represents the spectrum of the pulse passing through a rapidly growing plasma generated inside the chamber (at the pressure ~ 2.3 Torr).

v_c is the electron-neutral collision frequency. In this experiment, $\omega_0^2/v_c^2 \gg 1$, thus $E_c \sim \omega_0/v_c$. Since v_c is proportional to electron speed and in the present case the electron quiver speed $eE/m\omega_0$ is much larger than the electron thermal speed, then $v_c \sim E$ and this leads to $v_i \sim (E/E_c)^{5.3} \sim E^{10.6}$; a very strong dependence of the ionization frequency v_i on E is shown. It is a disadvantageous feature for controlling the frequency shift by self-generated plasmas. On the other hand, it becomes an advantageous feature for possibly minimizing the spectral broadening on the frequency-shifted output pulse as indicated by the result shown in Fig. 3. The amount of electron-density change contributed to frequency shift of each pulse segment depends not only on the ionization frequency v_i but also on the available time period τ during which the initial effect dominates over the boundary effect, where τ is a time-dependent function. In the beginning of the pulse, the background electron density is low and hence the boundary effect is weak. Thus, the initial effect can prevail over the boundary effect for almost the entire period of the pulse segment; i.e., $\tau_0 = l/c$, the transit time of the pulse through the chamber. τ decreases, however, as the electron density increases. The density change of plasma electrons available for the frequency shift of each pulse segment is then given by $\Delta n_e/n_0 \sim v_i \tau$. Since each segment of the pulse suddenly experiences half of such a fractional electron-density increase on the average, while passing through the chamber, the dispersion relation of the carrier of the pulse should also change accordingly in time from $\omega_p^2 = \omega_{p0}^2 + k\delta c^2$ to

$$\omega_p^2 = (\omega_{p0} + \Delta\omega_p)^2 + k\delta c^2 = \omega_0^2 + 2\omega_{p0}\Delta\omega_p + \Delta\omega_p^2.$$

In the region $\Delta\omega_p \ll \omega_{p0}$, we have

$$\omega_f \approx \omega_0(1 + 2\omega_{p0}\Delta\omega_p/\omega_0^2)^{1/2} \approx \omega_0(1 + \omega_{p0}\Delta\omega_p/\omega_0^2).$$

Since $\Delta\omega_p/\omega_{p0} = \frac{1}{2}(\Delta n_e/n_0) = \frac{1}{2}\Delta n_e/n_0$, we then have the frequency up-shift

$$\Delta f_0/f_0 = \frac{1}{2}(\Delta n_e/n_0)\omega_{p0}^2/\omega_0^2 \sim v_i \tau n_0.$$

In general, this frequency shift is a function of time. It would be the case of a rectangular pulse and lead to a spectral broadening because each pulse segment experiences a slightly different frequency shift. However, no apparently spectral broadening is shown in the result (curve 2) presented in Fig. 3. On the other hand, the pulse envelope shown in Fig. 1(a) is not exactly a rectangular pulse either. It shows that the pulse has a decreasing amplitude (on average). It means that v_i decreases while n_0 increases. It is verified by the Bragg scattering result. Since the generated plasma is a set of parallel layers, one can use the Bragg scattering method³ to monitor the growth and decay of plasma electrons, where the scattering coefficient is proportional to $n_e^2(t)$. As shown in Fig. 4, the intensity of the scattering signal

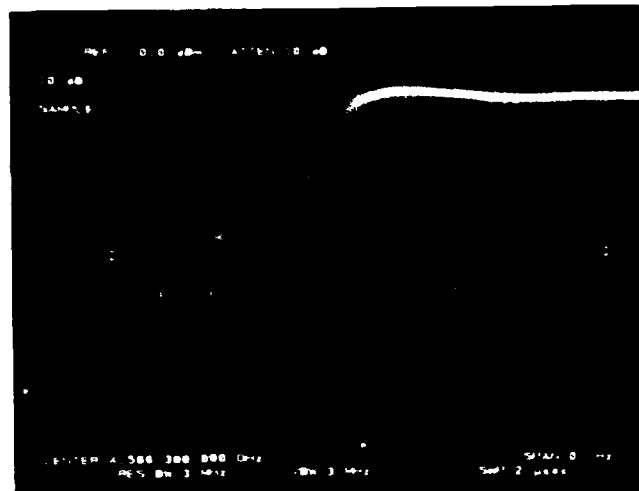


FIG. 4. The growth and decay of the intensity of Bragg scattering signal during the first 2-μsec period.

after emerging out of the noise level increases with a decreasing rate. In order to minimize the spectral broadening on the frequency-shifted output pulse, it requires that $v_i \tau n_0 \sim \text{const}$ over a large portion of pulse length. Considering the portion of the pulse from its peak to the half-peak point (~0.7-μsec interval), a self-consistent set of the solution of the rate equation $dn_0/dt = v_i n_0$ given by $n_0 = n_1(1 + v_{i0}t/1.25)^{1.25}$, $v_i = v_{i0}/(1 + v_{i0}t/1.25)$, and $\tau = \tau_0/(1 + v_{i0}t/1.25)^{0.25}$, with $n_1 = 2.5 \times 10^7 \text{ cm}^{-3}$, $v_{i0} = 2.94 \times 10^9 \text{ sec}^{-1}$, and $\tau_0 = l/c \sim 2 \text{ nsec}$, leads to a constant frequency shift with a value about 1.4 MHz consistent with the experimental result. Using the function $v_i(t)$ and the relation $v_i \sim E^{10.6}$, the envelope of a 0.7-μsec pulse can be reconstructed and is found to overlap closely with the original pulse envelope in the corresponding interval [Fig. 1(a) with average amplitude]. This explains why there is no apparently spectral broadening appearing in curve 2 of Fig. 3. It is noted that at the end of the pulse, the average plasma density is about the cutoff density of each input pulse, i.e., $\langle \omega_p^2 \rangle \approx \omega_0^2 - \frac{1}{2}\omega_{p0}^2|_{\text{peak}}$.

In summary, we have demonstrated experimentally that it is possible to up-shift the carrier frequency of an electromagnetic pulse by passing it through a rapidly growing plasma. Though the achieved frequency shift is small, it is mainly because the pulse length of the present experiment is much longer than the size of generated plasma. If the pulse length can be reduced to be comparable to the length of the chamber (e.g., using 2-nsec pulses), the field intensity of each pulse can be increased considerably without causing gas breakdown near the chamber wall. Thus, the ionization rate of gas in the intersecting regions of two pulses can be increased by a factor of about 500, and a frequency shift $\Delta f_0/f_0 \sim 0.26$ is expected. In order to minimize spectral broadening on

output pulses, a proper shaping of the input pulses is required.

I would like to thank Professor G. Schmidt of Stevens Institute of Technology for stimulating conversations and reading through the manuscript. I also appreciate the technical assistance from Y. S. Zhang and A. Ren. This work was supported by the Air Force Office of Scientific Research, Air Force Systems Command, Grant No.

AFOSR-85-0316.

¹S. C. Wilks, J. M. Dawson, and W. B. Mori, Phys. Rev. Lett. **61**, 337 (1988).

²Eli Yablonovitch, Phys. Rev. Lett. **31**, 877 (1973); **32**, 1101 (1974).

³S. P. Kuo and Y. S. Zhang, Phys. Fluids B **2**, 667 (1990).

⁴A. V. Gurevich, Geomagn. Aeron. **19**, 428 (1979).

Observation of frequency up-conversion in the propagation of a high-power microwave pulse in a self-generated plasma

S.P. Kuo, Y.S. Zhang and A. Ren

Weber Research Institute, Polytechnic University, Route 110, Farmingdale, NY 11735, USA

Received 2 July 1990; revised manuscript received 20 August 1990; accepted for publication 21 August 1990

Communicated by R.C. Davidson

A chamber experiment is conducted to study the propagation of a high-power microwave pulse. The results show that the pulse is experiencing frequency up-shift while ionizing the background air if the initial carrier frequency of the pulse is higher than the electron plasma frequency at the incident boundary. Such a frequency autoconversion process may lead to reflectionless propagation of a high-power microwave pulse through the atmosphere.

1. Introduction

During the past decade, there has been a considerable effort in the study of the propagation of high power microwave pulses through the atmosphere for its applications in high power radar and directed energy systems [1–6]. This study has also been a subject of considerable scientific interest because air breakdown produces ionization phenomena that can radically modify wave propagation [7]. Both fluid and kinetic transport codes have been developed to give a self-consistent description of the propagation process. Many laboratory experiments have also been conducted to verify the results of computer codes.

After air breakdown, a space-time dependent plasma is generated. It attenuates the tail of the pulse but hardly affects its leading edge because it takes finite time for the plasma to build up. A phenomenon which is called "tail erosion" plays the primary role in limiting the transmission of pulse energy. Two mechanisms responsible for the tail erosion phenomenon have been identified experimentally in our previous work [7]. The first one is due to attenuation by the self-generated underdense plasma. It is shown that the erosion to the tail of the pulse is not complete and the loss of the pulse's energy may still be within the tolerable level. The second one is caused through reflection by the self-generated overdense plasma screen. In this case, as shown, a large portion

of the pulse is more or less eroded away during the finite propagation period. The second mechanism is far more severe in causing energy loss of the pulse than the first one. Once the reflection mechanism is in play, the remaining pulse will become too narrow to carry enough energy as desired.

One easy way to avoid cutoff reflection is to restrict the power of the pulse with a given pulse length to be lower than a critical power level. However, this critical power level is usually too low for many practical applications. Therefore, it becomes essential to explore means for more powerful electromagnetic pulses to achieve reflectionless propagation through the atmosphere. Recently, Gildenburg et al. [8] have pointed out that it is indeed possible to achieve reflectionless propagation of powerful EM pulses in an ionizing medium. Their analytical and numerical results [9] show that a frequency autoconversion process is in play in a nonstationary plasma. In particular, when the ionization frequency of the background air becomes much larger than the electron-neutral collision frequency ν , the carrier frequency ω of the pulse will always shift upward with the growth of plasma frequency ω_{pe} so that the plasma during breakdown will always remain transparent to the pulse (i.e. $\omega > \omega_{pe}$).

In this paper, we describe a chamber experiment conducted to demonstrate the frequency autoconversion process. The chamber is made of a 2 foot cube

of plexiglass. A microwave pulse is fed into the cube by an S-band microwave horn placed at one side of the chamber. A second S-band horn placed at the opposite side of the chamber is used to receive the transmitted pulse. The spectra of the incident pulse and transmitted pulse are then compared. The microwave power is generated by a single magnetron tube (OKH1448) driven by a soft tube modulator. The magnetron produces 1 MW peak output power at a frequency of 3.27 GHz. The modulator uses a pulse forming network (PFN) having a pulse width of 1 μ s and a repetition rate of 60 Hz.

In section 2, a theoretical model describing pulse propagation in an ionizing air is introduced. The equation describing the frequency autoconversion process is also derived and discussed. The pulse propagation experiment is presented in section 3 in which the experimental results are also included. A discussion of the work is given in section 4.

2. Modeling of the propagation of a powerful EM pulse in ionizing air

The processes which are relevant to the plasma formation include ionization, attachment, recombination, and diffusion. When the power level of the pulse in consideration far exceeds the breakdown threshold of the air, however, the ionization rate ν_i of the air dominates over all the loss rates of the induced plasma. Thus, the rate equation for the electron density during the pulse period can be simplified by

$$\frac{\partial}{\partial t} \omega_{pe}^2 = \nu_i \omega_{pe}^2, \quad (1)$$

where $\omega_{pe}^2 = 4\pi n_e e^2 / m_e$ is linearly proportional to the electron density n_e and ν_i is proportional to the intensity of the pulse.

The propagation of an EM pulse in such an ionizing medium is governed by the wave equation

$$\left[\frac{\partial^2}{\partial t^2} - c^2 \frac{\partial^2}{\partial x^2} + \omega_{pe}^2 \left(1 - \frac{i\nu}{\omega + i\bar{\nu}} \right) \right] E(x, t) = 0, \quad (2)$$

where the electron momentum equation has been used to determine the current density induced by the

wave field in the plasma; ν is the electron-neutral collision frequency and $\bar{\nu} = \nu + \nu_i$.

Eq. (2) is analyzed by letting

$$E(x, t) = A(x, t) e^{-i\phi(x, t)}$$

and assuming that

$$\left| \frac{\partial}{\partial t} \ln A \right| \ll \left| \frac{\partial}{\partial t} \phi \right|$$

and

$$\left| \frac{\partial}{\partial x} \ln A \right| \ll \left| \frac{\partial}{\partial x} \phi \right|$$

for a pulse which contains many oscillations. Furthermore, the local frequency $\omega = \partial\phi/\partial t$ and wave-number $k = -\partial\phi/\partial x$ are defined. Thus, (2) can be reduced approximately to

$$\frac{\partial}{\partial t} \omega A^2 + \frac{\partial}{\partial x} k c^2 A^2 = - \frac{\omega_{pe}^2 \nu \omega A^2}{\omega^2 + \bar{\nu}^2} \quad (3)$$

and

$$\omega^2 - k^2 c^2 = \omega_{pe}^2 \left(1 - \frac{\nu \bar{\nu}}{\omega^2 + \bar{\nu}^2} \right). \quad (4)$$

From the definition of ω and k , it is required that

$$\frac{\partial}{\partial x} \omega + \frac{\partial}{\partial t} k = 0. \quad (5)$$

Taking the partial time derivative of (4) and using relation (5), the equation describing the frequency autoconversion is derived to be

$$\frac{\partial}{\partial t} \omega^2 + \nu_i \frac{\partial}{\partial x} \omega^2 = \frac{1 - \nu \bar{\nu} / (\omega^2 + \bar{\nu}^2)}{1 - \omega_{pe}^2 \nu \bar{\nu} / (\omega^2 + \bar{\nu}^2)^2} \frac{\partial}{\partial t} \omega_{pe}^2 \quad (6)$$

where $v_g = \partial\omega/\partial k$ is the local group velocity of the pulse.

Under the conditions that $\nu \bar{\nu} \ll \omega^2 + \bar{\nu}^2$ and $\omega_{pe}^2 \lesssim \omega^2 + \bar{\nu}^2$, (6) reduces to the equation derived by Gildenburg et al. [8],

$$\frac{d}{dt} (\omega^2 - \omega_{pe}^2) = -v_g \frac{\partial}{\partial x} \omega_{pe}^2, \quad (7)$$

where $d/dt = \partial/\partial t + v_g \partial/\partial x$ is the total time derivative along the group trajectory of the pulse.

The implication of eq. (7) is illustrated as follows. Consider a rectangular pulse as shown in fig. 1, the

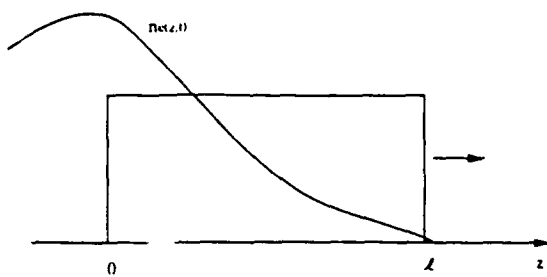


Fig. 1. Envelope of a rectangular pulse and the pulse-generated electron density distribution.

density of the induced plasma at a given time t is expected to grow spatially from the background level at the leading edge of the pulse to a peak value at the tail end of the pulse. Behind the pulse, the density drops from the peak level due to various loss mechanisms. The envisioned density profile is also plotted in fig. 1. Therefore, $\partial\omega_{pe}^2/\partial x < 0$ in the pulse interval and consequently, $d(\omega^2 - \omega_{pe}^2)/dt > 0$. This implies that plasma during the breakdown can remain transparent (i.e. $\omega > \omega_{pe}$) to the pulse as long as $\omega > \omega_{pe}$ initially. A frequency autoconversion process leads to reflectionless pulse propagation. Moreover, eq. (7) can be rewritten as

$$\frac{d}{dt} \omega^2 = \nu_i \omega_{pe}^2 \geq 0,$$

an up-shift in the carrier frequency of the pulse is anticipated. In the following, a chamber experiment on wave propagation is performed to observe the frequency up-conversion phenomenon as a manifestation of eq. (7). It is noted that it is desirable to keep the distortion of the pulse due to plasma generation small so that $\nu_i \omega_{pe}^2$ can be kept nearly a constant value along the pulse's trajectory thereby achieving the greatest frequency shift.

3. Experimental results

The block diagram of the experimental setup is shown in fig. 2. A directional coupler connected to the horn transmitting the input pulse is used to monitor the spectrum of the input pulse which is used as the reference. After passing through the chamber, the pulse is received by a second horn placed at the opposite side of the chamber. The chamber is pumped to the lowest pressure at about 0.15 Torr in order to minimize the electron-neutral collision frequency ν , which is below $5 \times 10^8 \text{ s}^{-1}$. Limited by the available power of the magnetron tube, the ionization frequency ν_i is less than 10^8 s^{-1} . Thus, $\nu \nu_i \ll \omega^2$. We also limit the power level of the input pulse in order to prevent the overdense plasma being generated near

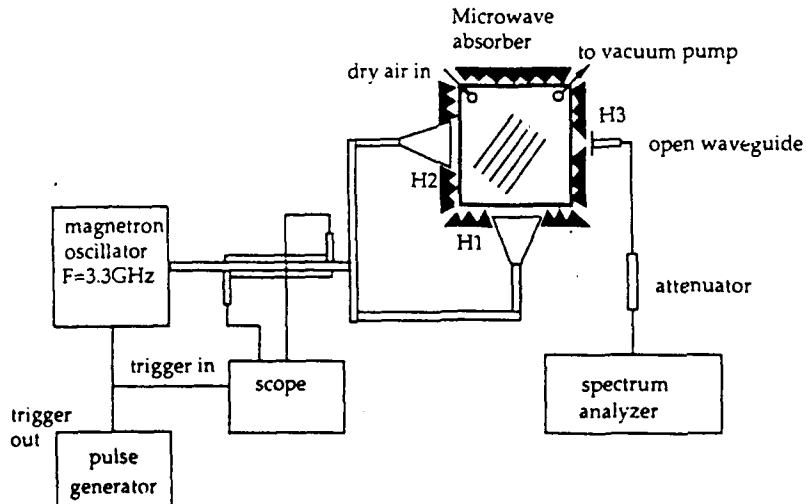


Fig. 2. Experimental setup.

the incident boundary, i.e. ω_{pe} (at $x=0$) $\leq \omega$. The assumptions of eq. (7) are then justifiable with the current experiment.

One microsecond pulse is used in the experiment, thus, the spatial length of the pulse is about 300 m long which is much longer than the length 0.6 m of the chamber. Since in any instance only a small fraction of the pulse can fit inside the chamber where plasma is generated by the field of the same pulse, we can only anticipate to observe a very small percentage of frequency shift in the present experiment. In other words, one may divide the pulse into 500 segments and each segment of the pulse experiences a frequency shift while it is inside the chamber. Therefore, the maximum frequency shift on the output pulse may just be the maximum frequency shift of each segment.

Three sets of frequency spectra are presented in figs. 3a-3c. In each set of frequency spectra, curve 1 is the frequency spectrum of the input pulse, while curve 2 is the frequency spectrum of the output pulse. The results are recorded for three consecutively increasing amplitudes of the input pulse transmitted into the chamber. The frequency difference between the peaks of each spectral set represents the frequency shift attributed to the plasma generation in the chamber by the corresponding input pulse. It is shown that the frequency shift in the first two cases (figs. 3a and 3b) is much larger than that in the third case (fig. 3c). On the other hand, one can also note that the distortion of the pulse shape and the attenuation of the pulse intensity in the first two cases are much smaller than those in the third case. It suggests that if the pulse is not distorted seriously (i.e. $\omega > \omega_{pe}$) at the incident boundary, the pulse will not be distorted seriously and is experiencing frequency up-shift while ionizing the air during the subsequent propagation period. This is precisely the implication of eq. (7).

It is noted that the achievable frequency of the present experiment is much less than that reported in the previous work [10] conducted in the same experimental setup. The reason is that the previous experiment is performed by using two crossed microwave pulses so that the plasma in the chamber is generated simultaneously in the intersecting region of the pulses. Thus, the initial effect (causing the change of frequency) is dominant over the boundary

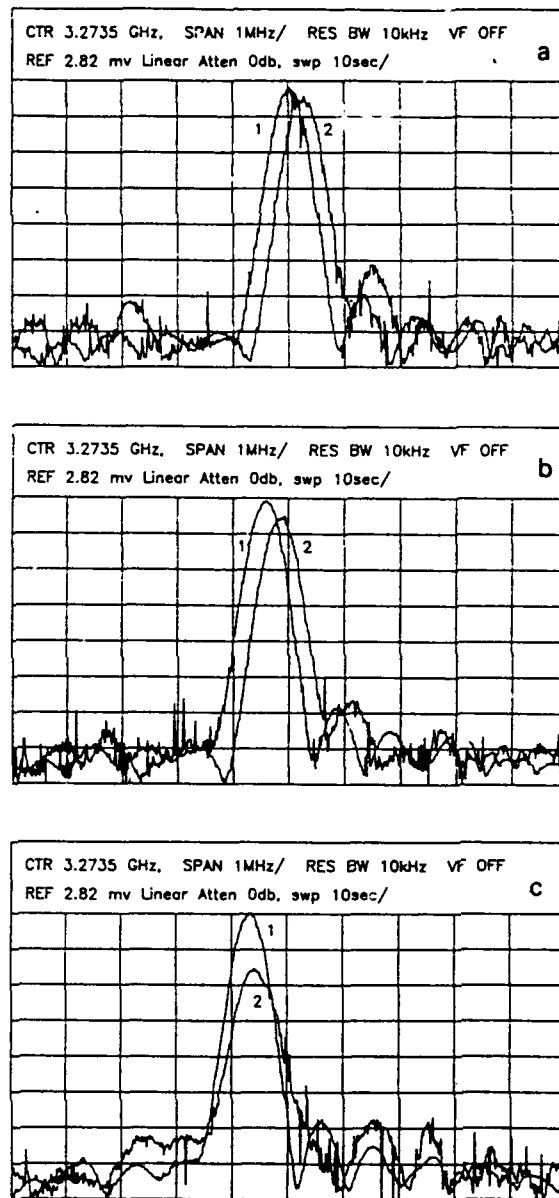


Fig. 3. The frequency spectra of the input (curve 1) and output (curve 2) pulses, the background air pressure is 0.15 Torr. (a) Microwave power $P \sim 1.1P_{th}$, the breakdown threshold power; (b) $P \sim 1.27P_{th}$; (c) $P \sim 1.42P_{th}$.

effect (causing the change of the wavenumber). On the other hand, the present work is aimed at studying and improving pulse propagation, hence, only a single pulse is used in the experiment. Thus, the bound-

ary effect and the initial effect are always mixed during the density change. The boundary effect works to countervalue the initial effect in causing the frequency shift.

4. Discussion

A pulse propagation experiment for demonstrating the frequency autoconversion process in an ionizing medium is conducted in a large chamber. The results show that the output pulse with less distortion by the self-generated plasma experiences more frequency up-shift. It is consistent with the implication of eq. (7) which indicates that if $\omega > \omega_{pe}$ initially and pulse energy depletion by the self-generated plasma is small, then $\omega > \omega_{pe}$ throughout the propagation. Moreover, ω increases along the pulse's trajectory.

However, how are the experimental results related to the point of frequency autoconversion process for reflectionless pulse propagation? It should be noted that the air pressure inside the chamber is more or less uniform. On the other hand, the air pressure from the ground to space decreases with the altitude and the breakdown threshold of the air is pressure dependent. In general, the breakdown threshold decreases with altitude before reaching an altitude having the Paschen breakdown minimum. Beyond that altitude, the breakdown threshold increases with the altitude [11]. Therefore, if the pulse is transmitted from the ground to space and if the ionization density on the ground, where the breakdown threshold is very high, does not exceed the critical density set by the carrier frequency of the pulse, the pulse is expected to propagate through the Paschen minimum region without experiencing cutoff reflection even if the pulse intensity in that region is many times the

breakdown threshold intensity. This is because the carrier frequency of the pulse is continuously shifted upward as more dense plasma is generated during the propagation. Likewise, such a frequency autoconversion process also works for pulse propagation from space to the ground.

The frequency autoconversion process is expected to make the operation of the high power radar and directed energy systems easier and more effective.

Acknowledgement

This work is supported by the Air Force Office of Scientific Research Grant No. AFOSR-85-0316 and by the Air Force Geophysical Laboratory through NASA Grant No. NAG 5-1051. Useful discussion with Professor B.R. Cheo is appreciated.

References

- [1] W.M. Bollen, C.L. Yee, A.W. Ali, M.J. Nagurney and M.E. Read, *J. Appl. Phys.* 54 (1983) 101;
C.L. Yee, A.W. Ali and W.M. Bollen, *J. Appl. Phys.* 54 (1983) 1278.
- [2] J.H. Yee, R.A. Alvarez, D.J. Mayhall, N.K. Madsen and H.S. Cabayan, *J. Radiat. Eff. Res. Eng.* 3 (1984) 152.
- [3] B. Goldstein and C. Longmire, *J. Radiat. Eff. Res. Eng.* 3 (1984) 1626.
- [4] Wee Woo and J.S. DeGroot, *Phys. Fluids* 27 (1984) 475.
- [5] J.H. Yee, R.A. Alvarez, D.J. Mayhall, D.P. Byrne and J. DeGroot, *Phys. Fluids* 29 (1986) 1238.
- [6] M.J. Mulbrandon, J. Chen, P.J. Palmadesso, C.A. Sullivan and A.W. Ali, *Phys. Fluids B* 1 (1989) 2507.
- [7] S.P. Kuo, Y.S. Zhang and P. Kossey, *J. Appl. Phys.* 67 (1990) 2762.
- [8] V.B. Gildenburg, V.A. Krupnov and V.E. Semenov, *Pis'ma Zh. Tekh. Fiz.* 14 (1988) 1695.
- [9] V.A. Krupnov, Workshop on Artificial ionized layers in the atmosphere, Kiev, USSR, October 1989.
- [10] S.P. Kuo, *Phys. Rev. Lett.*, in press.
- [11] S.P. Kuo and Y.S. Zhang, *Phys. Fluids B* 2 (1990) 667.

Scattering and Broadband Absorption of Microwaves by an Arc Plasma Column*

A. Y. Ho and S. P. Kuo
Weber Research Institute
Polytechnic University
Route 110, Farmingdale, NY 11735

* Work supported by AFOSR.

ABSTRACT

The absorption and scattering of microwaves by a single column arc plasma are studied and compared with the theory. The plasma is produced in a background pressure 1 to 10 Torr through steady state hollow cathode discharge where the cathode is made of Tantalum tubing allowing Argon gas to flow through. The diameter of the plasma column can be varied from 2 to 10 cm by varying the gas flow. The current and voltage of the arc are about 10 A and 50 V, respectively. This plasma is shown to give rise to strong absorption and scattering of incident microwave. The scattering experiment is performed by placing the vacuum chamber in the far field zone of the transmitting horn and measuring the angular distribution of the scattered field intensities. The result shows the expected attenuation of the signal in the forward direction together with the scattering of the incident wave to the sides.

EXPERIMENTAL SETUP

Hollow Cathode Discharge

The plasma discharge experimental set-up is shown in figure 1. A vacuum system made of a large bell-jar was used to contain the argon plasma produced by hollow cathode discharge. The hollow electrodes are made from Tantalum for its relatively low work function and high melting point. The background pressure can be varied from 300mTorr to about 10 Torr by regulating the amount of argon gas flowing through the hollow cathode. Figure 2 shows the electrical schematic of the discharge circuit. When the background pressure is stabilized at about 1 Torr, the application of an RF trigger to the electrodes heats the cathode sufficiently to allow a self-sustained discharge to begin. The electrical operating parameters of the plasma were 10 amps and 50 volts established by the external power supply and circuitry which were variable up to 100 amps and 300 volts maximum. Using optical and spectroscopic diagnostics, the plasma parameters were estimated to be $n_e \sim 10^{11}-10^{13} \text{ cm}^{-3}$ and $T_e \sim 1-2 \text{ eV}$. By varying the gas flow, and thus the background pressure, the plasma can be varied to appear as a pinched, dense column with diameter of the order of 2 cm to a less dense, elongated spheroid with minor axis of the order of 10 cm. The length of the column in all cases can be varied from 5 to 10 inches by adjusting the distance between the electrodes.

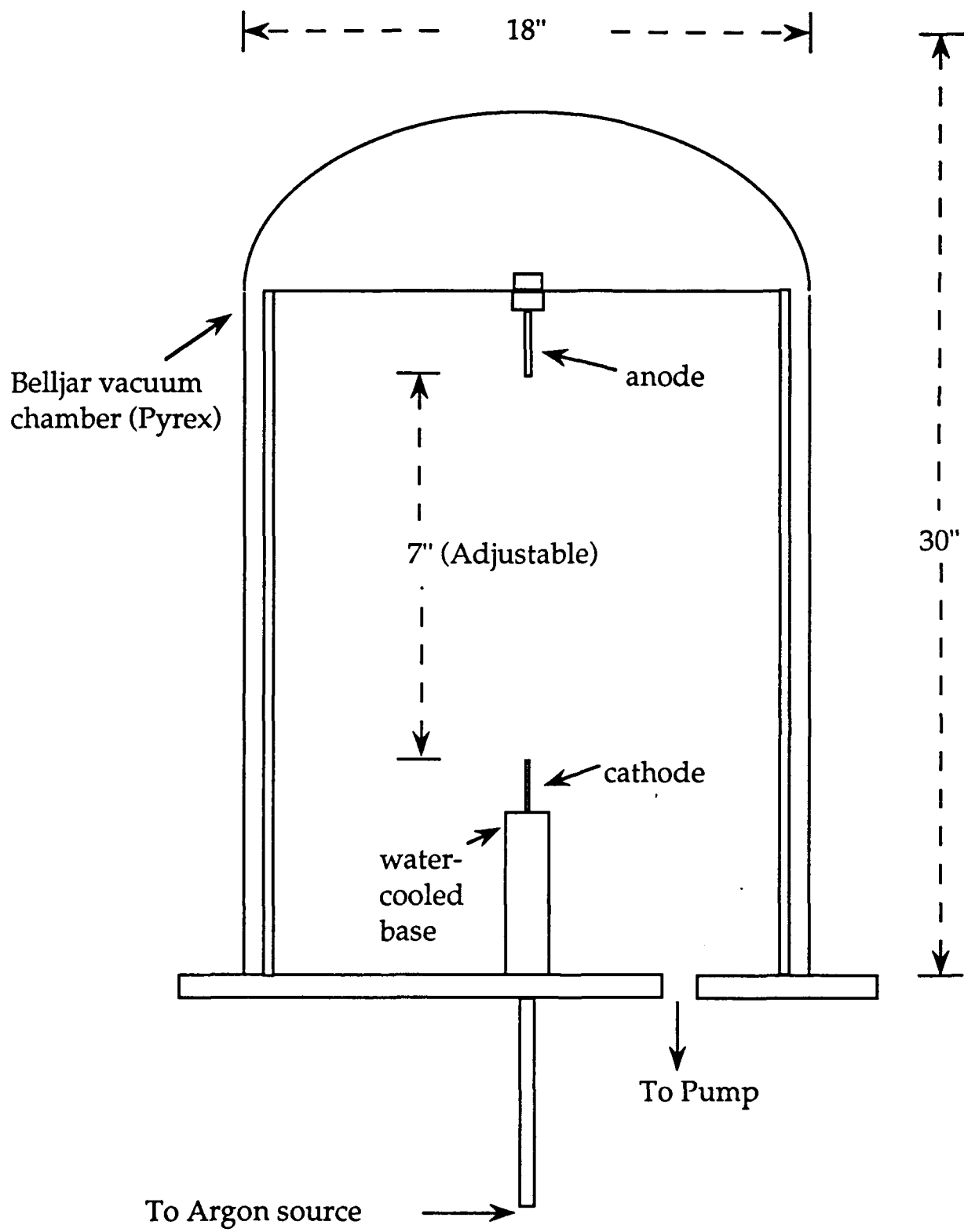


Figure 1. Schematic diagram of single hollow cathode discharge unit.

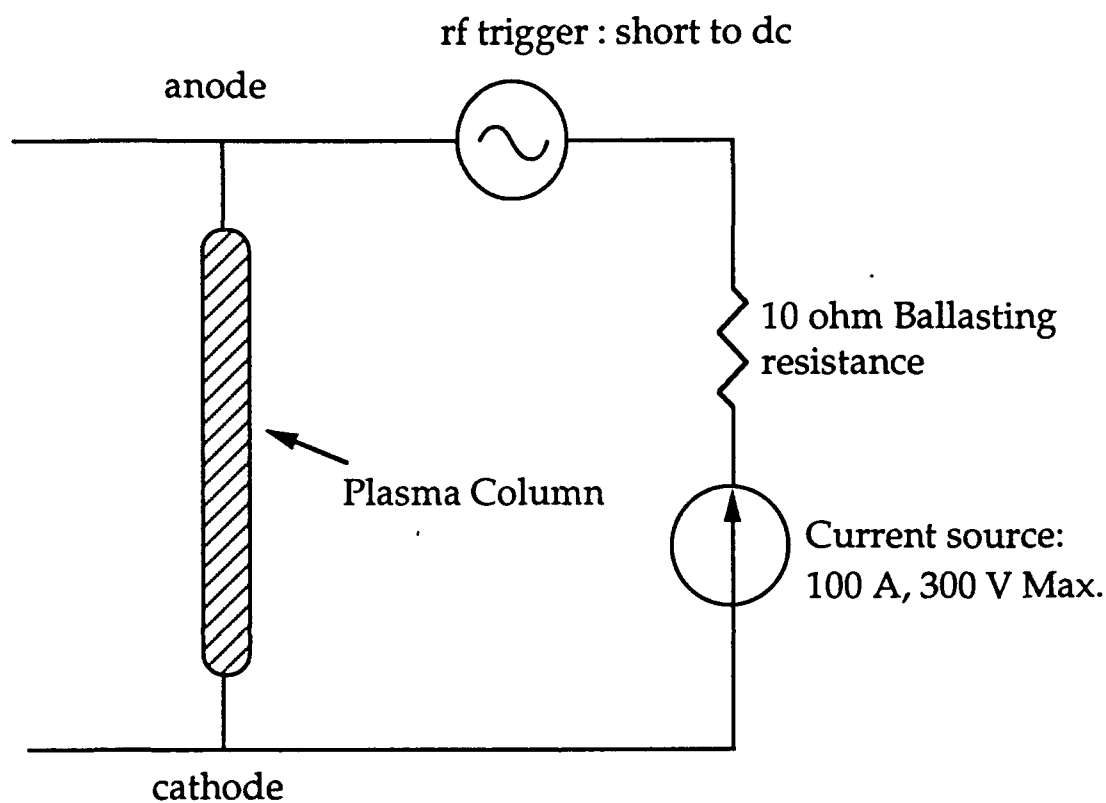


Fig. 2 Schematic diagram of the HCD discharge circuit.

Microwave Scattering

The microwave scattering set-up is shown in figure 3. An HP microwave sweep generator was set up for 10 dBm cw nominal power output at frequencies selectable from 3.8 to 12 GHz. The signal is fed to a launching horn aimed at the plasma chamber and is placed near it. Microwave absorbers are then placed surrounding the chamber to minimize unwanted reflections and scattering from nearby objects. Windows in the absorbers allow the placement of a receiving horn at various angles about the center of the plasma chamber to pick up the microwave signal. A spectrum analyzer also capable of time domain sweeps is then used to examine the received signal in the presence and in the absence of the plasma column.

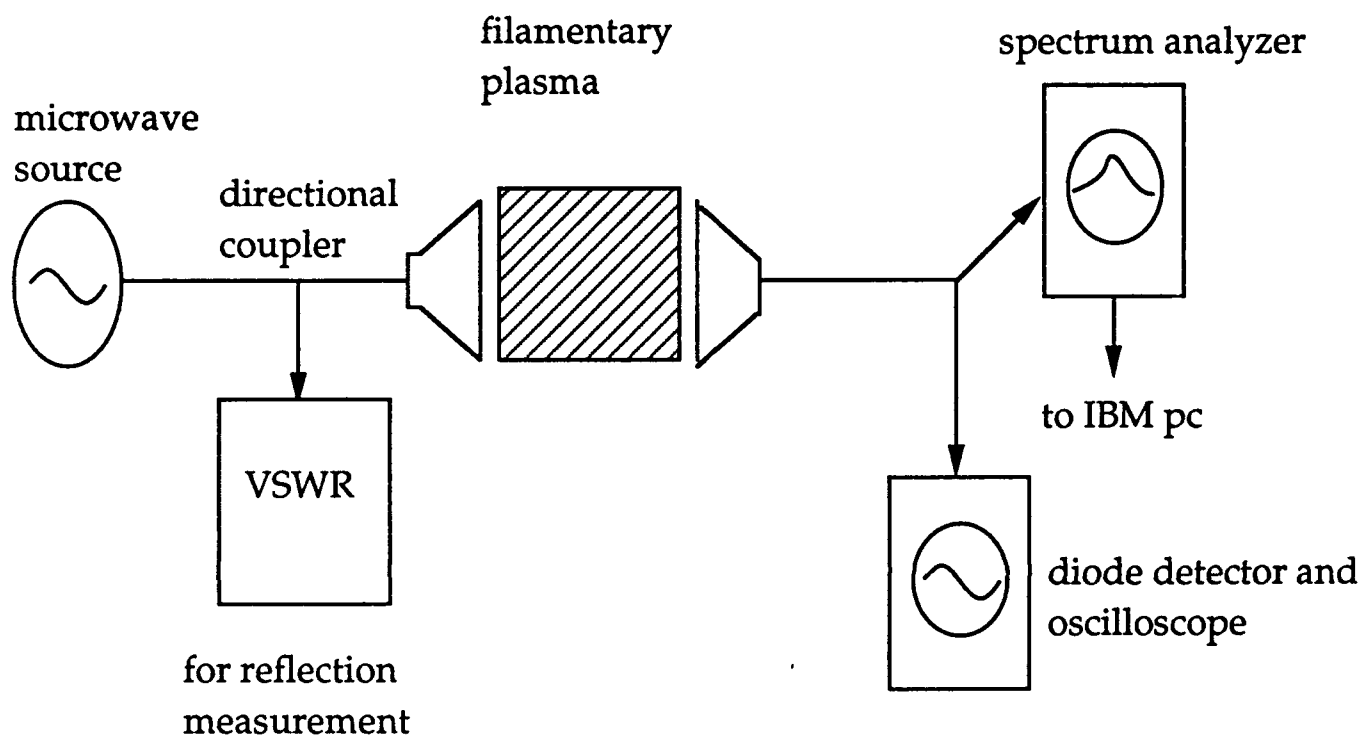


Fig. 3 Schematic diagram of experimental setup.

EXPERIMENTAL RESULTS

Broadband Attenuation

A typical frequency domain sweep from 4 - 8 GHz comparing the forward received signal with and without plasma is shown in figure 4. It is seen that attenuation to the transmitted signal in the forward direction attributable to absorption and scattering occurs over the whole frequency range. Fluctuations in the amount of attenuation are due to fluctuations in the plasma during the time the spectrum analyzer took its reading at each particular frequency. This plasma fluctuation has been observed experimentally by the use of a photomultiplier tube and the cause has been traced to the ac ripples in the source supply. Since the sampling algorithm in the analyzer displays the peak received value within any sampling period, one expects that the maximum observed attenuation should apply to all frequencies if the plasma can be made more quiescent.

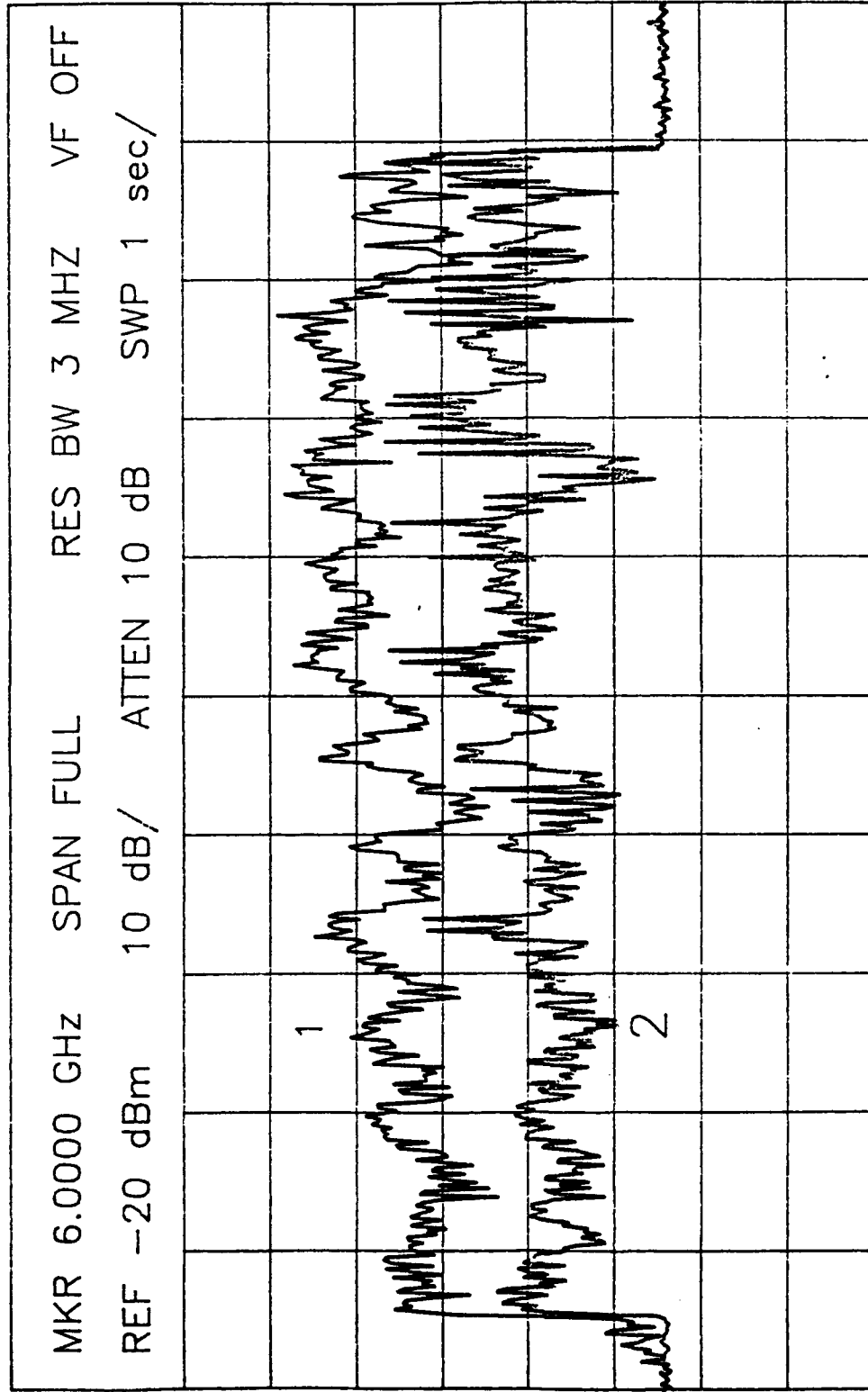


Figure 4 Spectral distribution of transmitted wave. (4 - 8 GHz sweep)
 Curve 1 - without plasma column in chamber.
 Curve 2 - plasma column present.

Angular Distribution of Scattering Wave

Measurements of the angular spectrum of microwave scattering by the plasma column at 6 GHz are shown in figure 5. Three sets of data taken under as close as possible conditions were used to generate the curve and error bars. The data points are normalized to the incident wave for comparison with the theoretical results to be presented in the future. It can be seen from the attenuation of the signal in the forward direction and the enhancement of received signal above 20 degrees from forward that the plasma column indeed scatters the incident wave away from the forward and to the sides. The attenuation to the incident wave in the forward direction as shown is 26 dBs. The typical value of the enhanced signal is -10 dB below the incident power level.

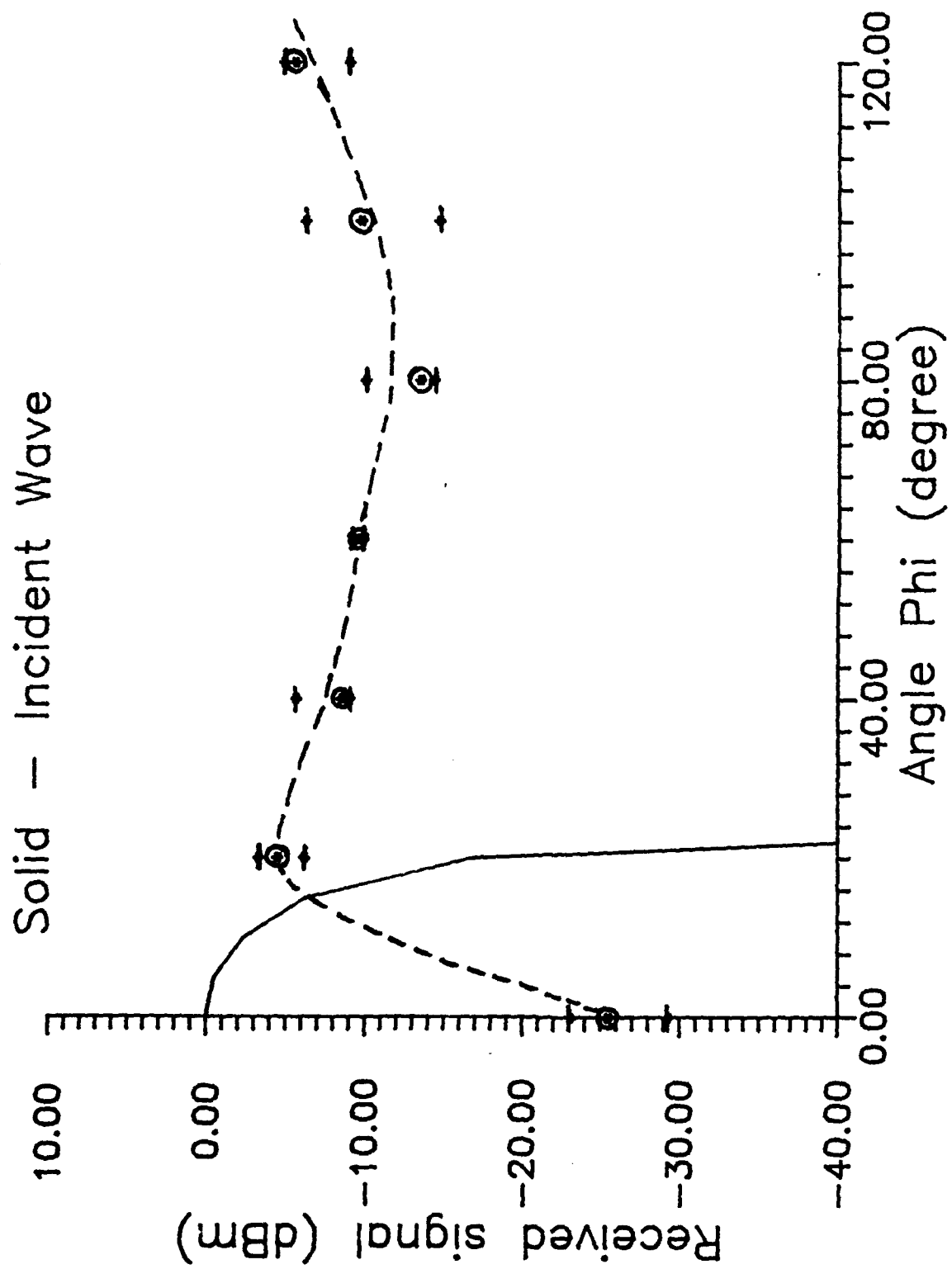


Figure 5 Angular distribution of scattering wave